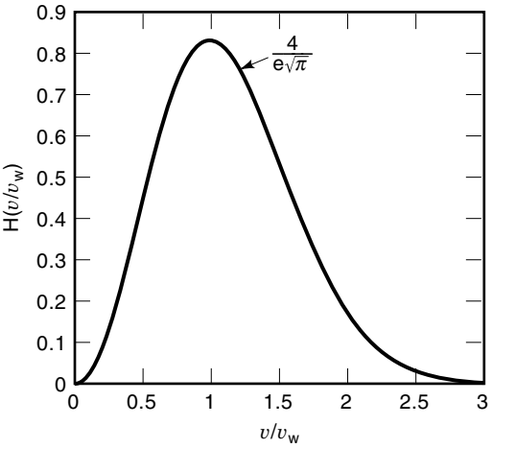

Figure 1. Boltzmann–Maxwell velocity distribution.

CONDUCTION AND BREAKDOWN IN GASES

BASIC STRUCTURE AND CHARACTERISTICS OF GASES

During breakdown in gases, electrons and ions are accelerated to such a high energy level by the applied electric field that additional charged particles are produced by ionization processes. To understand these processes some knowledge about the movement of gas molecules is a prerequisite.

Velocity of Gas Molecules

In an ideal atomic or molecular gas, the velocity distribution of particles is described by the Boltzmann–Maxwell distribution (Fig. 1). The gas atoms or molecules are assumed to behave like elastic balls moving linearly with constant velocity until a collision occurs with the wall or another particle. The energy of the moving particles is so low that no excitation or ionization occurs.

The Boltzmann–Maxwell distribution is described by the following expression:

$$\frac{dN(v)/N}{dv/v_w} = H_{(v/v_w)} = \frac{4}{\sqrt{\pi}} \left(\frac{v}{v_w}\right)^2 \exp\left[-\left(\frac{v}{v_w}\right)^2\right] \qquad (1)$$

$N(v)$ is the number of particles with the velocity v, N the total number of particles and v_w the velocity with the highest probability. Because of the nonsymmetrical distribution, the mean value of the velocity v_m is higher than v_w. For the same reason, the effective velocity v_{eff}, which is relevant for energy calculations, is higher than v_m.

By integrating Eq. (1), we obtain

$$v_m = \overline{v} = \frac{2}{\sqrt{\pi}} v_w = 1.128\, v_w \qquad (2)$$

$$v_{eff} = \sqrt{\overline{v^2}} = \sqrt{\frac{3}{2}} v_w - 1.224\, v_w \qquad (3)$$

Because of the energy exchange by collision, the mean kinetic energy of all particles irrespective of their mass is identical. It is assumed that no additional energy is transferred to the elastic balls of the model gas. Then the mean kinetic energy of each particle with mass m is $0.5 \cdot k \cdot T$ for each possible direction of movement. The mean total energy of a particle is given by

$$W_{kin} = \frac{3}{2} kT = \frac{1}{2} m v_{eff}^2 \qquad (4)$$

where the Boltzmann constant $k = 1.38 \cdot 10^{-23}$ J/K and T is the absolute temperature. From Eqs. (2)–(4), the parameters of the velocity distribution can be calculated:

$$\begin{aligned} v_{eff} &= \sqrt{\frac{3kT}{m}} \\ v_w &= \sqrt{\frac{2kT}{m}} \\ v_m &= \sqrt{\frac{8kT}{\pi m}} \end{aligned} \qquad (5)$$

The calculated mean values of the velocity v_m for different gases at $T = 273.15$ K (0°C) are listed in Table 1 (1). This velocity distribution also applies to the electrons in the gas. Therefore the relevant mass has to be taken into account, which for electrons is

$$m_e = 9.1 \cdot 10^{-31}\,\text{kg} \qquad (6)$$

Table 1. Relative Mass and Mean Velocity v_m of Molecules in Different Gases at 0°C[a]

Gas	Relative Mass of Molecules	v_m, mm/μs
N_2	28	0.45
O_2	32	0.42
H_2	2	1.70
CO_2	44	0.36
SF_6	146	0.20
Electrons	1/1840	100

[a] Ref. 1.

For atoms or molecules, the proton mass m_p

$$m_p = 1840\, m_e = 1.67 \cdot 10^{-27}\,\text{kg} \tag{7}$$

has to be multiplied by the relative atomic or molecular mass.

During a time interval of technical relevance, which is typically 1 μs, the thermal movement of gas molecules at 0°C is on the order of 1 mm and of electrons approximately 100 mm. However this is not a linear movement, but a stochastic movement due to the large number of collisions.

General Gas Law

As for any gas, the mean molecular energy depends only on the temperature. The pressure is the same provided that the particle density is equal. Therefore the pressure p on the walls of an enclosure is proportional to the particle density and the mean energy per particle for example, the temperature T. This can be derived from Fig. 2. In the volume element $dx\,dy\,dz$ at the wall of an enclosure on an area $dy\,dz$ the particles hit the wall and are reflected elastically. Only the vertical components of the forces or impulses are relevant for the pressure. During an elastic reflection the following impulse difference occurs:

$$\Delta F_x\, dt = 2\, m |v_x| \tag{8}$$

which is absorbed by the wall. With $dx/dt = v_x$, the force of an impact is given by

$$\Delta F_x = 2\, m\, \frac{v_x^2}{dx} \tag{9}$$

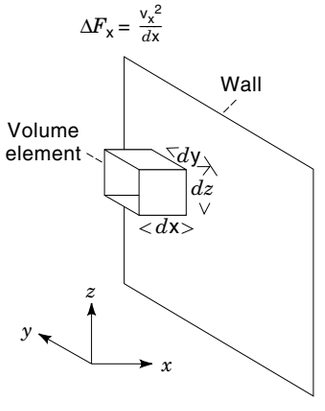

Figure 2. Outside wall of an enclosure with gas molecules and adjacent volume element.

Because the velocity distribution is equal in all directions, only 50% of the total number of particles $dx\,dy\,dz\,N/\mathrm{V}$ in the volume element have a positive velocity v. These contribute to the impact at the wall element $dy\,dz$. The mean force of all impacts is given by

$$\overline{F}_x = \frac{1}{2}\frac{N}{V}\, dx\, dy\, dz\, 2\, m\, \frac{v_x^2}{dx} \tag{10}$$

and the mean pressure

$$\overline{p} = \frac{\overline{F}_x}{dy\, dz} = \frac{N}{V}\, m \overline{v}_x^2 \tag{11}$$

The effective velocity

$$v_{\text{eff}}^2 = \overline{v}^2 = \overline{v}_x^2 + \overline{v}_y^2 + \overline{v}_z^2 \tag{12}$$

is the result of equal distribution of the components:

$$\overline{v}_x^2 = \overline{v}_y^2 = \overline{v}_z^2 \Rightarrow v_{\text{eff}}^2 = 3\overline{v}_x^2 \tag{13}$$

The mean pressure $\overline{p}$ caused by many impacts corresponds to the pressure p at the walls:

$$p = \frac{1}{3}\frac{N}{V}\, m v_{\text{eff}}^2 \tag{14}$$

From Eq. (5) we obtain the general gas law:

$$pV = NkT \Rightarrow p = nkT$$

where

$$n = \frac{N}{V} \tag{15}$$

The relative molecular (or atomic) mass of a gas g in grams is a mole. For any ideal gas, a mole contains the same number of particles N_a, which is called Avogadro's number. This is calculated from the proton mass m_p [Eq. (7)]. A proton has a relative atomic mass of 1.008.

$$N_a = \frac{1.008\, g}{m_p} = 6.02 \cdot 10^{23} \frac{\text{molecules}}{\text{mol}} \tag{16}$$

At 0°C and 1 bar pressure the volume of a mole of any ideal gas is 22.7 liters.

Mean Free Path

In ideal gases, between successive impacts the particles travel the free path λ, which has a statistical spread around the mean free path λ_m. This is a very important characteristic for the interaction of charged particles (ions or electrons) with neutral atoms or molecules of the gas. The charged particles receive a certain energy from an applied electric field, which in part is transferred by impact to the molecules and atoms of the gas. Such impact processes produce ionization and carrier multiplication, which may induce breakdown. These processes occur only if the energy of the particles exceeds certain limits.

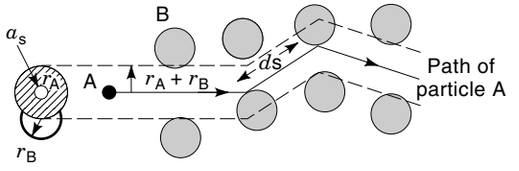

Figure 3. Model for the free path and the collision cross section.

Because of an applied electric field, a directed field-induced movement of the charged particles is superimposed on the undirected thermal movement. Figure 3 shows the path of a particle A with radius r_A through the gas consisting of particles B with radius r_B. If particles B do not move, a collision between particles A and B is possible within the shaded area a_s:

$$a_s = \pi (r_A + r_B)^2 \tag{17}$$

called the collision cross section. The probability of a collision between particles A and B on their zigzag path ds through the gas is given by

$$dw = n_B a_s \, ds \tag{18}$$

where n_B is the concentration of molecules of gas B. Because the mean free path is λ_m, the probability of a collision on the path ds is expressed by

$$dw = \frac{ds}{\lambda_m} \tag{19}$$

Combining Eqs. (18) and (19), the mean free path is given by

$$\lambda_m = \frac{1}{n_B a_s} \tag{20}$$

and is a function of the gas density n_B and the collision cross section a_s of the particles. It is assumed that only few particles A are within gas B, so that the total number of particles n is approximately n_B. From Eq. (15) we obtain

$$\lambda_m = \frac{1}{a_s} \frac{kT}{p} \tag{21}$$

The mean free path depends on gas temperature, gas pressure, and the collision cross section. For collisions of electrons with gas molecules which are nearly stationary with $r_A \ll r_B$, the mean free path of the electrons is given by

$$\lambda_{me} \approx \frac{1}{\pi r_B^2} \frac{kT}{p} \tag{22}$$

For collisions of ions with gas molecules with $r_B \approx r_A$, the mean free path of the ions is given by

$$\lambda_{mi} \approx \frac{1}{4\pi r_B^2} \frac{kT}{p} \tag{23}$$

For purely thermal motion of particles with similar molecular mass and size ($r_B \approx r_A$), Eq. (23) may also be applied. However, statistically the velocity vectors of the colliding particles are orthogonal to each other, which reduces the mean free path of the gas molecules by the factor $\sqrt{2}$ (2).

$$\lambda_{mg} \approx \frac{1}{4\sqrt{2}\pi r_B^2} \frac{kT}{p} \tag{24}$$

By comparing Eqs. (22)–(24) it is evident that the mean free path of electrons in a gas is significantly larger than that of the gas molecules:

$$\lambda_{me} \approx 4\lambda_{mi} \approx 4\sqrt{2}\lambda_{mg} \tag{25}$$

Table 2 gives the mean free path for gas molecules and electrons for different gases (1). With the mean velocity v_m (Table 1) and the mean free path λ_m (Table 2), the mean transit time τ_m between collisions and the collision frequency f_m is given by

$$\tau_m = \frac{1}{f_m} = \frac{\lambda_m}{V_m} \tag{26}$$

The ideal gas model with spherical molecules and ions and point electrons undergoing elastic collisions is an approximation. Electric forces are effective at some distance between the charged particles. Therefore the real collision cross sections are larger than the area of the gas model. For high energy, excitation and ionization have to be taken into account, which greatly influence the energy transfer and the cross section.

This can be seen from Fig. 4, where measurements of cross sections for electrons are plotted (2). The energy is given in eV, which is the amount of energy transferred to an electron if it passes a potential of 1 V within an electric field. Given the electron charge of $e = 1.6 \times 10^{-19}$ C, this energy is 1 eV $= 1.6 \times 10^{-19}$ J.

In a model gas with elastic collisions, the distribution of the free path can be calculated. $N_a(x)$ is the number of charged particles which have traveled a path of length x without colliding with a gas molecule. Their free path is equal or greater than x. These charged particles enter a gas element of thickness dx at point x. The number of charged particles $N_a(x)$, which until now did not collide changes within this element by dN_a, and will have a collision now. According to the probability for a collision dw and with Eq. (19) for $ds = dx$,

$$dN_{Ax} = -N_{Ax} \, dw = -N_{Ax} \frac{dx}{\lambda_m} \tag{27}$$

$$N_{Ax} = N_{A0} \exp\left(-\frac{x}{\lambda_m}\right) \tag{28}$$

Table 2. Mean Free Path λ_{mg} for Gas Molecules and λ_{me} for Electrons for Different Gases at 0°C and 1 Bar[a]

Gas	λ_{mg} in μm	λ_{me} in μm
H_2	0.11	0.63
N_2	0.058	0.33
O_2	0.064	0.36
CO_2	0.039	0.22
SF_6	0.025	0.13

[a] Ref. 1.

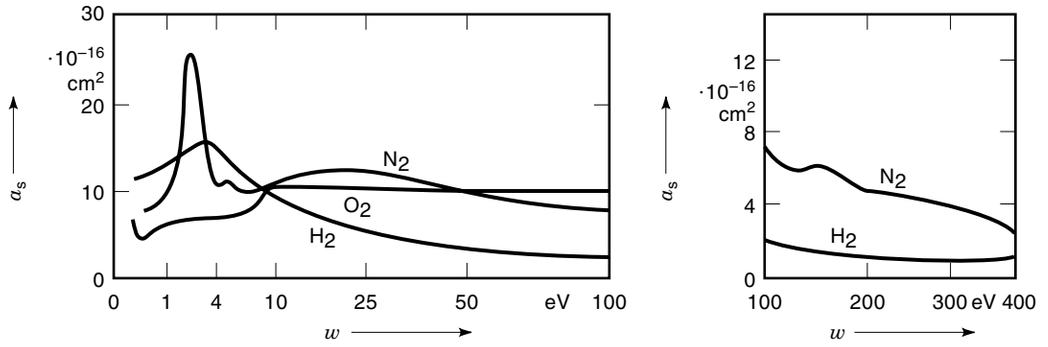

Figure 4. Collision cross section a_s for slow electrons in different gases (2).

The cumulative probability P for a free path λ equal to or greater than x is given by

$$P_{x/\lambda_m} = \frac{N_{Ax}}{N_{A0}} = \exp\left(-\frac{x}{\lambda_m}\right) \tag{29}$$

P is the fraction of particles with a free path λ equal to or greater than x (Fig. 5). For one carrier ($N_a(0) = 1$), P is the probability that the free path is equal to or greater than x. 37% of all particles have a free path equal or greater than λ_m ($x = \lambda_m$), and 0.0045% have a free path equal or greater than $10\lambda_m$ ($x = 10\lambda_m$).

Movement of Charged Particles

Charged particles in a gas are ions and electrons. Ions are generated from neutral molecules or atoms by detachment or attachment of electrons. Therefore ions have a positive or negative charge equal to the corresponding sum of the electron charges. The ion mass is normally equal to that of the molecules or atoms from which they have been generated, because the electron mass [Eq. (6)] is negligible.

As the charged particles in the gas are slowed down by collisions with the molecules, a limited velocity is reached based on the applied field. Actually the particles move on a zigzag course, but effectively they are accelerated on their mean free path in the direction or opposite to direction of the electric field. The mean directed drift velocity v_E is given by

$$v_E = bE \tag{30}$$

where the mobility of the particles is b. Collisions between the charged particles can be neglected, because during the prebreakdown phenomena in gases, the density of the charged particles is negligible compared with the molecular density.

The energy ΔW which is transferred by a collision of two particles can be estimated from the following model. It is assumed that no excitation or ionization occurs during the collision. This means that the structure of the particles and their potential energy is unchanged, and they can be simulated by elastic balls.

If a center-of-mass collision is assumed, from the energy and impulse laws the energy ΔW (3), which is transferred from particle 1 with mass m_1 and kinetic energy W to a stationary particle 2 with mass m_2 is given by

$$\frac{\Delta W}{W} = \delta = 4\frac{m_1 m_2}{(m_1 + m_2)^2} \tag{31}$$

If all possible directions with their statistical distribution are taken into account (3),

$$\frac{\Delta W}{W} = \delta = 2\frac{m_1 m_2}{(m_1 + m_2)^2} \tag{32}$$

During the collision of an electron with a molecule ($m_1 = m_e \ll m_2$) only the small fraction δ_e

$$\delta_e = 2\frac{m_e}{m_2} \ll 1 \tag{33}$$

of the electron energy is transferred to the gas molecule. Therefore the mobility b_e of the electrons is very high [Eq. (30)] and many collisions have to occur, until the energy accepted from the electric field is transferred to the gas molecules. For this reason electrons in an electric field have a much higher kinetic energy than the gas molecules.

During the collision of ions with gas molecules ($m_1 \approx m_2$), according to Eq. (32) a large fraction δ_l of the energy of the ion is transferred to the gas molecule:

$$\delta_l = \frac{1}{2} \tag{34}$$

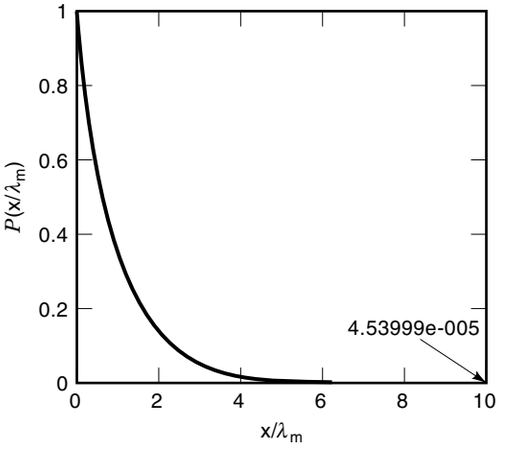

Figure 5. Probability for a free path $\lambda \geq x$.

After a few collisions, the energy of the ions which was accepted from the electric field has been transferred to the gas molecules. Therefore the kinetic energy of the ions is only slightly higher than that of the neutral gas molecules and their mobility b_I is comparatively low.

To calculate the mobility, consider a charged particle with the mass m and charge q within a molecular gas. Because of the force qE of the electric field E, the charged particle will receive a mean directed velocity increase during the mean transit time τ_m between two collisions given by

$$v_E = \frac{1}{2}\frac{q}{m}\tau_m E \tag{35}$$

The total velocity v is obtained together with the initial speed after the preceding collision. With the mean free path λ_m the mean transit time τ_m is given by

$$\tau_m = \frac{\lambda_m}{v_m} \tag{36}$$

The probability of every direction of the velocity vector after each collision is identical. In that case the mean directed velocity increase v_E according to Eq. (35) is identical to the mean directed drift velocity caused by the electric field. Additionally it is assumed that the mean velocity increase v_E on the free path is small compared with the mean total velocity v_m. It can also be assumed that the total velocity on the free path is approximately constant and the total velocity v of the particle before the next collision is also equal to v_m.

The corresponding total velocity of the field-induced velocity component before a collision caused by the linearly accelerated movement is $2v_E$. The energy balance for the collision is given by

$$\frac{1}{2}m(2v_E)^2 + \delta\frac{3}{2}kT = \delta\frac{1}{2}mv_m^2 \tag{37}$$

During the mean transit time, the mean energy $0.5m(2v_E)^2$ is accepted by a charged particle from the electric field. During the following collision with a gas molecule, the mean energy $1.5\delta kT$ is accepted from the thermal energy [Eq. (4)] of the gas molecules with gas temperature T. From the total energy $0.5mv_m^2$ of the charged particle the mean fraction $\delta 0.5mv_m^2$ is transferred to the gas molecules during collisions. Equation (37) is based on the fact that the final velocity v_m is reached when the mean accepted energy is equal to the mean transferred energy. Without an electric field the same result as in Eq. (4) must be obtained:

$$\frac{1}{2}mv_m^2 = \frac{3}{2}kT \tag{38}$$

As only a single charged particle is considered and the velocity change on the free path is negligible, v_m is equal to v_{eff}. From Eqs. (35)–(37), the total directed drift velocity v_E is calculated:

$$v_E^2 = \frac{\delta}{4}\frac{3kT}{2m}\left[\sqrt{1+\frac{1}{\delta}\left(\frac{2qE\lambda_m}{3kT}\right)^2}-1\right] \tag{39}$$

Two different cases are considered.

CASE 1

$$qE\lambda_m \ll \frac{3}{2}kT\sqrt{\delta}$$

or with Eq. (21)

$$\frac{E}{p} \ll \text{const}\sqrt{\delta} \tag{40}$$

In this case, the energy accepted on the free path from the electric field is much smaller than the energy transferred by collisions. As for electrons, according to Eq. (33) $\delta_e \ll 1$. This condition is fulfilled only for very small values of the reduced field $E/p \leq 5$ V/cm. For ions according to Eq. (34) $\delta_I \approx 0.5$. This condition is fulfilled for normal field stress. Then Eq. (39) is approximated by:

$$v_E = \frac{1}{2}\frac{q\lambda_m}{\sqrt{3kTm}}E \tag{41}$$

According to Eq. (30) the mobility b is not dependent on the electric field:

$$b = \frac{1}{2}\frac{q\lambda_m}{\sqrt{3kTm}} = \text{const.} \tag{42}$$

Equation (41) can also be obtained from a simpler model. Therefore it is assumed that thermal movement is nearly undistorted by the electric field. In that case the mean transit time $\tau_m = \lambda_m/v_m$, and the mean field-induced drift velocity is given by

$$v_E = \frac{1}{2}\frac{q}{m}\frac{\lambda_m}{v_m}E \tag{43}$$

With Eq. (38) we obtain Eq. (41). The mobility of some singly charged ions is shown in Table 3 (1).

CASE 2

$$qE\lambda_m \gg \frac{3}{2}kT\sqrt{\delta}$$

or with Eq. (21)

$$\frac{E}{p} \gg \text{const}\sqrt{\delta} \tag{44}$$

For electrons ($\delta_e \ll 1$) this condition is met for fields which are usual in the field of gaseous dielectrics. For ions ($\delta_I \approx 0.5$)

Table 3. Mobility of Positive and Negative Ions at 1 Bar and 20°C for Very Low Electric Fields[a]

Gas	$b+$, cm²/Vs	$b-$, cm²/Vs
H_2	6.7	7.9
N_2	1.6	—
O_2	1.4	1.8
CO_2	1.1	1.3
SF_6	0.8	0.8

[a] Ref. 1.

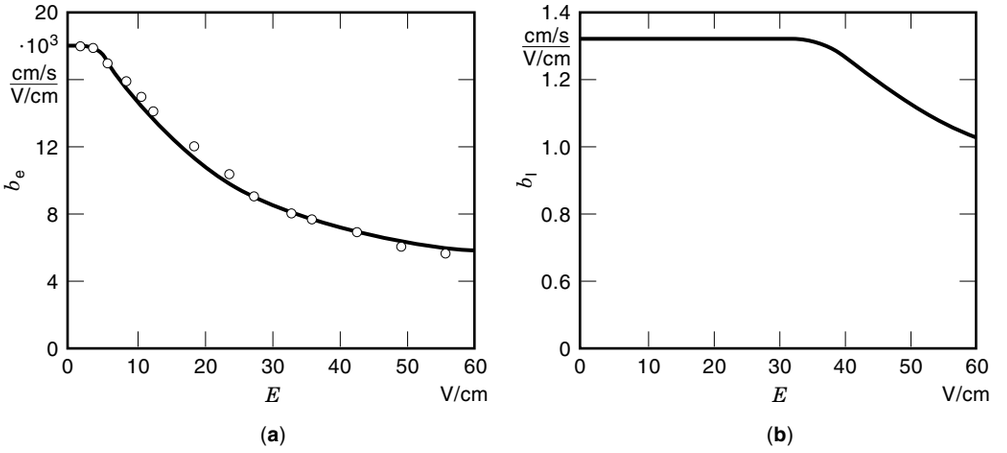

Figure 6. (a) Electron mobility in N_2 at 1 bar and 20°C (4). (b) Ion mobility in Ar at 1 bar and 20°C (4).

this condition is met at very high related fields E/p, which occur only at very low gas pressure. Then Eq. (39) is approximated by

$$v_E = \frac{1}{2}\sqrt{\frac{\sqrt{\delta}\, q\lambda_m}{m}}\,\sqrt{E} \tag{45}$$

According to Eq. (30), the mobility

$$b = \frac{1}{2}\sqrt{\frac{\sqrt{\delta}\, q\lambda_m}{m}}\,\frac{1}{\sqrt{E}} = \text{const}\,\frac{1}{\sqrt{E}} \tag{46}$$

decreases with increasing field.

Equation (46) is also obtained by an energy consideration. In this case the thermal energy may be neglected. It is assumed that during each collision the fraction $\delta 0.5 m v_m^2$ of the energy of the charged particle is transferred. The direction of the velocity vector is distributed equally. The mean total velocity v_E is reached when the energy being accepted between two collisions from the field $0.5m(2v_E)^2$ is equal to the energy being transferred by the collision:

$$\frac{1}{2}m(2v_E)^2 = \delta\frac{1}{2}mv_m^2 \tag{47}$$

Combining Eqs. (35) and (36) we obtain Eq. (46). In Fig. 6 examples for the electron and ion mobility (positive) are shown (4). For electrons the mobility is high and constant only for very low fields. For ions this range is extended to much higher fields (Case 1). For very high fields the ion mobility is also decreased (Case 2).

The calculation is based on a very simple model. More precise results are obtained if the velocity and the mobility according to Eqs. (39), (41), (42), (45), and (46) are multiplied by a correction factor a. For electrons this factor $a \approx 0.7$ and for ions $a \approx 1.15$.

For further application it is useful to note some specific facts and data. Heavy ions have a low but constant mobility. Light weight electrons have a very high mobility, which depends on the electric field. For air at 1 bar, 0°C, and in a breakdown field of approximately 30 kV/cm, the following data are obtained:

$$b_{\text{electron}} = b_e \approx 500\,\frac{\text{cm}^2}{\text{Vs}} \qquad b_{\text{ion}} = b_I^+ \approx b_I^- \approx (1\cdots 2)\,\frac{\text{cm}^2}{\text{Vs}} \tag{48}$$

$$v_{E(\text{electron})} \approx 150\,\frac{\text{mm}}{\mu\text{s}} \qquad v_{E(\text{ion})} \approx (0.3\cdots 0.6)\,\frac{\text{mm}}{\mu\text{s}} \tag{49}$$

For many calculations, especially for a short time stress with an impulse voltage, the ions can be approximately assumed as stationary. In SF_6, the mobility of ions of both polarities is approximately 0.7 cm^2/Vs and for electrons it is approximately 150 cm^2/Vs.

The movement of the charged particles and the current flow can be calculated from the mobility b. In addition for processes in gas discharges the energy of the charged particles is also of great interest. The final energy W of a charged particle is reached when the following energy balance is reached. On the mean free path λ_m from the electric field E the energy $qE\lambda_m$ is accepted, and it must be equal to that energy δW, which is transferred by the following collision:

$$W = q\,\frac{\lambda_m}{\delta}\,E \tag{50}$$

Accordingly, an effective mean free path λ_m^* can be defined as

$$\lambda_m^* = \frac{\lambda_m}{\delta} \tag{51}$$

which in the case of electrons ($\delta_e \ll 1$) is much higher than the true mean free path between successive collisions.

IONIZATION, EXCITATION, AND ATTACHMENT

In gas discharges, only charged particles are affected by the electric field. Therefore either charged particles must be available in the gas volume before application of the electric

field or they must be injected from outside, for instance, from electrodes. Usually only a few charged particles are available, and conduction is obtained only by multiplication of the charged particles.

In a gas volume, charged particles can be generated by electron detachment from neutral molecules. On solid surfaces, electrons may be released from the surface. Therefore volume ionization and surface ionization must be distinguished.

Energy Levels

To explain ionization processes, a simple model is presented. An atom with atomic number z has z charges in the core and z electrons with negative charge $e = -1.6 \times 10^{-19}$ C, which move on circular paths on the different levels K, L, M, . . . (Fig. 7). Those paths are determined by the balance between coulombic force F_q and centrifugal force F_z:

$$F_z = \frac{m_e v_e^2}{r_e} = F_q = \frac{e(ze)}{4\pi\epsilon_0 r_e^2} \tag{52}$$

where the electron mass is m_e, the electron velocity v_e, and the electric field constant ϵ_0. The coulombic force of the other electrons is neglected.

The rotational momentum P_e of an electron is given by

$$P_e = m_e v_e r_e \tag{53}$$

From quantum theory only discrete values of the energy and of the rotational momentum are possible which are given by

$$P_e = n\frac{h}{2\pi}, \qquad n = 1, 2, 3, \ldots \tag{54}$$

Therefore

$$h = 6.625 \times 10^{-34}\,\text{Js} = 4.135 \times 10^{-15}\,\text{eV s} \tag{55}$$

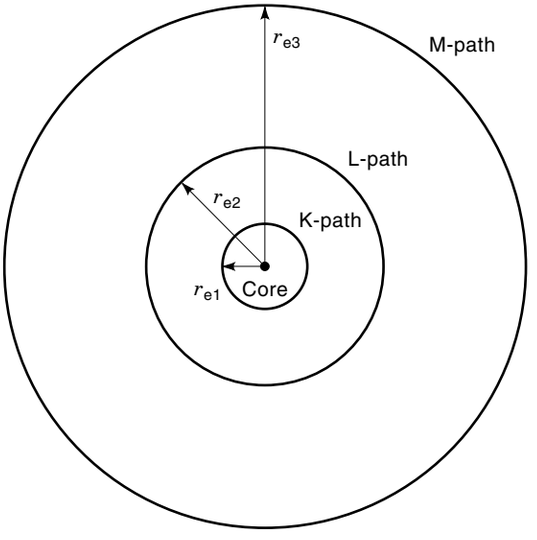

Figure 7. Atomic model: core diameter $\approx 10^{-15}$ m; diameter of the outer path $\approx 10^{-10}$ m.

is Planck's constant. From Eqs. (52)–(54)), the radius r_{en} of the nth discrete electron path is given by

$$r_{en} = \frac{1}{\pi}\frac{h^2\epsilon_0}{m_e e^2}\frac{n^2}{z} = 0.529\frac{n^2}{z} \times 10^{-10}\,\text{m} \tag{56}$$

The energy of electrons on different levels is decisive for ionization processes. The total electron energy consists of the kinetic energy W_{kin}, which is determined by the mass, and the potential energy E_{pot}, which is determined by the charge. From

$$W_{kin} = \frac{1}{2} m_e v_e^2 \tag{57}$$

and Eq. (52) we obtain

$$W_{kin} = \frac{1}{8\pi\epsilon_0}\frac{e^2 z}{r_e} \tag{58}$$

The potential energy of an electron due to the charge of the core is given by

$$W_{pot} = -\frac{1}{4\pi\epsilon_0}\frac{e^2 z}{r_e} = -2W_{kin} \tag{59}$$

If the electron is released from the atom ($r_e \to \infty$), its potential energy is zero. The total binding energy of an electron is given by

$$W_{tot} = W_{kin} + W_{pot} = \frac{1}{2}W_{pot} = -\frac{1}{8\pi\epsilon_0}\frac{e^2 z}{r_e} \tag{60}$$

According to Eq. (56), the binding energy of an electron on the nth level is given by

$$W_{tot} = -13.61\frac{z^2}{n^2}\,\text{eV} = -W_I \tag{61}$$

Because this energy is required to release electrons from the atom, it is called ionization energy W_I. If an electron is collected by such a positive ion, the ionization energy is released by recombination radiation.

Before an electron is released by ionization, it can be moved by a lower amount of energy from a lower level (inner circle) to a higher level (outer circle). This process is called excitation. When the electron returns to the original level, the same energy is released by radiation. Normally electrons move on the inner levels. Therefore each level contains a maximum number of electrons. The excitation energy W_A between the νth level and the μth level, according to Eq. (61) is given by

$$W_A = 13.61 z^2 \left(\frac{1}{\nu^2} - \frac{1}{\mu^2}\right)\,\text{eV} \tag{62}$$

When electrons return from the excited state to the basic state, the excitation energy W_A is released, and the corresponding radiation with frequency f and wavelength λ is emitted. From the velocity of light $c_0 = 2.998 \times 10^8$ m/s, we obtain

$$W_A = hf = h\frac{c_0}{\lambda} \tag{63}$$

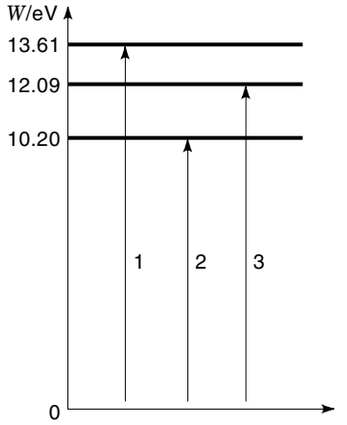

Figure 8. Energy scheme of the hydrogen atoms (H); 1—ionization energy 13.61 eV, 2—1. excitation energy 10.2 eV, 3—2. Excitation energy 12.09 eV.

and the wavelength of the radiation is given by

$$\lambda = \frac{c_0 h}{W_A} = \frac{1240}{W_A/\text{eV}}\,\text{nm} \tag{64}$$

In Fig. 8 an energy scheme for the hydrogen atom ($z = 1$) with the excitation energy and the ionization energy is shown. As only discrete excitation levels are possible, only discrete wavelengths of the radiation can be generated. Therefore the emission spectrum of atomic gases is a line spectrum. The wavelengths are mainly in the lower visible range and in the UV range. For the simple hydrogen atom the experimental data are in good agreement with the model. For atoms with higher numbers, the interaction between the electrons must also be taken into account.

The excitation and ionization energy for some important gases are given in Table 4 (1). For atoms or molecules with more than one electron, multiple ionization is also possible. The levels given in Table 4 are valid only for the release of the first electron from a neutral particle. To release further electrons, much higher energies are required. However such processes in general are not relevant for gas discharges, as such high energy is not available.

The lifetime of an excited state is very short (10^{-8} s). If no further processes occur, the excited electrons return to the basic state according to a statistical distribution. Thereby a photon is emitted, which may excite or ionize other atoms.

Table 4. Excitation Energy to the First Excited Level and Ionization Energy for the First Electron[a]

Gas	Excitation Energy W_A, eV	Ionization Energy W_I, eV
H	10.2	13.6
H_2	10.8	15.9
N_2	6.3	15.6
O_2	7.9	12.1
CO_2	10.0	14.4
SF_6	6.8	15.6
He	19	24

[a] Ref. 1.

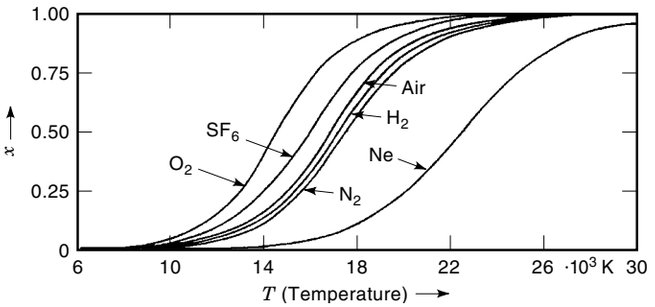

Figure 9. Ionization degree x of thermoionized gases at 1 bar (5).

Additionally, metastable excited states can occur. Then according to quantum theory, the transition of the excited electron back to the stable state cannot occur directly. A transition to an intermediate state is required. Also in such cases when the energy of a photon or a collision is not sufficient for direct ionization, a stepwise ionization process may occur. Then the energy must be sufficient for excitation and during the duration of the excited state a further, rather low energy transfer can cause ionization. However during the short times relevant, this energy transfer usually has to occur by short wavelength radiation of high intensity, which is usually not available in gas discharges.

Because of the relatively long duration of metastable states in noble gases (up to 0.1 s), a stepwise ionization by impact processes with rather small energy and accordingly low electric fields is possible (gas discharge lamps). For high molecular gases, ionization and dissociation will occur together because in many cases the generated positive ions are not stable.

Volume Ionization

Thermoionization. In gases at high temperature, molecules may ionize by collision. According to the Boltzmann–Maxwell velocity distribution, temperatures of some 1000 K are required for significant ionization.

The ionization degree x can be calculated from the Saha equation. The result is shown in Fig. 9 (5):

$$\frac{x^2}{1-x^2} = 0.182\,\frac{T^{2.5}}{p}\exp\left(-\frac{W_I}{kT}\right)\cdot\frac{\text{bar}}{K^{2.5}} \tag{65}$$

For gas discharges, thermoionization is relevant only during the final phase. In that state, a highly conductive channel is formed due to the heating of the gas caused by high-energy dissipation.

Photoionization. By absorbing a photon of sufficient quantum energy, photoionization can occur. According to the necessary ionization energy high frequency

$$h f \geq W_I \tag{66}$$

or short wavelength [Eq. (63)]

$$\lambda \leq \frac{c_0 h}{W_I} \tag{67}$$

Table 5. Wavelength and Quantum Energy of Electromagnetic Radiation[a]

Radiation	Wavelength, nm	Quantum Energy, eV
Infrared	750–10000	0.12–1.65
Visible	450–750	1.65–2.75
Ultraviolet (UV)	150–380	3.26–8.27
Vacuum ultraviolet	15–150	8.27–82.7
X rays	0.01–0.15	$8.2 \cdot 10^3$–$124 \cdot 10^3$
γ radiation	0.0005–0.01	$1.24 \cdot 10^5$–$2.5 \cdot 10^6$
Cosmic radiation	<0.0005	$>2.5 \cdot 10^6$

[a] Ref. 1.

of the radiation is required. In normal gases such ionization processes require radiation with a wavelength of 65 $\cdots$ 100 nm (Table 4). With UV radiation of wavelength approximately 200 nm in such gases only the energy W_A and $W_I - W_A$ (Table 4) can be provided and only stepwise photoionization can occur (Table 5). By photoionization the primary electrons, required for gas discharges, are provided. The source for the radiation may be terrestrial with energy levels up to some MeV or cosmic with energy levels up to 60 MeV. The latter has such high energy, that usual enclosures do not have any screening effect.

Collision Ionization. Multiplication of charged particles in a gas is achieved by collision. Again a simple model can be used, where now the inelastic collision of two balls has to be considered. If the initial kinetic energy of particle 1 is W, the maximum potential energy ΔW_{pot} transferred to stationary particle 2 can be calculated (3):

$$\frac{\Delta W_{pot}}{W} = \frac{m_2}{m_1 + m_2} \tag{68}$$

According to this model, for an electron ($m_1 \ll m_2$) the total energy is transferred to a molecule. An ion ($m_1 \approx m_2$) can transfer only 50% of its kinetic energy. For direct ionization, the precondition is $\Delta W_{pot} \geq W_I$, and for stepwise ionization the lower energy levels $\Delta W_{pot} \geq W_A$ and $\Delta W_{pot} \geq W_I - W_A$ are sufficient. Therefore electrons are more effective for collision ionization. Due to the 5.6-times larger mean free path [Eq. (25)] and due to the large effective free path λ^* [Eq. (51)] the energy of electrons in a gas is much higher than that of the ions. Therefore multiplication of charged particles can be calculated by considering electron collision alone.

The ionization coefficient α is the number of collisions causing ionization per unit length. This important coefficient strongly depends on the field. According to the effective free path λ/δ, the energy of the electrons is given by

$$W = eE \frac{\lambda}{\delta} \tag{69}$$

Therefore stepwise ionization is neglected. Only if the energy is as high as the ionization energy W_I, according to this model ionization occurs. The corresponding free path λ is called λ_I:

$$\lambda_I = \frac{\delta W_I}{eE} \tag{70}$$

According to Eq. (29), the probability P for a free path $\lambda \geq x = \lambda_I$ is given by

$$P = \exp\left(-\frac{\lambda_I}{\lambda_m}\right) \tag{71}$$

The mean number of all collisions per unit length is $1/\lambda_m$. Therefore one electron will cause α ionizations per unit length:

$$\alpha = \frac{1}{\lambda_m} \exp\left(-\frac{\lambda_I}{\lambda_m}\right) \tag{72}$$

Townsend's first ionization coefficient α is the key factor for multiplying charged particles. According to Eq. (21), provided that the collision cross section is constant, the mean free path λ_m, is inversely proportional to the gas pressure. Therefore, it is appropriate to calculate the reduced ionization coefficient α/p. Combining this with Eq. (70), we obtain the following result:

$$\frac{\alpha}{p} = C_1 \exp\left(-\frac{C_2}{E/p}\right)$$

where

$$C_1 = \frac{a_s}{kT}$$

and

$$C_2 = \frac{a_s \delta W_I}{ekT} \tag{73}$$

In Table 6 some data for C_1 and C_2 in different gases are listed. Due to the simplicity of the model being used the validity is limited as indicated.

In Figs. 10 (6) and 11 (7) data for the ionization coefficient α and the attachment coefficient η in air and SF_6 are shown. From that data the effective ionization coefficient α-η is also calculated. A simple description of the processes may be obtained, if the term ionization cross section is introduced. If according to Fig. 3 an electron A is passing through gas B, the ionization cross section a_{sI} is given by the assumption that all collision processes corresponding to the ionization cross section are causing ionization. In the same way, cross sections for other interactions in the gas can be defined, that is, excitation, attachment, or recombination. With the ionization cross section, the probability for ionization dw_I of an electron on its zigzag path ds is described by Eq. (18):

$$dw_I = n_B a_{sI}(v)\, ds \tag{74}$$

Table 6. Values for C_1 and C_2

Gas	C_1, $(\text{cm} \cdot \text{bar})^{-1}$	C_2, kV/(cm · bar)	Validity for E/p, kV/(cm · bar)
H_2	3760	97.7	110–300
N_2	9770	255	75–450
CO_2	15000	349	370–750
Air	11300	274	110–450

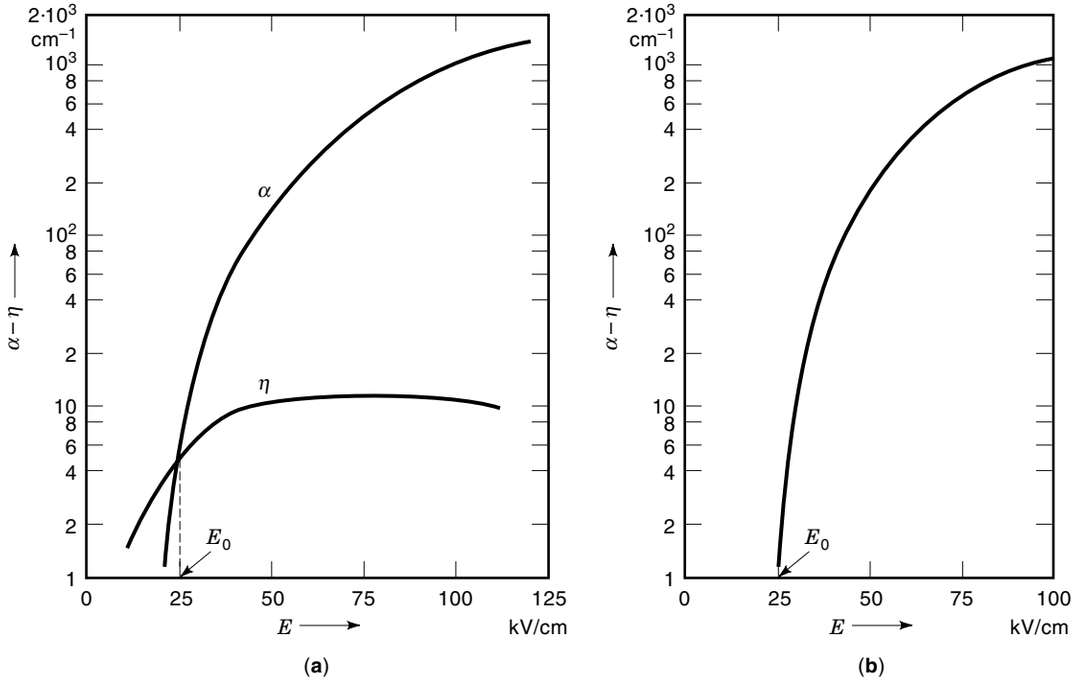

Figure 10. (a) Ionization coefficient α, attachment coefficient η, and (b) effective ionization coefficient $\alpha - \eta$ for air at 1 bar (6).

Thereby molecules B are regarded as stationary. It is important that the ionization cross section depends on the energy, that is, the velocity v of the electrons. Some data for the ionization cross section are given in Fig. 12 (8,9).

The velocity distribution of the electrons is determined by the thermal movement, according to Eq. (1), and the superimposed directed movement caused by the electric field. The quantity of electrons $dN_{(v)}$, which have a velocity v, are considered. The probability that these electrons will cause ionization on their path ds is given by

$$\Delta w_{\mathrm{I}} = \frac{dN_{\mathrm{v}}}{dv}\,dv\,dw_{\mathrm{I}} = n_{\mathrm{B}} a_{\mathrm{sI}}(v)\,\frac{dN_{\mathrm{v}}}{dv}\,dv\,ds \tag{75}$$

The total number of electrons is given by

$$N_{\mathrm{A}} = \int_{v=0}^{v=\infty} \frac{dN_{\mathrm{v}}}{dv}\,dv \tag{76}$$

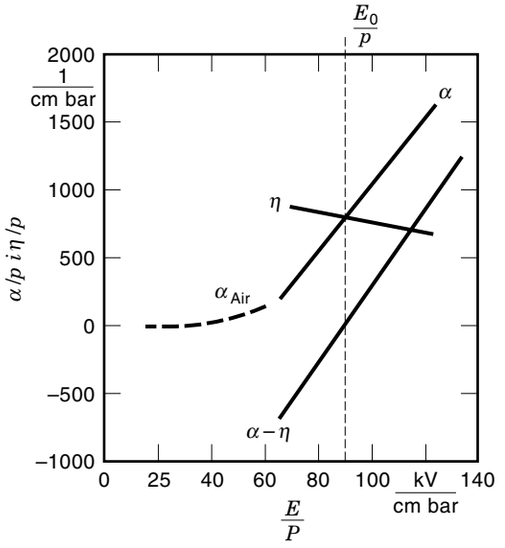

Figure 11. Reduced ionization coefficient α/p, reduced attachment coefficient η/p, and reduced effective ionization coefficient $(\alpha - \eta)/p$ for SF_6; for comparison α/p for air is also plotted; $t = 20°C$ (7).

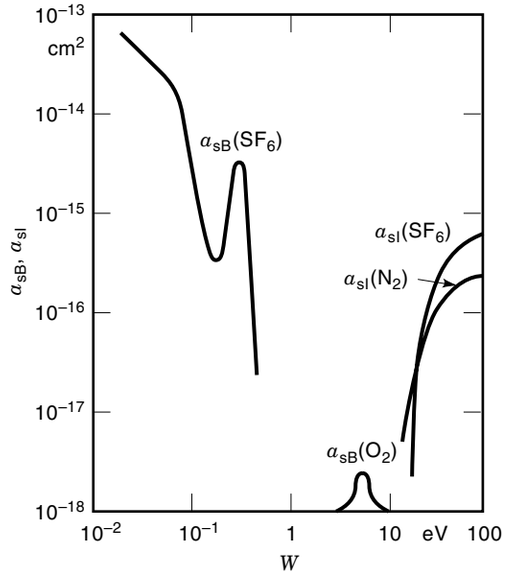

Figure 12. Ionization cross section a_{sI} for N_2 and SF_6; attachment cross section a_{sB} for SF_6 and O_2 (8,9).

Table 7. W_a for Different Electrode Materials[a]

Material	W_a, eV
Barium oxide	1.0
Cesium	0.7–1.86
Aluminum	1.77–3.95
Copper	3.89–4.82
Gold	4.33–4.90
Nickel	3.68–5.02

[a] Ref. 4.

For ionization, the path dx of the electrons opposite to the direction of the electric field is relevant. This can be calculated according to the relevant velocities

$$\frac{ds}{dx} = \frac{v}{v_E} \tag{77}$$

where v_E is the directed, field-dependent drift velocity. For all electrons N_A the probability for ionization W_I is given by

$$W_I = \left(\int_{v=0}^{v=\infty} \frac{dN(v)}{dv} a_{sI}(v) \frac{v}{v_E} dv \right) n_B dx \tag{78}$$

According to the definition of the (collision) ionization coefficient α, the probability for ionization for N_A electrons on the path dx must be

$$W_I = N_A \alpha \, dx \tag{79}$$

The result for α is

$$\frac{\alpha}{n_B} = \frac{1}{N_A} \int_{v=0}^{v=\infty} \frac{dN(v)}{dv} a_{sI}(v) \frac{v}{v_E} dv \tag{80}$$

At constant temperature, the molecular density n_B is proportional to the gas pressure p. Equation (80) is a physical explanation of the reduced ionization coefficient α/p. Obviously α/p is greatly influenced by the ionization cross section of the electrons.

Surface Emission

Electrons are released from a cathode if the relevant binding forces are overcome. Therefore energy W_a is required:

$$W_a = eV_a \tag{81}$$

Some values for W_a are given in Table 7. Barium oxide and cesium have especially low values, which allows application in vacuum tubes with high cathode emission. The energy W_a can be provided in the following ways.

Field Emission. Electrons are released from metallic conductors if the potential difference caused by the internal (atomic) field is overcome. However, this requires very high external fields, which are reached only in pressurized gases. For plane electrodes with smooth surfaces, fields on the order of 1 MV/cm are required.

Actually the structure of electrodes is far from being ideally smooth. At least the microstructure is usually distorted by protrusions and contamination. Therefore the fields are usually significantly higher than expected from a calculation of the electrostatic field distribution according to the macroscopic electrode geometry. In practice this effect becomes effective for macroscopic fields on the order of some 100 kV/cm.

Thermoemission. Electrons are released from metallic conductors if the temperature is increased. Thereby the thermal energy of the electrons in the metal is increased accordingly, and an increasing number of electrons overcome the existing potential difference. The emission current density S can be approximated according to the Richardson equation:

$$S = CT^2 \exp\left(-\frac{W_a}{kT}\right)$$

where

$$C = 60 \cdots 120 \frac{\mathrm{A}}{\mathrm{cm}^2 \cdot \mathrm{K}^2} \tag{82}$$

Photoemission. Photons release electrons from solid materials, if their energy hf is greater than the required energy W_a. The initial velocity v of the electrons is given by

$$v = \sqrt{\frac{2}{m}(hf - W_a)} \tag{83}$$

According to Eq. (63), the following condition for the radiation wavelength λ must be fulfilled for emission of electrons ($v \geq 0$):

$$\lambda \leq \frac{hc_0}{W_a} \tag{84}$$

A comparison of the energy values in Table 7 with the values of the ionization or excitation energy shows that for photoemission, radiation with a longer wavelength is sufficient compared with gas ionization. The number of emitted electrons per photon is given by the photoionization coefficient η_{ph}.

Secondary Electron Emission (γ-Process). Positive ions release electrons by collision with the cathode surface. Thereby a first electron is needed to neutralize the ion. To generate an additional electron, the energy $2W_a$ is required, which has to be provided by the kinetic energy W_{kin} of the ion and the released ionization energy W_I.

$$\frac{m}{2}v^2 + W_I \geq 2W_a \tag{85}$$

The number of emitted photons per ion is given by γ_I, the so-called second Townsend ionization coefficient. As in Eq. (85) W_I is usually much higher than the kinetic energy. γ_I does not depend very much on the field, rather than on the kind of gas and the electrode material. For air, SF_6, and commonly used electrodes, γ_I is on the order of 10^{-5} (Fig. 20).

Recombination of Carriers

During the movement of charged particles of different polarity, recombination may occur. Thereby the collision frequency

and the reduction of the density of the charged particles dn by recombination are proportional to the density n^+ of the positive and n^- of the negative particles. With the recombination coefficient r,

$$\frac{dn}{dt} = -r\,dn^+\,dn^- \tag{86}$$

Frequently it can be assumed that $n^+ = n^- = n$:

$$\frac{dn}{dt} = -r\,n^2 \tag{87}$$

Then the solution of Eq. (87) is

$$n = \frac{1}{\dfrac{1}{n_0} + rt} \tag{88}$$

with the initial density of charged particles n_0. Because of recombination, the density n of the charged particles is reduced to half of the initial value after t_H:

$$t_H = \frac{1}{n_0\,r} \tag{89}$$

The recombination coefficient r depends on the molecular density, that is, the gas pressure. Caused by cosmic radiation (see Photoionization), approximately a constant production rate of charged particles by ionization $(dn/dt)_0$ per unit volume and time is achieved. Therefore at a density n_0 of charged particles, a balance is achieved if the recombination rate according to Eq. (87) is equal to the production rate:

$$\left(\frac{dn}{dt}\right)_0 = r\,n_0^2 \tag{90}$$

$$n_0 = \sqrt{\frac{1}{r}\left(\frac{dn}{dt}\right)_0} \tag{91}$$

This density of charged particles is very important for the inception of gas discharges. As long as the energy of the charged particles is not sufficient to allow ionization, only n_0 charged particles can contribute to conduction. Ionization processes also start from those. Therefore usually only the electrons are relevant (see Collision Ionization).

For air at $p = 1$ bar and $T = 0°C$, the following data can be used:

$$\begin{aligned} n_0 &= 500\,\mathrm{cm^{-3}} \qquad r = 8 \times 10^{-6}\,\mathrm{cm^3 \cdot s^{-1}} \\ t_H &= 250\,\mathrm{s} \qquad (dn/dt)_0 = 2\,\mathrm{cm^{-3} \cdot s^{-1}} \end{aligned} \tag{92}$$

However the cosmic radiation has a high temporal scatter and increases with altitude. The terrestrial radiation depends on location. Therefore the ion density of air strongly depends on location and atmospheric conditions.

Electron Attachment

Free electrons attach to molecules resulting in the formation of negative ions. By attachment, the number of charged particles is not influenced. However the number of free electrons in the gas is reduced. The free electrons, however, are relevant for ionization and multiplication of the charged particles in the gas (see Collision Ionization). Therefore discharge development is greatly impeded by attachment. The binding energy of attached electrons (electron affinity) is very high for halogens, because those in the basic state have a free space in the outer electron shell. The electron affinity W_B for some elements is given in Table 8 (7,8,10).

Table 8. Electron Affinity W_B of Some Elements and Gases[a]

Element	Electron Affinity W_B, eV
H	0.7
F	3.4
Cl	3.6
O	1.4
O_2	0.4
SF_6	(0.05–0.1)[b] 1.0–1.7

[a] Refs. 7, 10.
[b] Initial values; after some 10 μs the second range of values applies.

Therefore all combinations containing halogens have a high potential for attachment of electrons and the formation of negative ions. All gases with these characteristics are called electronegative gases. Sulfur hexafluoride (SF_6) is the most frequently used electronegative gas with an initial electron affinity of approximately 0.05 to 0.1 eV. After some 10 μs the electrons are attached more strongly, resulting in an increased electron affinity of 1.0 up to 1.7 eV. On the other hand, in electronegative gases electrons may be released again if this rather low energy, compared with the ionization energy given in Table 4, is provided. Without an applied electric field the thermal energy is usually so low that most of the electrons are attached, which results in a high number of negative ions and only a few free electrons.

Different attachment processes are possible. The result is described by the attachment cross section a_{sB}. Some data are given in Fig. 9 for SF_6 and O_2. The high attachment cross section of SF_6, especially at low energy, is an important feature of this gas. Because the attachment cross section of O_2 is much lower and N_2 as the main component of air does not attach any electrons, the total attachment in air is very low (Fig. 10).

During discharge development, the number of free electrons is also significantly influenced by attachment. This is described by the attachment coefficient η, which is the relative reduction of the number of electrons per unit length, that is, the probability of attachment for an electron per unit length. Based on a similar mechanism, the attachment coefficient can be calculated from Eq. (80):

$$\frac{\eta}{n_B} = \frac{1}{N_A}\int_{v=0}^{v=\infty} \frac{dN_v}{dv}\,a_{sB}v\,\frac{v}{v_E}\,dv \tag{93}$$

Because gas pressure p at constant temperature is proportional to molecular density n_B, the reduced attachment coefficient η/p depends mainly on the attachment cross section $a_{sB}v$. Therefore similar to $a_{sB}v$ the attachment coefficient depends on the electron velocity v, that is, the electron energy.

The attachment coefficient can also be described by a simple model. Based on the model for collision ionization (see Collision Ionization) it is assumed that attachment always occurs, if the energy of the particle is smaller than the electron

affinity W_B. Therefore the free path λ must be smaller than the free path for attachment λ_B. From Eq. (69) the effective free path is given by

$$\frac{\lambda}{\delta} < \frac{\lambda_B}{\delta} = \frac{W_B}{eE} \tag{94}$$

This consideration can be continued in the same way as for collision ionization. From Eq. (29) the probability for a free path $\lambda < x = \lambda_B$ is given by

$$P = 1 - \exp\left(-\frac{\lambda_B}{\lambda_m}\right) \tag{95}$$

Based on the mean number of collisions $1/\lambda_m$ per unit length, the probability for attaching an electron per unit length is given by

$$\eta = \frac{1}{\lambda_m}\left[1 - \exp\left(-\frac{\lambda_B}{\lambda_m}\right)\right] \tag{96}$$

The mean free path is inversely proportional to the gas density [Eq. (20)], that is, the gas pressure at constant temperature. Combined with Eq. (95) a description similar to the ionization coefficient is obtained:

$$\frac{\eta}{p} = C_4\left[1 - \exp\left(-\frac{C_3}{E/p}\right)\right] \tag{97}$$

Comparing the results of Eq. (97) with the experimental data shown in Fig. 11 for the attachment coefficient in SF_6 proves the validity of this simple model. However as can be seen from Fig. 10, Eq. (97) should not be applied to describe the attachment coefficient in air.

DISCHARGE DEVELOPMENT

Voltage-Current Characteristics of a Gap

The different mechanisms of conduction in gases can be shown by the voltage-current characteristic of a gap. Between plane–plane electrodes distance d apart, a homogeneous field E is applied according with dc voltage V. If the voltage is increased, the current density S is as shown in Fig. 13.

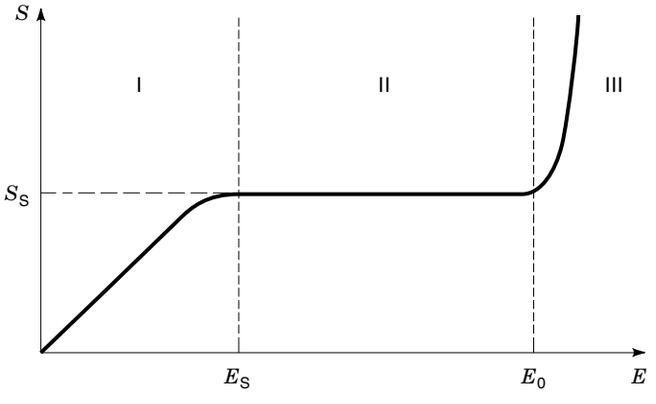

Figure 13. Current density S in a plane-to-plane gap in air with field E.

Range I shows ohmic characteristics. The current density is given by

$$S = eE(n_I^+ b_I^+ + n_I^- b_I^- + n_e b_e) \tag{98}$$

where n_I^+ and n_I^- are the density of the positive and negative ions, n_e is the density of the electrons and the corresponding mobilities are b_I^+, b_I^-, and b_e. For a short time interval, the current is nearly a pure electron current, because the electron mobility b_e is much higher than the ion mobility $b_I^{+,-}$. After the electrons have moved to the electrodes, and this time interval is considered here, only the rather slow ions contribute to the current and the corresponding conductivity σ is given by

$$\sigma = e(n_I^+ b_I^+ + n_I^- b_I^-) \tag{99}$$

As long as the applied field and the energy of the charged particles do not allow ionization, only the initial ions generated by cosmic or terrestrial radiation are available. According to Table 3 and Eq. (92), the following data are valid for air:

$$n_I^+ \approx n_I^- \approx 500\,\mathrm{cm}^{-3} \qquad b_I^+ \approx b_I^- \approx 1.6\,\frac{\mathrm{cm}^2}{\mathrm{V \cdot s}} \tag{100}$$

Therefore in range I the resistivity

$$\rho = \frac{1}{\sigma} \approx 4 \cdot 10^{15}\,\Omega \cdot \mathrm{cm} \tag{101}$$

For impulse-voltage stress, the electron current has to be taken into account, which results in much lower values of resistivity.

In range II the saturation current density S_S is obtained because all charged particles which are generated per unit time and volume by radiation are moved to the electrodes in the same time interval. According to Eq. (90) the charge difference per unit time caused by the particles generated within the electrode volume given by plane A and distance d is given by

$$\frac{dQ}{dt} = e\left(\frac{dN}{dt}\right)_0 = Ad\left(\frac{dn}{dt}\right)_0 e = Adrn_0^2 e \tag{102}$$

This must be equal to the charge difference per unit time based on the saturation current density S_S in the field E_S:

$$\frac{dQ}{dt} = AS_S = E_S(b_I^+ + b_I^-)\, n_0 Ae \tag{103}$$

Therefore the saturation field is given by

$$E_S = k\frac{rn_0 d}{b_I^+ + b_I^-} \tag{104}$$

with $k = 1$. Actually space-charge-induced field distortion has to be included in the calculation, which results in $k = 4.25$. The saturation field depends on the gap width d and amounts to ≈30 V/m for air gaps of $d = 1$ m.

Range III is characterized by a steep current increase caused by collision ionization. In air at 1 bar, a field of ≈25

kV/cm is required for this process, which results in breakdown in homogeneous fields.

Avalanche Formation and Effective Ionization Coefficient

In range III (Fig. 13) an avalanche-like increase of the number of charged particles caused by collision ionization occurs. Thereby the collision ionization coefficient α and in electronegative gases also the attachment coefficient η have to be taken into account. As usual, only electrons cause collision ionization. The increase of the number of electrons dN_e in the distance between the locations x and $x + dx$ opposite to the direction of the electric field is given by

$$dN_e = (\alpha - \eta) N_e \, dx \tag{105}$$

where N_e is the number of electrons at the location x. Starting at $x = 0$, that is, at the cathode, with N_{e0} initial electrons, the number of electrons at the location x has increased to N_{ex}:

$$N_{ex} = N_{e0} \exp\left(\int_0^x (\alpha - \eta)\, dx\right) \tag{106}$$

and for the homogeneous field:

$$N_{ex} = N_{e0} \exp[(\alpha - \eta) x] \tag{107}$$

Therefore α-η is called the effective ionization coefficient, which was shown in Fig. 10(b) for air and in Fig. 11 for SF_6. For fields of $(E/p)_0 < 24.4$ kV/(cm · bar) in air and $(E/p)_0 < 87.7$ kV/(cm · bar) in SF_6, the attachment coefficient dominates. In this condition avalanche growth is not possible and free electrons are attached. if an avalanche develops toward such an area, the number of electrons decreases.

At the reduced limiting field $(E/p)_0$, the steep current increase shown in Fig. 13 occurs. Therefore below this field

$$\begin{aligned} \text{for air } \left(\frac{E}{p}\right)_0 &= 24.4 \frac{\text{kV}}{\text{cm} \cdot \text{bar}} \\ \text{for } SF_6 \left(\frac{E}{p}\right)_0 &= 87.7 \frac{\text{kV}}{\text{cm} \cdot \text{bar}} \end{aligned} \tag{108}$$

breakdown cannot occur. However, the microscopic field, which is relevant for discharge inception, can greatly differ from the macroscopic field. This phenomenon is of special importance in SF_6 (see Surface Effects).

For fields of 60 kV/(cm · bar) $\leq E/p \leq$ 120 kV/(cm · bar), the reduced effective ionization coefficient in SF_6 is approximately:

$$\frac{\alpha - \eta}{p} = k \left[\frac{E}{p} - \left(\frac{E}{p}\right)_0\right]$$

where

$$k = 28 \frac{1}{\text{kV}}$$

and

$$\left(\frac{E}{p}\right)_0 = 87.7 \frac{\text{kV}}{\text{cm} \cdot \text{bar}} \tag{109}$$

For fields of 24.4 kV/(cm · bar) $\leq E/p \leq$ 60 kV/(cm · bar), the reduced effective ionization coefficient in air is approximately (11):

$$\frac{\alpha - \eta}{p} = k \left[\frac{E}{p} - \left(\frac{E}{p}\right)_0\right]^2$$

where

$$k = 0.22 \frac{\text{cm} \cdot \text{bar}}{\text{kV}^2}$$

and

$$\left(\frac{E}{p}\right)_0 = 24.4 \frac{\text{kV}}{\text{cm} \cdot \text{bar}} \tag{110}$$

Breakdown in Homogeneous and Approximately Homogeneous Fields

Evaluation of the Streamer Mechanism. The experimental proof of the streamer mechanism was first performed with impulse-voltage stress in homogeneous fields at rather low gas pressure between 0.35 and 0.7 bar (12). However, those investigations are rather far away from the range which is relevant for technical application, that is, gases of higher specific strength, much higher gas pressure, and less homogeneous field distribution. Therefore some uncertainty remained whether this mechanism could be assumed as a general case for breakdown development.

The following experimental data (13,14) are much closer to technical application because dc voltage stress in approximately homogeneous fields ($\eta = E_{mean}/E_{max} = 0.79$) are investigated, high pressure of several bar is used, and gases of technical relevance, like N_2 and SF_6, are considered. However, under these conditions the dynamics of discharge development are greatly enhanced.

Complete breakdown development in compressed N_2 at 2 bar is reconstructed in Fig. 14 from several high-speed records (single frames) of luminous phenomena with less than 1 ns exposure time by a sampling technique. The application of this technique requires sufficient reproducibility of the discharge development, which has to be verified. The breakdown voltage V_B under these conditions is 59 kV.

The records in Fig. 14 start about 40 ns before the beginning of the voltage collapse ($t = 0$). In frames 1 and 2 an electron avalanche of subcritical size is observed, which drifts toward the anode with a velocity of $\approx 1.5 \times 10^7$ cm/s. The point-like structure of these records is simply due to the low radiation density. The formation of an avalanche of critical size just in front of the anode is shown in frames 3 and 4. The inception of the cathode-directed ionization wave (streamer) can be clearly seen from frame 5, and at frame 11 the streamer has reached the cathode. After that a conductive channel is formed. From these records a propagation speed of the cathode directed streamer of more than 10^8 cm/s is calculated.

There is no doubt that those observations at high pressure represent the same streamer mechanism which has been established for low gas pressure (12). This could also be proven for gas pressures as high as 6 bar in N_2 (13,14). However, under such conditions the timescale for the observations corresponding to Fig. 14 is reduced approximately by a factor of

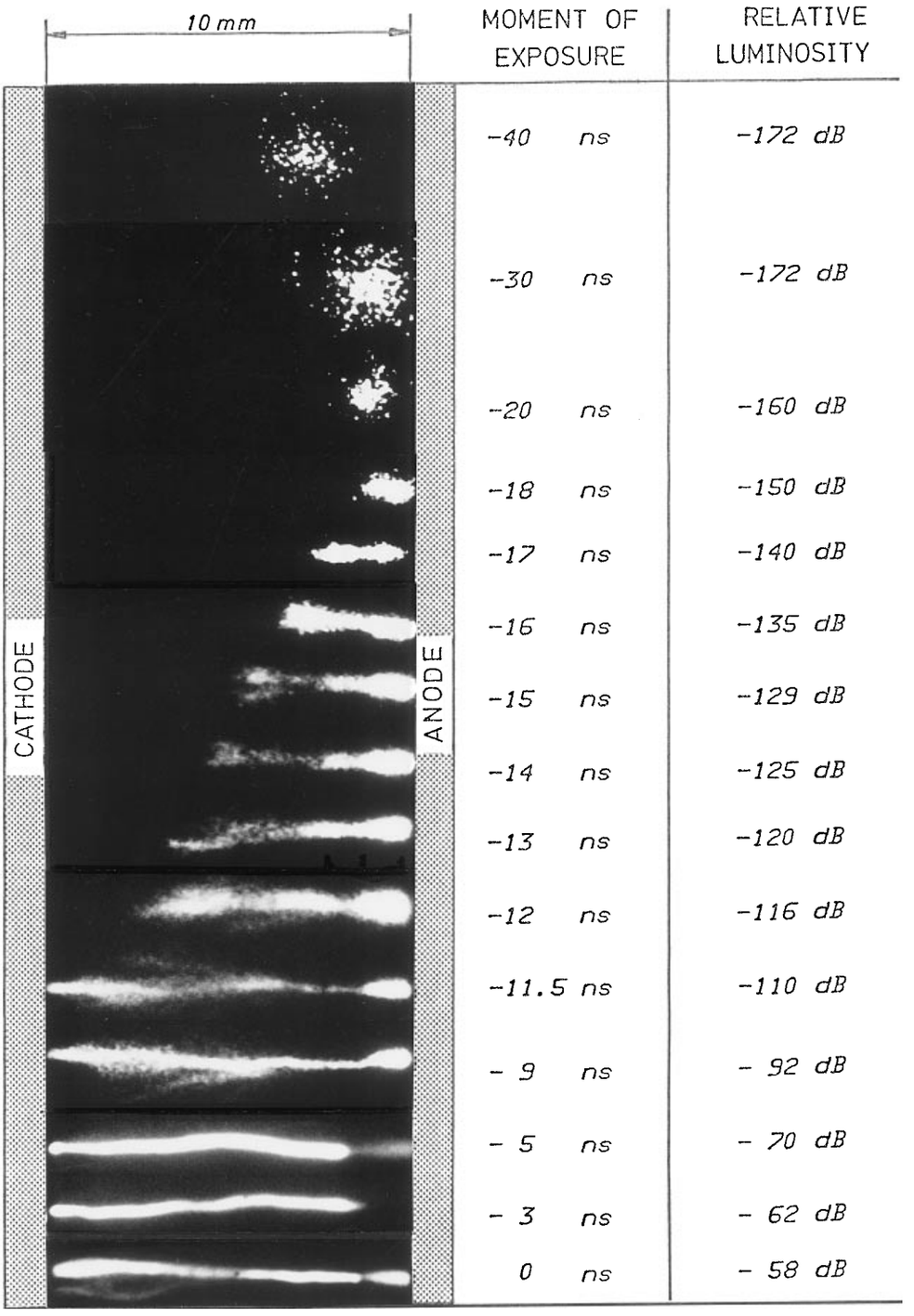

Figure 14. Discharge development in N_2, $p = 2$ bar, $V_B = 59$ kV (13,14).

3, which actually is the relative pressure increase. In SF_6 the observed phenomena also correspond to the streamer mechanism (13,14), if the special conditions are taken into account. Based on high breakdown fields, the timescale of the phenomenon in SF_6 at 2.4 bar is approximately the same as that in N_2 at 6 bar.

A definitive interpretation of the observed discharge phenomenon requires a spectrally resolved analysis. Therefore a technique is used (13,14), which provides both spectral resolution (horizontal axis) and one-dimensional spatial resolution along the electrode axis (vertical axis). An example of these measurements is shown in Fig. 15. Because the measurement was performed in N_2 at $p = 6$ bar, the reduced timescale as described before has to be taken into account.

The first two frames show the radiation from the critical avalanche. The spectral lines belong to the second positive system of the N_2 molecule (15). In frame 3, during the development of the cathode-directed streamer, this radiation is

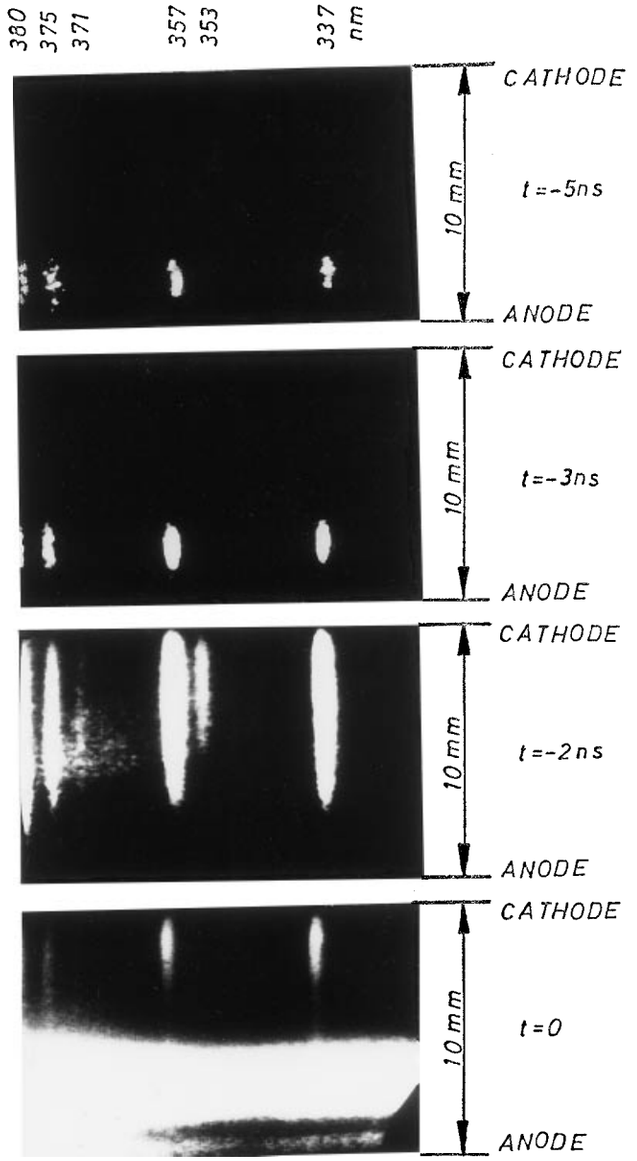

Figure 15. Prebreakdown spectrograms in N_2, $p = 6$ bar, $V_B = 153$ kV, wavelength 318 nm to 382 nm (13,14).

transferred toward the cathode. This indicates that both electron and gas temperature are not influenced significantly (15). In frame 4 the formation of the conductive discharge channel by thermoionization is being observed. This is indicated by the emission of continuous radiation, starting from that region, where the electron avalanche had become critical.

In SF_6 of commercial purity no spectral lines were observed during the discharge formation. Because the radiation coefficient of N_2 is some orders of magnitude higher than that of SF_6 (16,17), tiny additions of N_2 are recognized in the spectrograms. On the other hand, it ensures that small admixtures of N_2 do not influence the insulation properties of SF_6 (18). Therefore it seems to be admissible to use small admixtures of N_2 to indicate those processes in SF_6 which cannot be observed directly. By this method it was verified that the discharge development in SF_6 may also be described by the streamer mechanism.

Taking into account the transfer characteristics of the optical system, the number of photons N_{ph} can be estimated. Based on the radiation coefficient (19) the number of electrons can also be calculated (13). In N_2 it was found that the number of electrons of the critical avalanche is between 1×10^8 ($p = 1$ bar, $t = -20$ ns) and 3×10^8 ($p = 6$ bar, $t = -10$ ns), which agrees very well with other work (15,20).

The corresponding elaboration in SF_6 is restricted to spatial analysis of the prebreakdown phenomena, because the available data for the radiation coefficient are too uncertain to perform the calculation of the number of electrons as done in N_2. As can be seen from the effective ionization coefficient, which is plotted in Fig. 16, in SF_6 electron multiplication is only possible at a distance of 0.45 mm from the cathode and 1.7 mm from the anode because the approximately homogeneous field distribution is used. Based on Eq. (106) the total electron multiplication in front of the cathode is only 10^3, which is not sufficient to generate a critical avalanche. However, in front of the anode the required electron multiplication is obtained within a distance of less than 1 mm.

The records of the prebreakdown phenomena in Fig. 16 show good coincidence between the position of the avalanche tail and the zero passing of the effective ionization coefficient. To get some impression of the reproducibility of the prebreakdown phenomena in SF_6, which is much lower than in N_2, three records for the same experimental conditions are shown. The observed luminous phenomena in SF_6 belong to the formation phase of the critical avalanche and the lowest one already shows the inception of the cathode-directed streamer.

In SF_6 there are some differences in the observed phenomena especially during the streamer inception and propagation phases. So the typical constriction at the avalanche tail cannot be recognized. The branching during the inception of the cathode-directed streamer, which can also be seen in Fig. 14, is not observed in SF_6. Generally there is a bit scatter of the temporal and spatial development of the cathode-directed streamer. The measured propagation velocities vary between 2×10^8 to 5×10^8 cm/s.

Breakdown Criterion According to the Streamer Mechanism. All investigations definitely indicate that the streamer model can be applied to explain breakdown development in gaps with homogeneous and approximately homogeneous field distribution for different gases. With some simplifications breakdown criteria can be derived from such a model. Therefore it is assumed that in a homogeneous electric field an avalanche starts with a single initial electron ($N_{e0} = 1$). The avalanche growth is shown in principle in Fig. 17.

At location x the number of electrons has grown according to Eq. (107):

$$N_e(x) = \exp[(\alpha - \eta)\, x] \tag{111}$$

The avalanche head (2) is formed by the electrons, which are moving with very high speed. The long avalanche tail (1) is formed by the comparatively slow positive ions, which can be considered nearly stationary. Because of diffusion, the electrons in the avalanche head spread equally in all directions. At the time t a charge ball with the radius r_L forms. With the

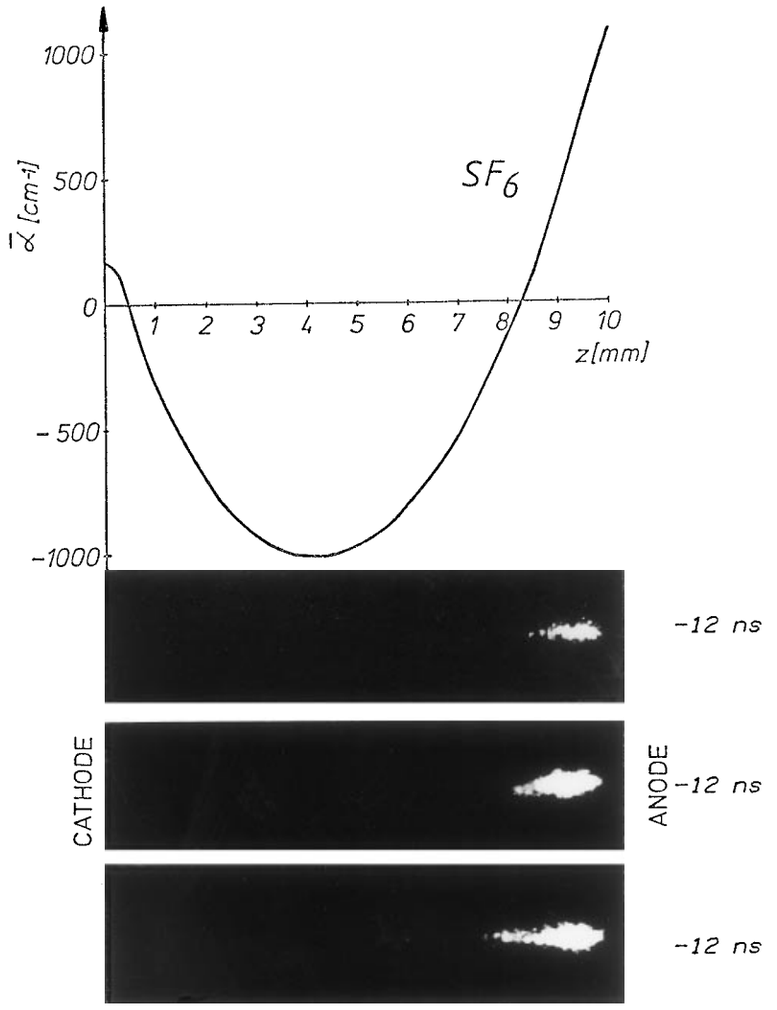

Figure 16. SF_6, $p = 2.4$ bar, $V_B = 198$ kV. Upper part: $\alpha - \eta$; lower part: critical avalanche, $t = -12$ ns (13,14).

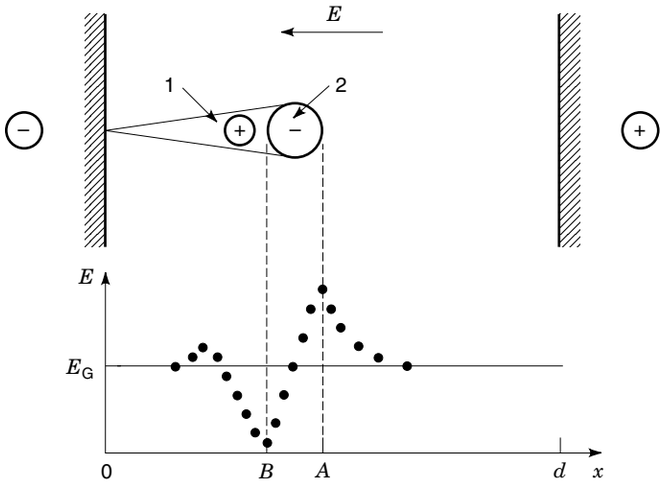

Figure 17. Electron avalanche in a homogeneous field and field distribution in the axis of the avalanche of critical size. E_g is the applied external field. The dotted line is the field resulting from space-charge distortion.

diffusion constant D according to Einstein's law

$$\frac{D}{b_e} = \frac{kT}{e}$$

$$r_L = 2\sqrt{Dt} \tag{112}$$

Because of the spatial distribution of the charged particles, the charge density in the avalanche head is much higher than in the avalanche tail. To evaluate the field distribution near the avalanche head, the charge in the avalanche head alone may be accounted for as an approximation. Therefore a space-charge-induced field E_L is built up. Combining the applied external field E_g (Fig. 17) at location A with the field ($|E_g| + |E_{Lmax}|$) at the location B results in the field ($|E_g| - |E_{Lmin}|$).

Because the increased field at location A in front of the avalanche head, increased ionization and propagation of the avalanche occurs (20). Therefore it is assumed that increased emission of very short wavelength radiation ($\lambda \leq 100$ nm) also plays an important role (12). By this photoionization additional charged particles are obtained and the spatial growth of the discharge development can occur with the velocity of light. During the inception of the anode- and cathode-directed streamers, the low field region corresponding to location B

can be identified as the area with very low emission (Fig. 14, frames 6 to 10).

Because the streamer propagation may be partly accomplished by photons, the effective streamer velocity is very high and in air at atmospheric pressure may already be in the range of 10^7 to 10^8 cm/s. The lower limit is valid for nonhomogeneous fields, the higher for strictly homogeneous fields. When the streamer reaches the electrodes, heating of the prebreakdown channel occurs within a short time interval, followed by thermo-ionization. This results in high conductivity and rapid voltage collapse, provided that the impedance of the voltage source is sufficiently low.

The condition $|E_L| \approx |E_g|$ is regarded as the breakdown criterion. To calculate space-charge field at the avalanche head E_L, it is assumed that the entire electron charge is concentrated in the center of the avalanche head. For avalanche growth, only the basic field E_g is taken into account because space-charge distortion by the charge in the avalanche head can be neglected until the number of electrons is approximately 10^7. Based on the number of electrons at location x [Eq. (111)] the strength of the space charge field is given by

$$E_L = \frac{N_{ex}\, e}{4\pi\epsilon_0 r^2} \frac{e \exp[(\alpha - \eta)x]}{4\pi\epsilon_0 r^2} \tag{113}$$

Based on Eq. (112) and by assuming a constant electron mobility b_e (see Movement of Charged Particles) the radius of the avalanche head can be calculated from

$$r_L^2 = 4D\frac{x}{v_-} = 4D\frac{x}{b_e E_g} \tag{114}$$

With the diffusion constant D from Eq. (112) and the radius of the avalanche head from Eq. (114) the space charge field at the avalanche head is given by

$$E_L = \frac{e^2 \exp[(\alpha - \eta)x]}{16\pi\epsilon_0 kTx} E_g \tag{115}$$

It is assumed that breakdown occurs for $E_L = E_g$. Therefore the avalanche, which started at $x = 0$ (cathode), reaches its critical length x_{cr} and the critical number of electrons N_{cr} in the avalanche head. From Eq. (115)

$$16\pi\epsilon_0 kTx_{cr} = e^2 \exp[(\alpha - \eta)x] = e^2 N_{cr} \tag{116}$$

This condition is fulfilled only if x_{cr} is smaller than or equal to the gap width d. For a homogeneous field and dc voltage stress it can be assumed that the critical size of the avalanche is reached at the anode, that is, $x_{cr} = d$. For a gap width d of 1 cm the result from Eq. (116) is $N_{cr} = 10^8$. As indicated, this value depends on the gap width and on the field distribution. For gap widths of several cm up to some ten cm a critical number of electrons between 10^6 and 10^8 is assumed. Therefore the following breakdown criteria can be used (12,21):

$$\exp\left[\int_0^{x_{cr}} (\alpha - \eta)\, dx\right] = N_{cr} \qquad x_{cr} \le d \qquad N_{cr} = 10^6 \cdots 10^8 \tag{117}$$

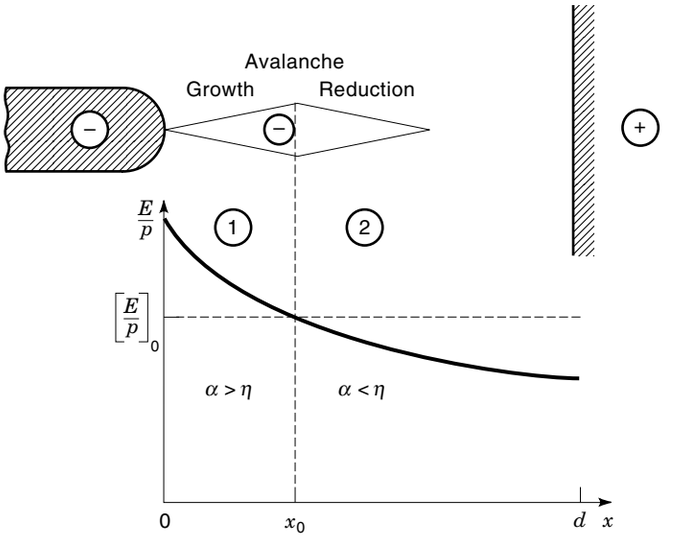

Figure 18. Avalanches in nonhomogeneous fields; area 1: avalanche growth, area 2: avalanche decrease.

For a nonhomogeneous field:

$$\int_0^{x_{cr}} (\alpha - \eta)\, dx = \ln N_{cr} = K_{St} \qquad x_{cr} \le d \qquad K_{St} = 13.8 \text{ to } 18.4 \tag{118}$$

$$\exp[(\alpha - \eta)x_{cr}] = N_{cr} \qquad x_{cr} \le d \qquad N_{cr} = 10^6 \text{ to } 10^8 \tag{119}$$

For a homogeneous field:

$$(\alpha - \eta)x_{cr} = \ln N_{cr} = K_{St} \qquad x_{cr} \le d \qquad K_{St} = 13.8 \text{ to } 18.4 \tag{120}$$

If less than N_{cr} electrons in the avalanche head are obtained at the anode, no breakdown occurs and the electrons are absorbed by the anode.

Originally this breakdown criterion had been verified experimentally and formulated by Raether only for homogeneous field distribution and for nonattaching gases. Later on it could be shown, that it may also be used in nonhomogeneous fields, as long as streamer breakdown is relevant, and also for attaching gases.

In the case of nonhomogeneous field distribution, as shown in Fig. 18, the calculation according to Eq. (117) has to be performed over the distance x_0 starting at the electrode to that point where the reduced field has dropped to the reduced limiting field $(E/p)_0$, as shown in Figs. 10 or 11. At this point if the critical number of electrons is not obtained, no breakdown occurs because no further increase in the number of electrons is possible. In the case of negative polarity of a curved electrode, which is shown in Fig. 18, a decrease of the avalanche occurs behind x_0. For positive polarity of a curved electrode, the maximum number of electrons is reached at the anode and those are absorbed in that case.

Breakdown Criterion According to the Generation Mechanism. Originally it was assumed that breakdown could occur only if several successive avalanches developed. However, the so-called generation mechanism or Townsend mechanism

(22), could not be maintained at least as a general case, because breakdown had also been observed for pulses of rather short duration.

For the generation mechanism the model of avalanche growth is identical to that of the streamer mechanism. If an avalanche is developing in a homogeneous field from a single electron at the cathode ($x = 0$), the number of electrons N_e in the avalanche head at location x (Fig. 17) is given by

$$N_e = \exp\left[\int_0^x (\alpha - \eta)\, dx\right] = \exp[(\alpha - \eta)\, x] \tag{121}$$

However, in addition, the number of positive ions N_I^+ in the avalanche tail are taken into account by

$$\begin{aligned} N_I^+ &= \int_0^x \alpha N_e\, dx = \int_0^x \alpha \exp[(\alpha - \eta)x]\, dx \\ &= \frac{\alpha}{\alpha - \eta}\{\exp[(\alpha - \eta)x] - 1\} \end{aligned} \tag{122}$$

The positive ions move back to the cathode, and according to the γ-process (see Secondary Electron Emission) N_{e0l} new initial electrons are released from the cathode

$$N_{e0l} = \gamma_I N_I^+ \tag{123}$$

with Townsend's second ionization coefficient γ_I.

Photons, emitted from the avalanche, also release electrons from the cathode. It is assumed that the number of emitted photons N_{ph}

$$N_{ph} = \epsilon N_I^+ \tag{124}$$

is proportional to the number N_I^+ of positive ions. Because of photon absorption in the gas only the fraction δN_{ph} of the emitted photons reaches the cathode and according to the section on Photoemission the number of new initial electrons N_{e0ph} is given by

$$N_{e0ph} = \eta_{ph} \delta \epsilon N_I^+ \tag{125}$$

The total number of electrons released from the cathode is determined by the feedback coefficient γ:

$$N_{e0} = \gamma_I N_I^+ + \eta_{ph} \delta \epsilon N_I^+ = \gamma N_I^+ \tag{126}$$

If the first avalanche has crossed the whole gap width d, according to Eq. (122) the number of initial electrons for the second avalanche is given by

$$N_{e0} = \gamma \frac{\alpha}{\alpha - \eta}\{\exp[(\alpha - \eta)d] - 1\} \tag{127}$$

On condition that

$$N_{e0} \geq 1 \tag{128}$$

the successive avalanche is larger than the first, which developed from a single initial electron. The following avalanches also grow steadily until breakdown occurs. The discharge current for the generation mechanism is shown in Fig. 19 for different numbers of initial electrons N_{e0} and different overvoltages ΔV related to the static breakdown voltage V_B. It is evident that rather long periods are required for discharge formation. According to Eqs. (127) and (128) the breakdown criterion for the generation mechanism is given by

$$\exp[(\alpha - \eta)\, d] \geq \frac{\alpha - \eta}{\alpha \gamma} + 1 \tag{129}$$

The corresponding breakdown criterion for the streamer mechanism from Eq. (119) is given by

$$\exp[(\alpha - \eta)\, d] \geq N_{cr} \tag{130}$$

Breakdown is possible according to both mechanisms if the limiting field E_0 is exceeded. However, the practical significance of the generation mechanism is limited. For instance, in SF_6 for fields which are slightly higher than $(E/p)_0$ the condition $\alpha \geq \eta$ is met. Under this condition, the decisive term in Eq. (129) is reduced to the feedback coefficient γ:

$$\frac{\alpha - \eta}{\alpha \gamma} \approx \frac{1}{\gamma} \tag{131}$$

The feedback coefficient, however, is greatly reduced by the gas pressure. In SF_6, the feedback coefficient due to the absorption of the short wavelength radiation is especially small, which can be seen from Fig. 20 (23). By comparing Eq. (129) and (130) and taking into account that for the streamer mechanism electron numbers N_{cr} of 10^6 may already be sufficient for breakdown inception, it is more and more unlikely that the generation mechanism can occur if the feedback coefficient is less than 10^{-6}.

Generally it is assumed that the generation mechanism can occur only for $pd < 1$ bar · cm. In any case a precondition for the occurrence of the generation mechanism is steady-state voltage stress.

BREAKDOWN CHARACTERISTICS

Paschen Characteristic (Similarity Law)

Paschen has shown by experiments that for homogeneous gaps with the gap width d and the gas pressure p the breakdown voltage V_B is a function of pd:

$$V_B = f(pd) \tag{132}$$

The Paschen curves agree with both the streamer mechanism and the generation mechanism. According to Eq. (120) the breakdown criterion for the streamer mechanism is given by

$$(\alpha - \eta)\, d \geq K_{St} \tag{133}$$

The corresponding criterion for the generation mechanism with Eq. (129) is given by

$$(\alpha - \eta)\, d \geq \ln\left[\frac{\alpha - \eta}{\alpha \gamma} + 1\right] \approx K_g \tag{134}$$

Because of the logarithmic dependency, variations of $[(\alpha - \eta)/(\alpha\gamma) + 1]$ do not have a big influence. Therefore this function

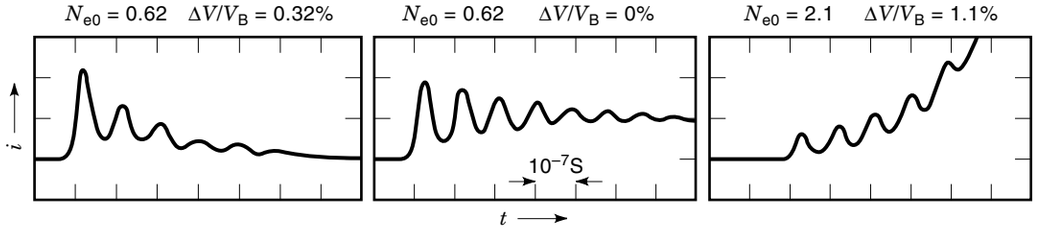

Figure 19. Discharge current for the Townsend mechanism; V_B—static breakdown voltage, ΔV—overvoltage, N_2/CH_4 gas mixture 1:60, p = 0.36 bar, homogeneous field, d = 1.46 cm (12).

can be approximated by the constant K_g for the generation mechanism. For both mechanisms, the following condition must be fulfilled for breakdown:

$$(\alpha - \eta)d \geq K$$

or

$$\frac{\alpha - \eta}{p} \geq \frac{K}{pd} \tag{135}$$

For each gas the reduced effective ionization coefficient $(\alpha - \eta)/p$ is a typical function of the reduced field [Eq. (109) or (110)]:

$$\frac{\alpha - \eta}{p} = f_1(E/p) = f_1\left(\frac{V}{pd}\right) \tag{136}$$

At the breakdown voltage V_B the breakdown criterion according to Eq. (135) must be fulfilled:

$$\frac{K}{pd} = f_1\left(\frac{V_B}{pd}\right) \tag{137}$$

Thereby the Paschen characteristic based on Eq. (132) is confirmed.

For nonattaching gases ($\eta = 0$), a simple formula for the breakdown voltage is obtained from Eq. (73) and Eq. (135) for $E = E_B = V_B/d$:

$$V_B = \frac{C_2 pd}{\ln\left(\frac{C_1 pd}{K}\right)} \tag{138}$$

where $K = K_{St}$ for the streamer mechanism and $K = K_g$ for the generation mechanism.

The Paschen curves have a typical minimum V_{Bmin} at $(pd)_{min}$. In Table 9 the minimum breakdown voltages (1), which depend on the electrode material, are shown.

In Figs. 21–23 some Paschen characteristics for technically relevant gases (24) are shown.

Similar to the Paschen characteristics of the breakdown voltage, the characteristics of the reduced breakdown field E_B/p can be defined. According to Eq. (137) the relevant function is

$$\frac{E_B}{p} = f_2(pd) \tag{139}$$

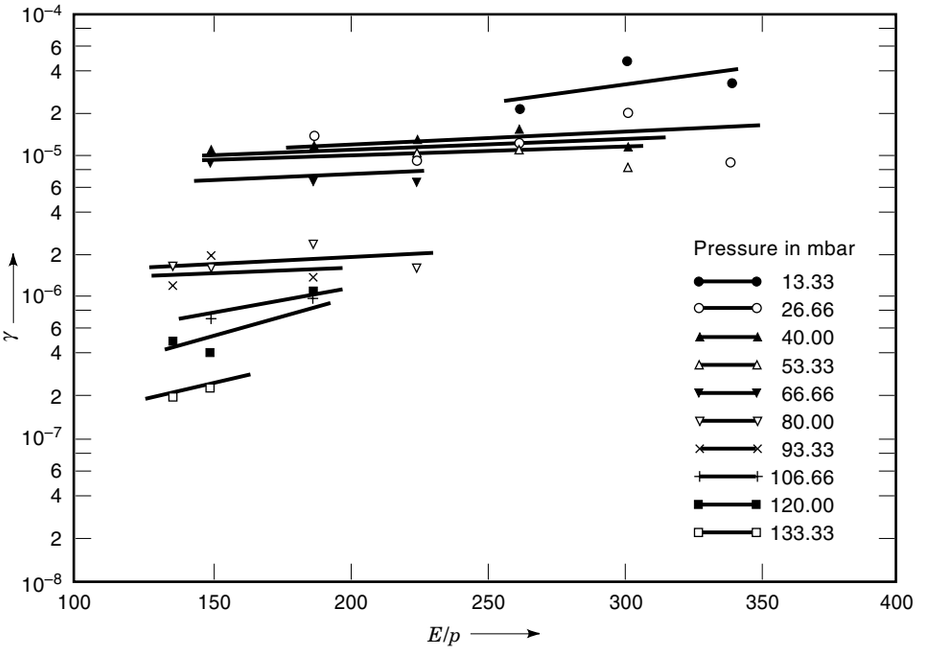

Figure 20. Feedback coefficient γ in SF_6 for rather low gas pressure (23).

Table 9. Minimum Breakdown Voltages of Some Gases[a]

Gas	$(pd)_{min}$, 10^{-3} bar · cm	V_{Bmin}, V
Air	0.73	352
SF_6	0.35	507
N_2	0.86	240
H_2	1.40	230
O_2	0.93	450
CO_2	0.68	420
He	5.32	155
Ne	5.32	245

[a] Ref. 1.

The typical shape of such curves is shown in Fig. 24. For large values of pd all curves approach the reduced limiting field $(E/p)_0$. However, there are big differences in the way this is achieved. The curve for plane–plane electrodes in air in Fig. 24 has a very steady slope and even for the greatest value of pd, the reduced limiting field $(E/p)_0$ = 24.4 kV/(cm · bar) is not reached because of the rather slow increase of the effective ionization coefficient in air after the reduced limiting field is exceeded [Eq. (110)].

The corresponding curve in Fig. 24 for plane–plane electrodes in SF_6 shows a quick decrease of the reduced breakdown field with increasing pd and for pd = 1 cm · bar the reduced limiting field $(E/p)_0$ = 87.7 kV/(cm · bar) is already nearly obtained. The reason for this characteristic is the very steep increase of the effective ionization coefficient in SF_6 after the reduced limiting field is exceeded [Eq. (109)].

For homogeneous fields in air the dependency of the reduced breakdown field on gas pressure and gap width has to be taken into account within the whole range of pd which is relevant for practical applications. In SF_6 and especially for homogeneous fields in many cases, the reduced breakdown field E_b/p may be approximated by the reduced limiting field $(E/p)_0$.

For breakdown in air a simple criterion had been developed by Schumann (11). This is obtained from the reduced effective ionization coefficient in air, as described by Eq. (110), and the breakdown condition according to Eq. (135). For homogeneous fields and a pressure of 1 bar, the following formula for breakdown voltage is obtained:

$$V_B = V_0 + \sqrt{\frac{C}{d}}$$

where

$$V_0 = 24.4\,\text{kV}$$

and

$$C = 45\,\frac{\text{kV}^2}{\text{cm}} \tag{140}$$

As a first approximation in SF_6 the breakdown field E_B is equal to (or greater) than the limiting field E_0. This is obtained from Eq. (109):

$$E_0 = p\left(\frac{E}{p}\right)_0$$

where

$$\left(\frac{E}{p}\right)_0 = 87.7\frac{\text{kV}}{\text{cm} \cdot \text{bar}} \tag{141}$$

Because of the steep increase of the effective ionization coefficient in SF_6, which is described by Eq. (109), the critical number of electrons is obtained in a very short distance (Fig. 16). Therefore in SF_6 the distribution of the field close to the surface of the more highly stressed electrode is decisive for the breakdown development. As an approximation, the field

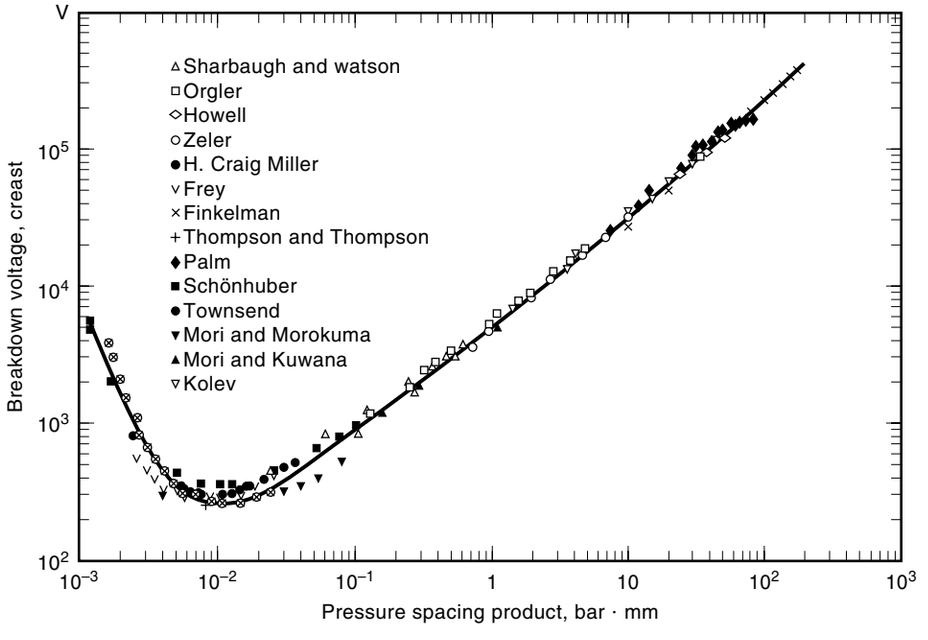

Figure 21. Paschen curve for N_2; temperature 25°C (24).

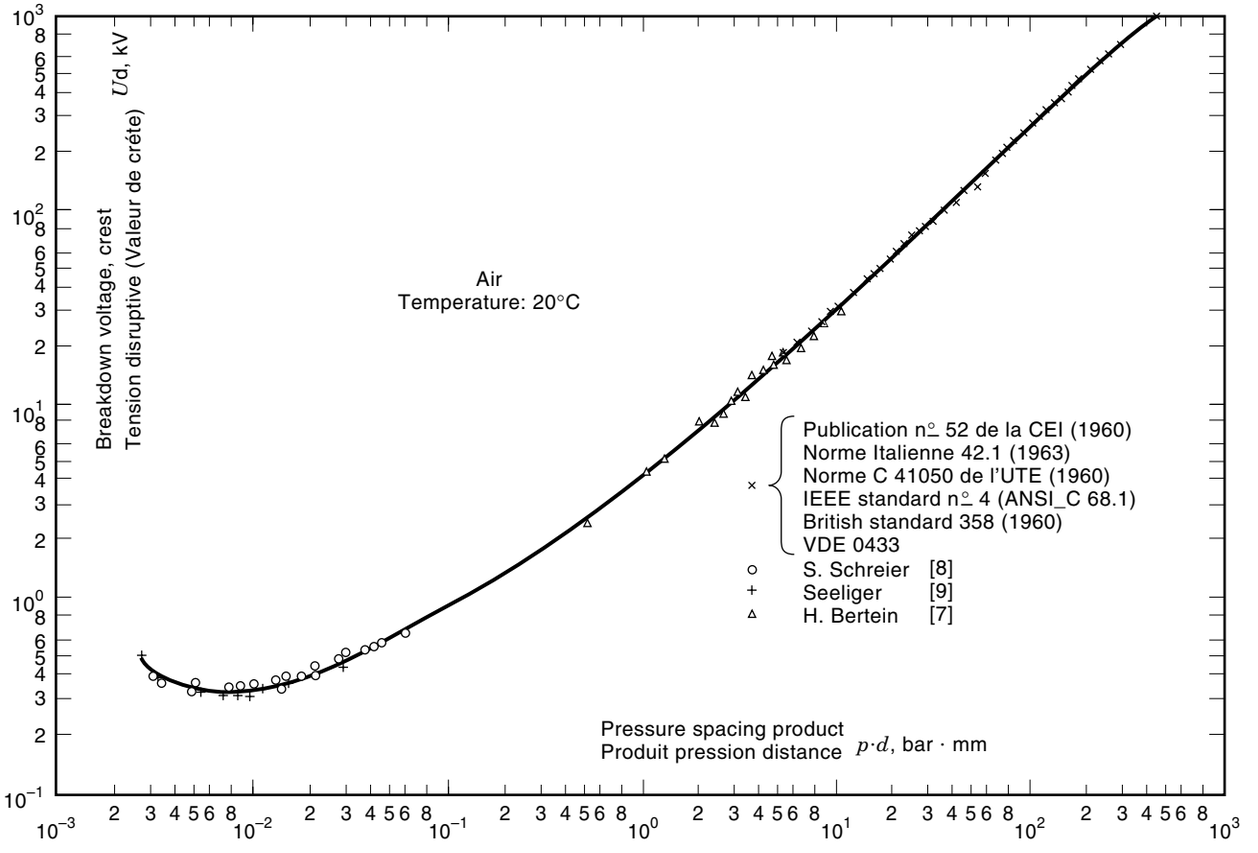

Figure 22. Paschen curve for air; temperature 20°C (24).

at the electrode surface can be introduced into the breakdown criterion according to Eq. (118). The effective ionization coefficient is taken from Eq. (109):

$$\int_0^{x_{cr}} \left[E - p \left(\frac{E}{p} \right)_0 \right] dx = \frac{K_{St}}{k} \qquad x_{cr} \le d \qquad \frac{K_{St}}{k} \approx 0.7\,\text{kV} \tag{142}$$

This equation means that the area of the field exceeding the limiting field E_0 [Eq. (141)] and the path x in the gap may not exceed the limiting value of approximately 0.7 kV. In principle this condition has already been shown in Fig. 18. Therefore the maximum permissible field is higher than the limiting field E_0. The difference is increased with decreased homogeneity of the field distribution. For the homogeneous field the breakdown voltage is based on Eq. (142):

$$V_B = 87.7 \frac{\text{kV}}{\text{cm} \cdot \text{bar}}\, pd + 0.7\,\text{kV} \tag{143}$$

The Paschen characteristic (similarity law) may be easily explained by a simple physical model, which is based on the similarity of two insulating arrangements. Arrangement 2 is obtained from arrangement 1 by magnification with the scale factor m. Accordingly the mean free path in arrangement 2 is increased by m, which is achieved by a decrease in the gas pressure corresponding to $1/m$. Therefore it ensures that

$$p_1 d_1 = p_2 d_2 \tag{144}$$

If the same voltage is applied, the field $E_2 = E_1/m$ is lower than in arrangement 1, but because the mean free path is increased according to $\lambda_{m2} = m\lambda_{m1}$, the energy of the charged particles $W = E\lambda$ is the same. Because also the mean number of collisions d/λ_m is also identical, exactly the same conditions for the discharge development are given. This results in identical breakdown voltages. Therefore the breakdown voltage is identified by the product pd as stated by the Paschen characteristic.

The Paschen characteristic may also be applied to electrode arrangements with approximately homogeneous field distribution. The only requirement is that no space charges are injected, which would result in additional distortion of the field distribution.

Breakdown of Gas Mixtures

Gas mixtures are of increasing interest. Mixtures are a very effective technique for obtaining optimized insulating characteristics by combining the advantageous features of two or even more components. A very popular example is the admixture of N_2 to SF_6. The insulating properties of SF_6 are reduced only slightly, but the liquefying temperature of the mixture is reduced significantly (7).

The following are characteristics of mixtures of two components, but in principle they are also valid for mixtures of more than two components. The molecular density n of a mixture is obtained from the molecular densities n_1 and n_2 of compo-

nents 1 and 2:

$$n = n_1 + n_2 \tag{145}$$

From Eq. (15) the total pressure

$$p = p_1 + p_2 = nkT \tag{146}$$

results from the partial pressures p_1 and p_2 of the components:

$$p_1 = n_1 kT$$

and

$$p_2 = n_2 kT \tag{147}$$

Because the liquefying temperature of a component corresponds to its partial pressure, the liquefying temperature of the mixture can be reduced.

It is evident that atmospheric air is also a gas mixture. However because this mixture, whose main components are O_2, N_2, and CO_2, always in the same ratio, it is commonly regarded as a unique gas.

During the analysis of the avalanche development in a gas mixture, the collisions of electrons with gas molecules have to be evaluated separately for each component. Therefore the different cross sections, ionization energies, and attachment energies have to be taken into account. For a mixture of molecules with collision cross sections a_{s1} and a_{s2}, the probability for a collision of an electron with a molecule of component 1 on the path ds is described by Fig. 3 and Eq. (18):

$$dw_1 = n_{B1} a_{s1}\, ds \tag{148}$$

and the number of collisions per unit length is given by

$$\frac{dw_1}{ds} = \frac{1}{\lambda_{m1}} = n_{B1} a_{s1} \tag{149}$$

According to the section on Collision Ionization, it is assumed that ionization occurs, if the transferred energy is equal to or greater than the ionization energy of molecule 1. The electrons receive this energy on the free path λ which is determined by collisions with the molecules of all components of the gas mixture. According to Fig. 3 and Eq. (18), the probability of a collision of an electron with molecules of both components on the path ds is given by

$$dw = n_{B1} a_{s1}\, ds + n_{B2} a_{s2}\, ds \tag{150}$$

The mean free path [Eq. (20)] is given by

$$\lambda_m = \frac{1}{n_{B1} a_{s1} + n_{B2} a_{s2}} \tag{151}$$

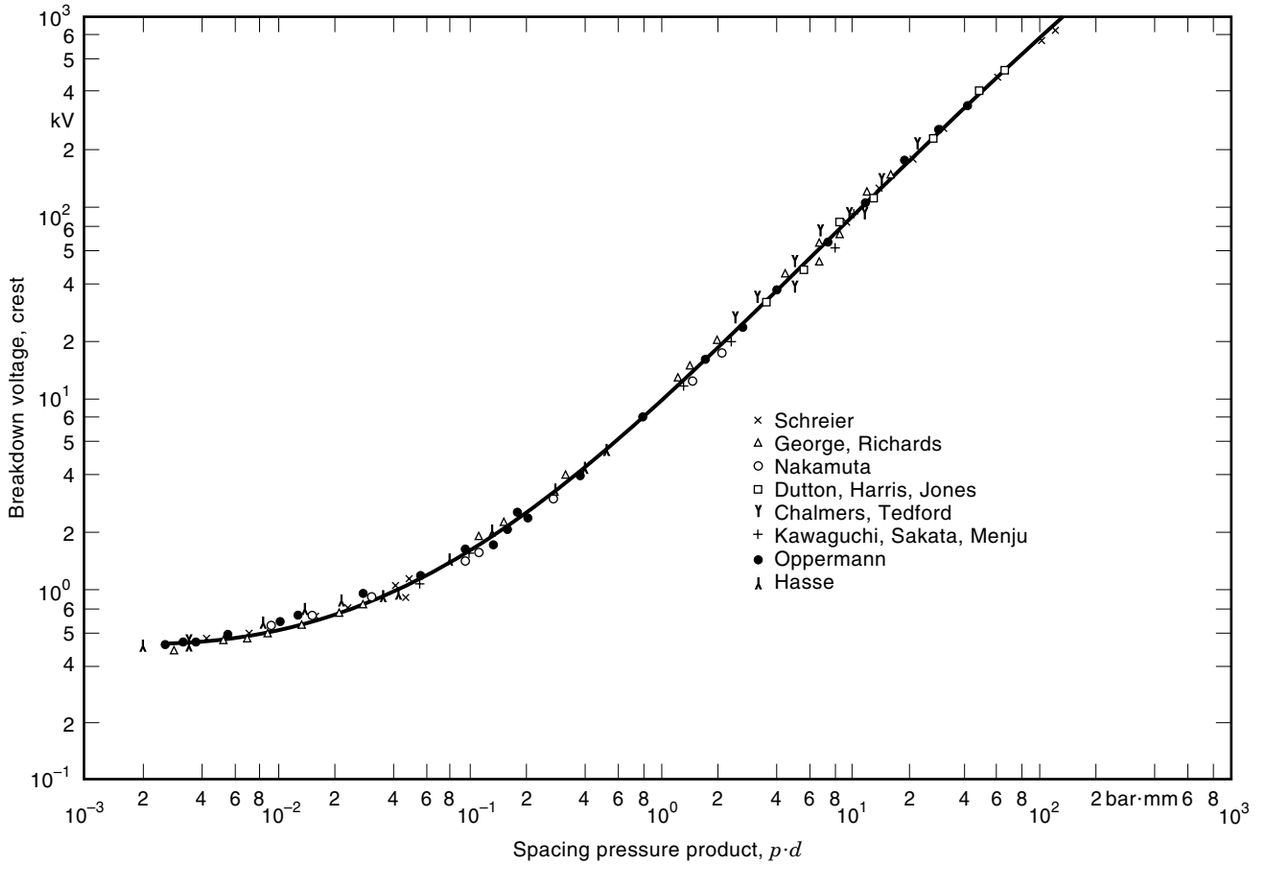

Figure 23. Paschen curve for SF_6; temperature 25°C (24).

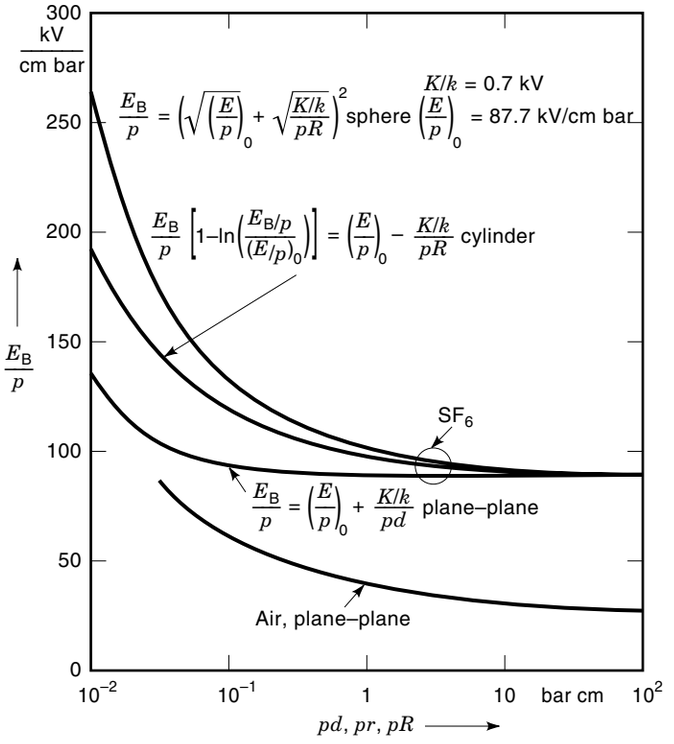

Figure 24. Reduced breakdown field of plane–plane electrodes with gap width d, coaxial cylinder electrodes with inner radius r, and coaxial sphere electrodes with radius R.

The ionization energy of molecule 1 is obtained, if the free path before a collision is in accord with Eq. (70):

$$\lambda_{I1} = \frac{\delta W_{I1}}{eE} \tag{152}$$

From Eq. (29) the collision probability is given by

$$P_1 = \exp\left(-\frac{\lambda_{I1}}{\lambda_m}\right) \tag{153}$$

The ionization coefficient for molecule 1 relates to the collision probability and the number of collisions with molecule 1 [Eq. (149)]:

$$\alpha_1 = \frac{P_1}{\lambda_{m1}} = n_{B1} a_{s1} \exp\left(-\frac{\lambda_{I1}}{\lambda_m}\right) \tag{154}$$

From Eqs. (152) and (154) an expression similar to Eq. (73) for a unique gas can be written for the ionization coefficient of component 1 in the gas mixture:

$$\frac{\alpha_1}{p_1} = C_{11} \exp\left[-\frac{C_{21}}{E/p}\left(\frac{p_1}{p} + \frac{p_2}{p}\frac{a_{s2}}{a_{s1}}\right)\right]$$

where

$$C_{11} = \frac{a_{s1}}{kT}$$

and

$$C_{21} = \frac{a_{s1}\delta W_{I1}}{ekT} \tag{155}$$

The simple model for the attachment [Eq. (97)] is also used accordingly:

$$\frac{\eta_1}{p_1} = C_{41}\left\{1 - \exp\left[-\frac{C_{31}}{E/p}\left(\frac{p_1}{p} + \frac{p_2}{p}\frac{a_{s2}}{a_{s1}}\right)\right]\right\} \tag{156}$$

The same calculations have to be made for component 2. The results can be obtained from Eqs. (155) and (156) if the numbering is changed accordingly.

The avalanche growth in the gas mixture can be calculated from Eq. (105) with the relevant effective ionization coefficients:

$$dN_e = (\alpha_1 - \eta_1)N_e\,dx + (\alpha_2 - \eta_2)N_e\,dx \tag{157}$$

The breakdown characteristics are obtained from the breakdown criteria for the streamer mechanism [Eqs. (117)–(120)] or for the generation mechanism [Eq. (129)].

In some cases a simplified model may be used, especially if high accuracy is not needed. In that case similar collision cross sections of the components $a_{s1} \approx a_{s2}$ are assumed. With Eq. (146) this results in

$$\frac{\alpha_1}{p_1} = C_{11} \exp\left(-\frac{C_{21}}{E/p}\right) \tag{158}$$

$$\frac{\eta_1}{p_1} = C_{41}\left[1 - \exp\left(-\frac{C_{31}}{E/p}\right)\right] \tag{159}$$

In this very simple model the ionization and attachment coefficients of unique gases can be used directly together with the relevant partial pressures p_1 and p_2. The reduced field, however, is obtained according to the total pressure. The result of this approximation (25) is shown in Fig. 25 for a SF_6–N_2 mixture. The accuracy is greatly improved if the different collision cross sections and further interactions of the particles are taken into account (26,27). As already stated, Eq. (97) and therefore also Eqs. (156) and (159) may not be used for some attaching gases like O_2 (and air).

An important conclusion from Fig. 25 is that small admixtures to SF_6 do not influence the insulating properties significantly. Even with 40% N_2 approximately 90% of the breakdown strength of pure SF_6 is maintained.

Surface Effects

Until now only the influence of the macroscopic field distribution has been taken into account in evaluating breakdown characteristics. This is only justified if the surface roughness of the electrodes (and other solids materials in the discharge volume) can be neglected. If this condition is not met, the measured breakdown voltages may be greatly affected (28,29). Thereby deviations from the Paschen characteristics, which can be observed in air at very high gas pressure and in SF_6 even at a moderate gas pressure of approximately 2 bar, can be explained (30).

The surface roughness of high quality electrodes will be less than some μm. It can be further improved by special sur-

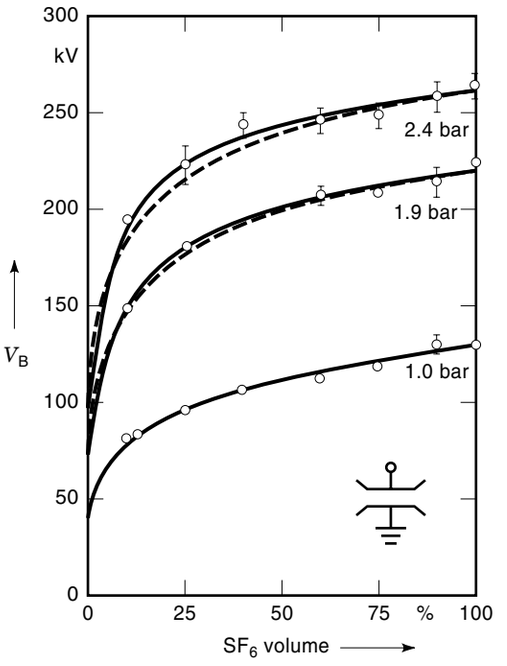

Figure 25. Breakdown voltage (ac) V_B of SF_6–N_2 mixtures depending on the relative SF_6 volume for constant gap width d = 15 mm and different total pressures (25); —— measurement, --- calculation.

face treatment. All kinds of discharges influence the microstructure of the electrode surface. Discharges with rather low energy can have a favorable effect (conditioning) because usually a smoothing of the microstructure occurs. Discharges with high energy cause considerable melting of the electrode surface, which usually results in degradation of the microstructure.

The surface roughness of the electrodes and its basic influence on the field distribution is shown in Fig. 26. Therefore in the vicinity of the electrode surface the microfield exceeds the macrofield, which is obtained without significantly considering the surface roughness.

Such surface phenomena can be taken into account for single protrusions according to Fig. 27. As can be seen from Fig. 27(a) only the reduced microfield in the vicinity of the electrode surface exceeds the reduced limiting field $(E/p)_0$. In the remaining part of the gap the field is lower than the reduced limiting field. Therefore without the field enhancement by surface roughness, no breakdown could occur.

In Fig. 27(b) the effective ionization coefficient $\alpha - \eta$ is plotted for three examples. Only for the microfield in the region $0 < x \leq x_0$ with $E/p > (E/p)_0$ is a positive effective ionization coefficient provided, which allows avalanche growth. The number of electrons N_e generated is shown in Fig. 27(c).

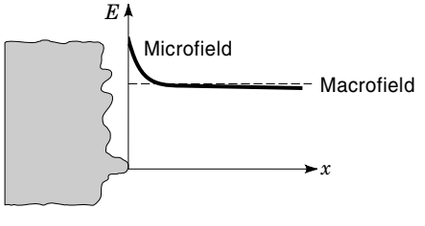

Figure 26. Field enhancement by surface roughness of the electrode; --- macrofield, –– microfield.

For the streamer mechanism the breakdown criterion is in accord with Eq. (118):

$$\int_0^{x_0} (\alpha - \eta)\, dx = K_{St} \tag{160}$$

Then either the area above the zero line in Fig. 27(b) must be equal to K_{St} or the electron number in Fig. 27(c) at x_0 must be equal to or greater than N_{cr}. The big differences among the three examples are caused by the fact that the effective ionization coefficient [Eq. (110)] in air has a rather slow increase with the field after the reduced limiting field is exceeded. In SF_6 this initial increase of the effective ionization coefficient [Eq. (109)] is much higher, which results in the different curves in Fig. 27(b). If in addition the gas pressure is increased from p_1 to p_2, which results in a proportional increase in the effective ionization coefficient, the breakdown criterion in SF_6 is fulfilled. This effect can also be observed in air and in other gases, but as shown in Fig. 27, much higher gas pressures would be required.

It is not practical to simulate any individual shape of the electrode surface. The most important factor, however, is the height h of the protrusions on the rough electrode surface, which are shown in Fig. 26. The size of the range $0 < x \leq x_0$ in Fig. 27(a) is increased with h, which also increases electron multiplication according to Eq. (160). Additionally, as shown before, the gas pressure directly increases electron multiplication. Therefore the product ph is decisive for the effect of surface roughness on the breakdown characteristics. An example of this effect for single protrusions is shown in Fig. 28 for SF_6 (31).

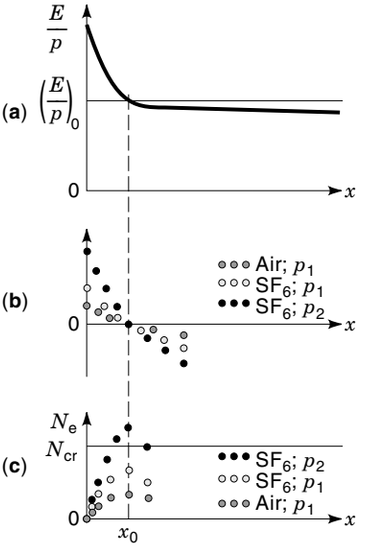

Figure 27. (a) Reduced microfield E/p; (b) effective ionization coefficient $\alpha - \epsilon$; and (c) electron number N_e near the rough electrode surface in air and SF_6 at gas pressure p_1 and in SF_6 at increased gas pressure p_2.

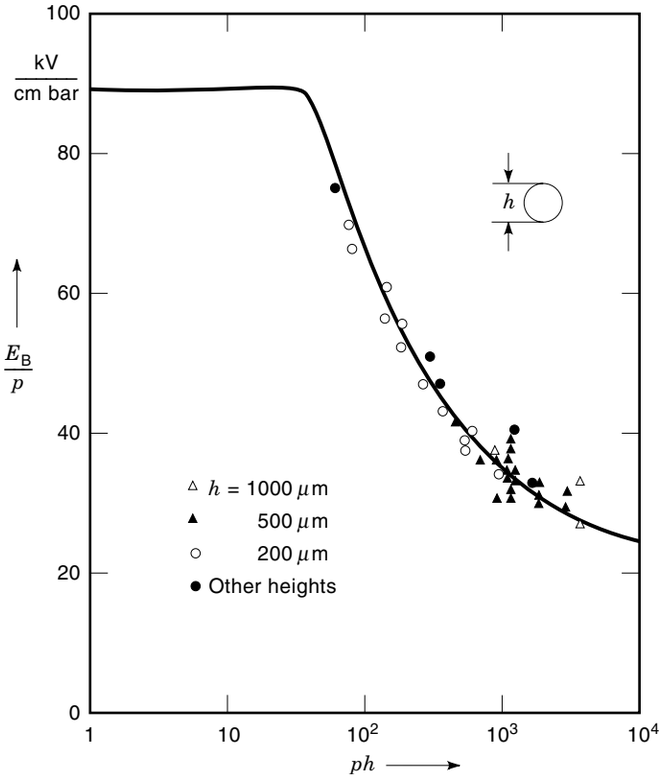

Figure 28. Breakdown field strength in a homogeneous field with field distortion by spherical protrusions with height h. The straight line is based on a calculation; the markers represent measurements (31).

BREAKDOWN IN NONHOMOGENEOUS FIELDS

In nonhomogeneous field breakdown also occurs according to the streamer mechanism (see previous sections). However, depending on the degree of homogeneity, after the streamer criterion is fulfilled, stable corona discharges are maintained in the high-field area (Fig. 29).

The degree of homogeneity η is defined as the ratio of the mean field V/d and the maximum field in the gap:

$$\eta = \frac{E_{\text{mean}}}{E_{\max}} = \frac{V}{dE_{\max}} \tag{161}$$

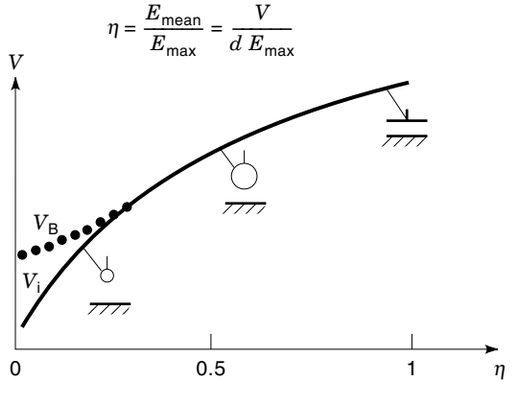

Figure 29. Breakdown voltage V_B and corona inception voltage V_i versus η for constant gap width d.

In general for nonhomogeneous field distribution, a distinction must be made between the corona inception voltage V_i and the breakdown voltage V_B. In cases with rather low values of η, a further voltage increase is required until a transition from the corona to a complete discharge formation occurs. However, usually this occurs in accordance with the streamer mechanism.

In very large gaps in the range of meters and impulse voltages of rather long rise times, a different phenomenon occurs in addition to the streamer. This leader mechanism, which is based on an initial streamer, is characterized by high current density in the prebreakdown channel and thermoionization.

Space-Charge Formation (Polarity Effect)

Because of corona discharges, especially in the high-field region, space charges are injected, which distort the electrostatic field distribution. This phenomenon will be analyzed for a point-to-plane gap in air. Thereby a pronounced polarity effect occurs because of a different discharge development and the different mobility of electrons and ions.

Positive Point–Plane Electrode. The limiting field $p(E/p)_0$ at first is exceeded in the vicinity of the positive point. Starting with primary electrons, which are generated by cosmic or terrestrial radiation, electron avalanches develop, which grow toward the positive point. After the streamer criterion [Eqs. (117) or (118)] has been fulfilled, the photonemission from the avalanche head induces the formation of successive electron avalanches. This causes a stable corona near the point electrode, which can be observed as a local glow discharge.

The electron avalanches develop toward the positive-point electrode with an increasing field. Thereby the critical number of electrons can be obtained on a short path, which also results in a rather high density of the positive ions. Because of their high mobility, the electrons are quickly collected at the anode. A space charge of slow positive ions remains in the vicinity of the positive-point electrode. Therefore the field near the point electrode is reduced significantly [Fig. 30(a)]. However because of the positive space charge, the point electrode is virtually elongated, which reduces the gap width and increases the field in the remaining gap. Thus a rather low breakdown voltage is typical for the positive point–plane electrode.

Negative Point–Plane Electrode. Primary electrons are also provided by emission from a negative-point electrode. As the avalanche develops toward a decreasing field, a longer path is needed until the critical size is obtained. If the field is high enough to fulfill the streamer criterion, the photonemission from the avalanche head induces the formation of successive electron avalanches. This leads to a corona discharge near the point electrode. The electrons drift toward the low field regions and in electronegative gases like air negative ions are formed by electorn attachment.

Because of the negative space charge, the field in the vicinity of the point electrode is reduced and the corona discharge is not maintained. A reignition of the corona occurs after the negative ions have been collected at the anode. This results in a pulsed corona (Trichel pulses), as shown in Fig. 31 (32). By increasing the voltage, the drift velocity of the negative ions is increased, which also increases the repetition rate of

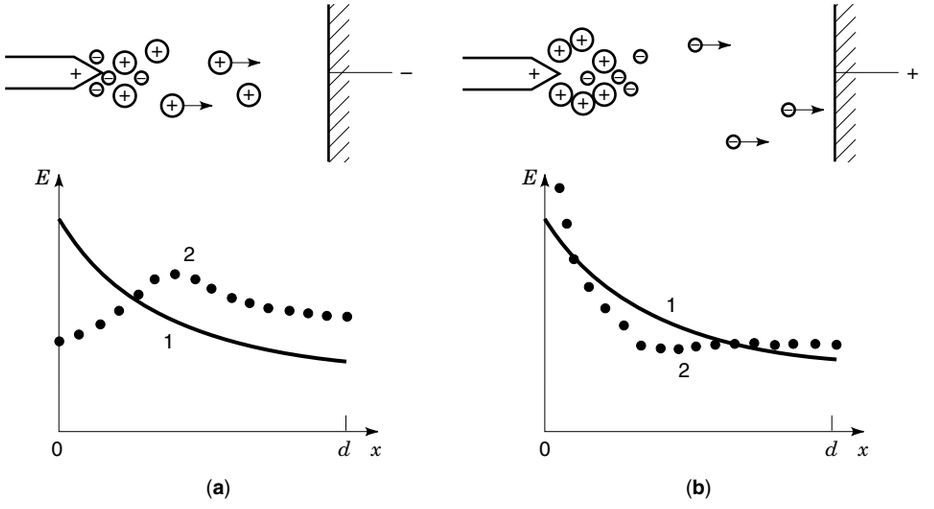

Figure 30. (a) Field distribution without (1) and with (2) space-charge-induced field distortion for positive point-plane electrode and (b) negative point-plane electrode.

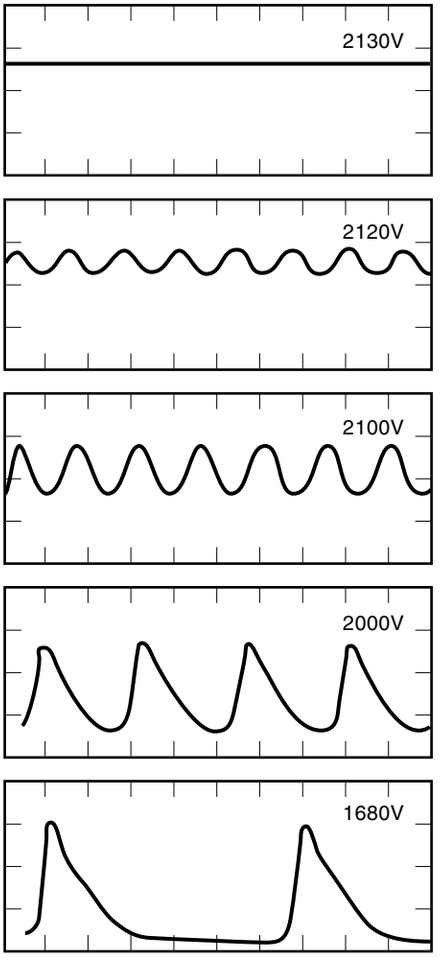

Figure 31. Transition of pulsed corona (Trichel pulses) to stable corona; gap distance $d = 2$ cm; N_2 with a tiny addition of O_2; $p = 0.8$ bar; timescale: 0.1 μs/division (32).

the corona pulses. When the loss of ions by drifting to the anode is equal to the generation rate, a stable corona is maintained. In nonattaching gases no negative ions are formed and no pulsed corona occurs.

Because critical avalanches develop, a positive space charge is left at some distance from the negative-point electrode, which results in a significant increase of the field near the point electrode [Fig. 30(b)]. In the vicinity of the anode the negative space charge results in some increase of the field. The outcome is a more homogeneous field distribution in the main part of the gap, which results in a rather high breakdown voltage.

$$V_{\mathrm{B(positive\ point)}} < V_{\mathrm{B(negative\ point)}} \tag{162}$$

For ac voltage stress, the positive half-wave is decisive and breakdown occur at its peak value $\hat{V}_{\mathrm{B}}$:

$$\hat{V}_{\mathrm{B}} = V_{\mathrm{B\ positive\ point}} \tag{163}$$

Streamer Discharge

Breakdown in a nonhomogeneous field is initiated by a streamer discharge, which in case of very low values of η (Fig. 29) develops from a stable corona discharge. There are no differences from the mechanism described in Evaluation of the Streamer Mechanism. However the strong gradient of the field causes some special effects. According to the polarity of the high-field electrode, a distinction has to be drawn between the positive and the negative streamer.

Positive Streamer Discharge. In the vicinity of the positive high-field electrode, which has a corresponding low electrode radius, the limiting field $p(E/p)_0$ is exceeded. A first electron avalanche develops toward the anode. If the electron avalanche reaches its critical size in front of the avalanche head and at the avalanche tail, as shown in Fig. 17, a significant field increase occurs. Photons are emitted from the avalanche head and in the region behind the avalanche tail, where because the field enhancement of the limiting field is exceeded, new avalanches are initiated. These avalanches move toward

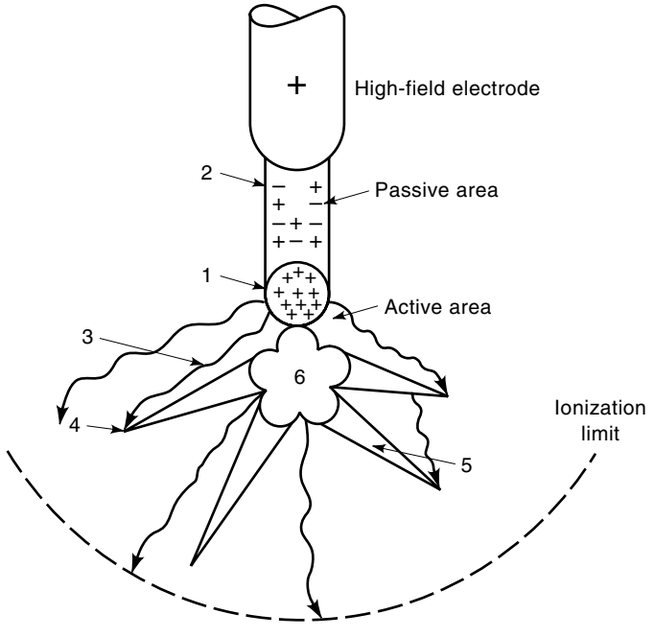

Figure 32. Development of the positive streamer discharge (33): 1—former streamer head; 2—streamer channel; 3—photon emission; 4—primary electron; 5—avalanche; 6—new streamer head.

the positive space charge of the initial avalanche and neutralize this positive space charge. Thereby a new center of positive space charges is formed, which moves toward the cathode. The heads of successive streamers will be located there.

This streamer development is shown in Fig. 32 (33). Around the head of the streamer with positive charge is (1) an area with active ionization. At the boundaries of this area the field is reduced below the limiting field $p(E/p)_0$. In this area (3) photoelectrons induce new electron avalanches (4, 5), which develop concentrically toward the streamer head. The large number of electrons entering the streamer head neutralizes the positive space charge at this location. However during their development a new center with positive space charge is formed (6), which has been moved toward the cathode.

Behind the streamer head a channel with low conductivity (2) remains. Because of the reduced field within this streamer channel, no further ionization occurs. The streamer can develop toward the cathode as long as the space-charge field at the streamer head combined with the basic electrostatic field are sufficient to generate new avalanches. The required minimum electrostatic field E_{gmin} in dry air is 4 kV/cm (34). Therefore the maximum range of the streamer increases with the homogeneity of the field. The mean streamer gradient has the same order of magnitude as E_{gmin}. In Ref. 35 a value of 4 to 5 kV/cm was found.

Negative Streamer Discharge. In the case of a negative high-field electrode primary electrons are also emitted from the cathode. An avalanche develops toward a decreasing field. However, because the field is enhanced by the negative charge of the avalanche head an area with active ionization is also available ($E > p(E/p)_0$). After the first avalanche reaches its critical size, new avalanches are induced within this area by photon emission. Therefore neutralization of the negative charge of the first avalanche head and the positive charge within the tail of the successive avalanches occurs. The charge within the head of the successive avalanches form a new negative streamer head.

Because the streamer head in this case is formed by electrons with high mobility according to Eq. (112), a larger radius is obtained compared with the radius of the head of the positive streamer. This results in a lower charge density and accordingly in a lower field enhancement. Therefore the minimum electrostatic field E_{gmin}, which is required for the streamer propagation, is much higher and amounts to between 13 to 18 kV/cm (36). The gradient of the negative streamer is also much higher than that of the positive streamer and amounts to between 7 to 10 kV/cm (35).

Leader Discharge

Leader discharge is typical for a very large gap width and switching-impulse voltage. Because much lower breakdown voltages occur for positive polarity of the high-field electrode, this case is relevant for dimensioning and has been investigated in detail (37–40).

The structure of the positive leader is shown in principle in Fig. 33. The leader can be separated into the leader channel (1), the leader head (2) and the leader corona (3). In the leader channel with diameter d_{L} a rather high current density exists. Therefore thermoionization occurs in the leader channel at high gas temperature T_{G}. Because of the high degree of ionization the leader gradient is rather low. The following data are typical for a leader channel about a meter long in air (38):

$$i_{\text{L}} \approx 0.6 \cdots 1\text{A} \quad E_{\text{L}} \approx 1.5\,\text{kV/cm} \quad d_{\text{L}} < 3\,\text{mm} \quad T_{\text{G}} \approx 5000^{\circ}\text{C} \tag{164}$$

The key factor for leader development is the supply of energy by the leader current i_{L} through the leader channel (1). Energy is required to maintain the high leader temperature

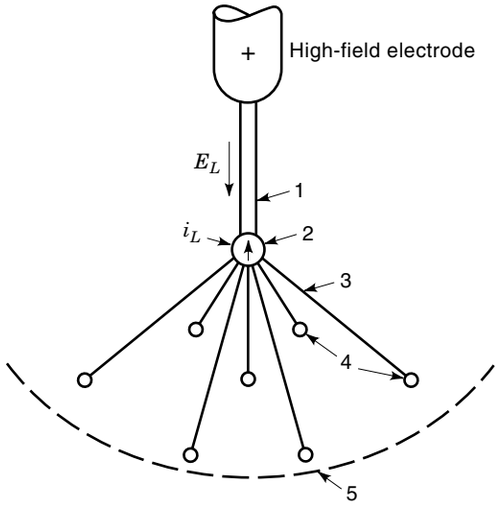

Figure 33. Leader development (33): 1—leader channel; 2—leader head; 3—leader corona; 4—streamer head of the corona; 5—limit of the ionization range.

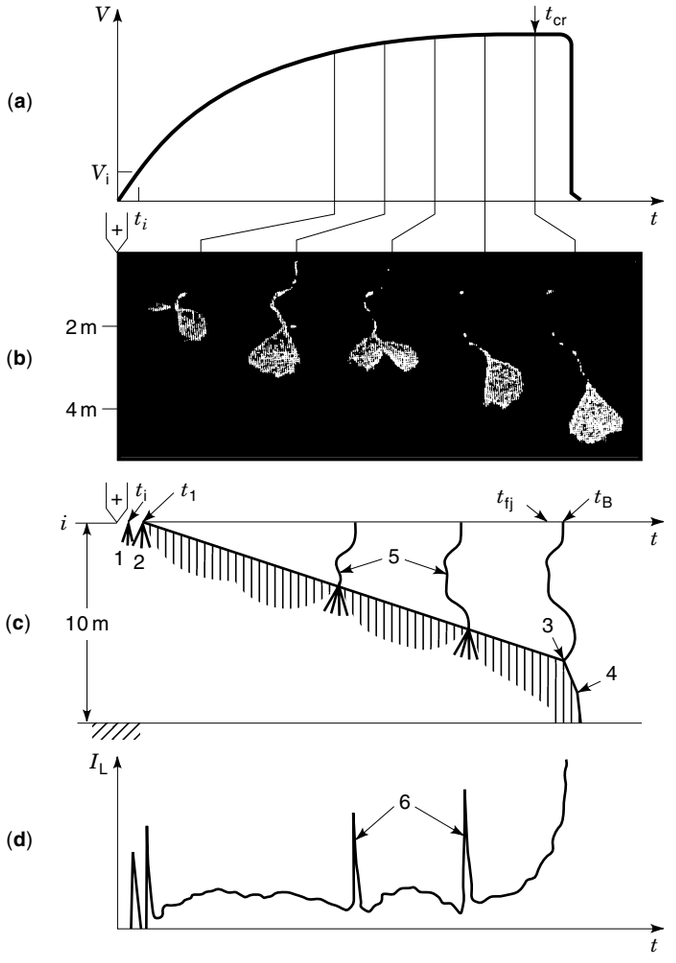

Figure 34. Discharge development in a 10 m rod-plane gap stressed with switching impulse voltage of critical shape 500/10000 μs and amplitude V_{cr} = 1760 kV (33); (a) voltage impulse, crest time t_{cr} = 500 μs; (b) framing photos of the discharge development (41); exposure time 10 μs; (c) schematic drawing of the temporal and spatial discharge development; (d) discharge current at the high field electrode (rod).

and thermoionization. Part of this energy is transferred from the leader head (2) to the leader corona (3). The leader corona is spread within an area starting from the leader tip to the limit of the ionization range (5), where the field is reduced below the limiting field $p(E/p)_0$. Within this area streamer-like discharges occur (4), which start successively from the leader head.

An experimental analysis of leader discharge is shown in Fig. 34 (41). Three different stages of development can be distinguished: the first corona (1), the leader development (2–3), and the breakdown development or final jump (4). After the corona inception voltage V_i is exceeded at time t_i, a corona discharge develops from the tip of the high-field electrode, which consists of single streamer-like discharges. Those streamers develop within the discharge volume as long as the required minimum basic field E_{gmin} of approximately 4 kV/cm is available. Because this range is less than the electrode distance, the gap cannot be bridged by a streamer.

Because the positive space charge in the streamer heads, the field in the vicinity of the high-field electrode is reduced, which results in extinction of the corona. After some increase of the applied impulse voltage the field, which is required for corona inception, can be obtained again. The successive corona, however, can proceed a certain distance toward the plane electrode. This process may be repeated several times proceeding with development of the corona discharge.

The second stage starts at t_1 with the inception of the leader discharge at the high-field electrode. Then the direction of the leader progression diverts significantly from the direction of the applied external field. During the investigations described here, which were performed with switching-impulse stress of critical shape (minimum breakdown voltage), the mean velocity of the leader and the leader current are assumed to be constant. Such optimum conditions for leader development are obtained, if the temporal increase of the applied voltage is equal to the increase of the mean voltage gradient of the leader, which is caused by the leader progression.

The short luminous phenomena of the leader development (5) together with a current impulse (6) indicate a noncontinuous progression of the leader corona. Such phenomena preferably occur together with a change of direction of the leader progression, where other areas of the discharge volume have to be crossed by the streamer corona. These steps in the development are comparable with the occurrence of the first corona (1).

At time t_{fj} the corona streamer in front of the leader head reaches the plane electrode (4). Now the last phase of the discharge development, called the final jump, occurs. In this phase a continuous high conductive plasma channel is formed, and at time t_B the voltage collapse occurs. This final phase is greatly influenced by the impedance of the test circuit.

The main reason for the low breakdown voltages obtained when the leader mechanism occurs, is the low gradient E_L within the leader channel. Detailed investigations (39) have shown that this gradient is reduced from an initial value of approximately 5 kV/cm to values from 1 to 1.5 kV/cm.

The leader development is closely linked with the rate of increase of the applied external voltage, and an optimum leader propagation is observed for a certain rate, which results in a typical minimum breakdown voltage. This minimum is achieved for a crest time t_{crit} of the switching-impulse voltage, illustrated in Fig. 35. At this minimum an optimal development of the leader occur because the potential at the leader head V_L and the progression of the leader development are nearly constant. As mentioned before, this requires that the temporal increase of the applied voltage is equal to the increase of the mean voltage gradient of the leader, which is caused by the leader progression.

For short crest times $t_{cr} < t_{crit}$ an initially increased leader gradient is obtained. However, because of the early decrease of the double exponential impulse voltage, the potential of the leader head is reduced before sufficient progression of the leader occurs. This results in an increased breakdown voltage.

For long crest times $t_{cr} > t_{crit}$ the increase of the voltage gradient during the progression of the leader cannot be compensated for by the increase of the applied impulse voltage. Therefore the potential at the leader head is reduced signifi-

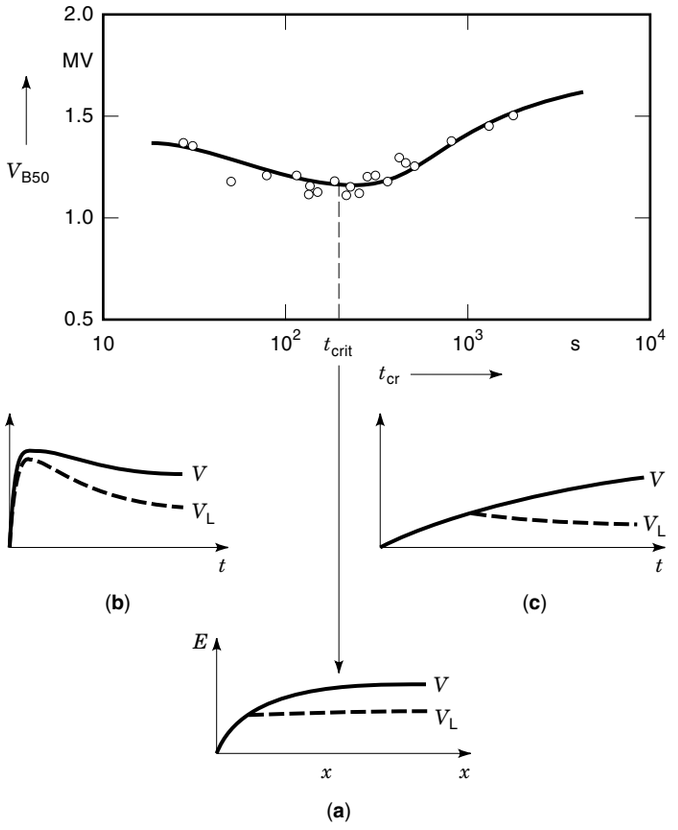

Figure 35. Influence of the crest time on the 50% breakdown voltage V_{B50} of a positive rod-plane gap, $d = 4$ m (35). V_L—potential at the leader head; (a) and (b) continuous leader; (c) noncontinuous leader.

cantly. Thereby the leader progression is impeded and may occur noncontinuously. This effect also results in an increased breakdown voltage.

A distinct minimum of the switching impulse resistance voltage occurs at $t_{cr} = t_{crit}$ (Fig. 35). This minimum depends on the gap width d. For decreasing gap width t_{crit} is reduced. The dependency of the 50% breakdown voltage V_{B50min} at t_{crit} of a positive rod-plane gap on the gap width d is given by an empirical formula (42,43):

$$V_{B\,min} = \frac{34}{1 + \dfrac{8\,\text{m}}{d}}\,\text{MV} \qquad \text{for} \quad 2\,\text{m} < d < 15\,\text{m} \quad (165)$$

$$t_{crit} = \left(35\frac{d}{\text{m}} + 50\right)\,\mu\text{s}$$

$$V_{B\,min} = \left(1.4 + 0.055\,\frac{d}{\text{m}}\right)\,\text{MV} \qquad \text{for} \quad d > 15\,\text{m} \quad (166)$$

$$t_{crit} = 50\,\frac{d}{\text{m}}\,\mu\text{s}$$

BREAKDOWN CHARACTERISTICS FOR TRANSIENT VOLTAGES

For impulse-voltage stress, the temporal development of the discharge has to be analyzed in detail. During discharge development, the statistical time lag t_S, the formative time lag t_F and the spark formation time t_B are observed. As shown in Fig. 36, the required limiting field E_0 must be available, which requires the voltage V_0. For the steep-fronted impulse V_0 is applied without delay. For the double exponential impulse the time t_0 is needed until V_0 is applied.

Primary electrons are needed to develop the first avalanche. The generation of primary electrons, for instance, by cosmic or terrestrial radiation is a statistical process. Therefore the statistical time lag t_S, which is needed until a sufficient number of primary electron is available in the critical discharge volume, may have a big scatter and strongly depends on the experimental conditions.

The formative time lag t_F is needed for the formation of a critical avalanche, the development of one or several streamers, and in special cases also a leader. Usually the scatter of this time lag is low.

The spark formation time t_B is required to increase the conductivity of the streamer channel until the voltage collapse across the gap occurs. This time lag is comparatively low without significant scatter.

Statistical Time Lag

Primary Electron Rate. To generate primary electrons, a distinction must be made between nonattaching and attaching (electronegative) gases. In the latter, the generated electrons are attached rather quickly and only a few primary electrons are available. Therefore a large statistical time lag with high spread occurs. Because atmospheric air has weak electronegative characteristics, similar effects occur. In nonattaching gases like N_2, lower statistical time lags are to be expected.

For electron multiplication, the effective ionization coefficient $\alpha - \eta$ depends strongly on the electric field. In attaching gases, the reduced field E/p must exceed the limiting reduced field $(E/p)_0$ until positive values of $\alpha - \eta$ are obtained and electron multiplication becomes possible (Figs. 10 and 11). Therefore for attaching gases only those primary electrons are relevant for electron multiplication which are within the so-called critical volume where the condition $E/p > (E/p)_0$ is fulfilled. For instance, in SF_6 within the critical volume the reduced field must exceed 87.7 kV/(cm · bar).

Ionization occurs within the gas volume by cosmic or terrestrial radiation (see Photoionization), and electrons together with positive ions are formed. Depending on the attachment coefficient of the gas, more or less electrons are attached to neutral gas molecules (see Electron Attachment), thereby negative ions are formed. Because the attachment coefficient is very high in SF_6 for low fields or without fields (Fig. 11), only a few free electrons are available in those conditions.

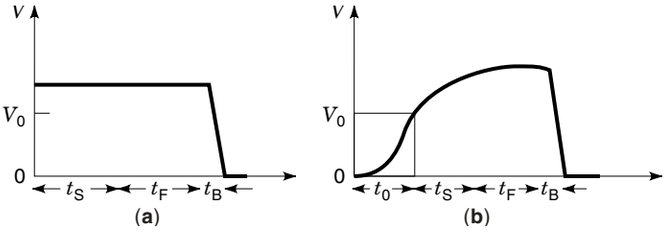

Figure 36. Time lags until breakdown in (a) a voltage step and (b) a double exponential impulse.

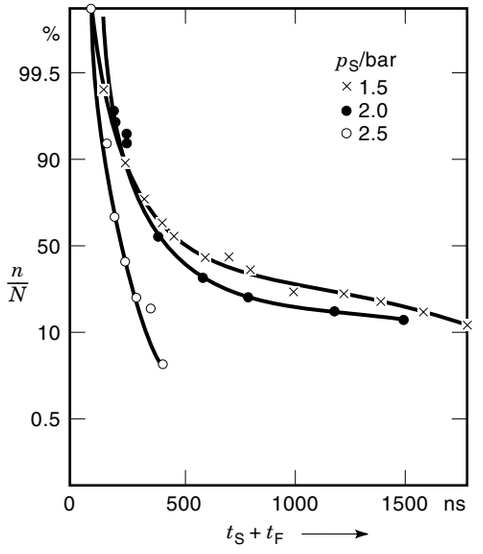

Figure 37. Reduction of the statistical time lags in SF_6 by pulsed UV ionization; n—number of events with a time lag ($t_S + t_F$) greater than indicated; N—total number of events being investigated; d = 4.2 mm; p = 1.5 bar; relative overvoltage $(V - V_B)/V_B$ = 7%; p_S—gas pressure of the gap used for pulsed UV illumination.

If no field or low fields are applied, the ionization rate of a gas is very low. In these conditions the recombination of electrons with positive ions is negligible because the density of positive ions is very low and the probability for such a recombination is proportional to the product of electron density n_e and ion density n_i^+. The probability for attachment of an electron to a neutral molecule is much higher because the density of the neutral molecules is high. If the detachment of electrons from negative ions is taken into account, the rate of the generation of primary electrons is given by

$$dn_e/dt = aSn_M - bn_M n_e + dn_i^- n_M \tag{167}$$

where the radiation coefficient is a, the radiation density S, the molecule density n_M, the attachment coefficient for thermal particle movement b, the electron density n_e, the detachment coefficient d, and the density of the negative ions is n_i^-. A stationary state with respect to the number of electrons is obtained for

$$dn_e/dt = 0 \tag{168}$$

Therefore the number of primary electrons per unit volume n_e, available for avalanche formation is given by

$$n_e = \frac{aS + dn_i^-}{b} \tag{169}$$

As can be seen from Eq. (169), the number of primary electrons is greatly influenced if the radiation density is increased, for instance, by UV illumination of the discharge volume or the electrode surface (see Photoemission). This phenomenon is demonstrated in Fig. 37 for a small SF_6 gap with approximately homogeneous field distribution (44,45). The amplitude of the applied dc voltage is only 7% more than the dc breakdown voltage. In these conditions very long statistical time lags have to be expected in SF_6. However, if the number of primary electrons is increased by the UV radiation of a pulsed gap, the statistical time lags are greatly reduced and may approach the limiting value of approximately 100 ns, which must be regarded as the formative time lag for that special condition. This is nearly obtained if the gas pressure of the pulsed gap is increased to p_S = 2.5 bar.

An optical investigation of the prebreakdown phenomena in SF_6 for approximately homogeneous fields (46) showed clearly that the primary electrons are generated by the UV illumination mainly at the electrode surface by photoemission (see Photoemission). But only those generated at the cathode surface are effective because those generated at the anode surface are immediately drawn back to the anode. This can be seen from the series of high speed photographs with an exposure time of 1 ns shown in Figs. 38 and 39. The breakdown voltage V_B, the exposure time referred to the beginning of the voltage collapse t_{exp}, and the relative luminous gain of the high speed framing system G_L are indicated for each frame.

In both cases the discharge starts at the cathode, which Fig. 38 (positive polarity of the high-field electrode) is the low field electrode. For this reason for positive polarity of the high-field electrode a higher overvoltage is required to obtain similar discharge development.

Such additional ionization by UV illumination is an effective measure for reducing the spread of measured results, which, especially in attaching gases, would otherwise require extensive statistical evaluation.

If no additional ionization is available, the number of primary electrons in attaching gases is increased by detachment (47) when the applied voltage is increased. The analysis of these phenomena is very complicated especially because in practical application double exponential voltage pulses are the main interest and the exact shape of this voltage would have to be taken into account for such an analysis.

Additionally, if higher fields are applied, primary electrons are released from the cathode surface by field emission (see Field Emission). This effect has to be taken into account if high surface roughness at the electrodes occurs and high gas pressure are used (see Surface Effects). In SF_6 with a technical quality electrode surface gas pressures of more than 3 bar are usually required (1). However, this effect is relevant only if the cathode is the high-field electrode because otherwise these electrons are not available within the critical volume.

Usually in these conditions experimental data for the effective rate of generating primary electrons $(dn/dt)_0$ are required. From such experiments (48) the following range for $(dn/dt)_0$ can be specified for impulse voltages of the shape 1.2/50 μs:

$$\left[\frac{dn}{dt}\right]_0 = 0.1 \text{ to } 1 \frac{1}{\text{cm}^3\,\mu\text{s}} \tag{170}$$

The observed range is caused by the spread of cosmic and terrestrial radiation.

As can be seen from the measured results (48) plotted in Fig. 40, no pronounced dependency on the applied impulse voltage is observed. This indicates that under the conditions being investigated surface-related generation of primary electrons does not play an important part.

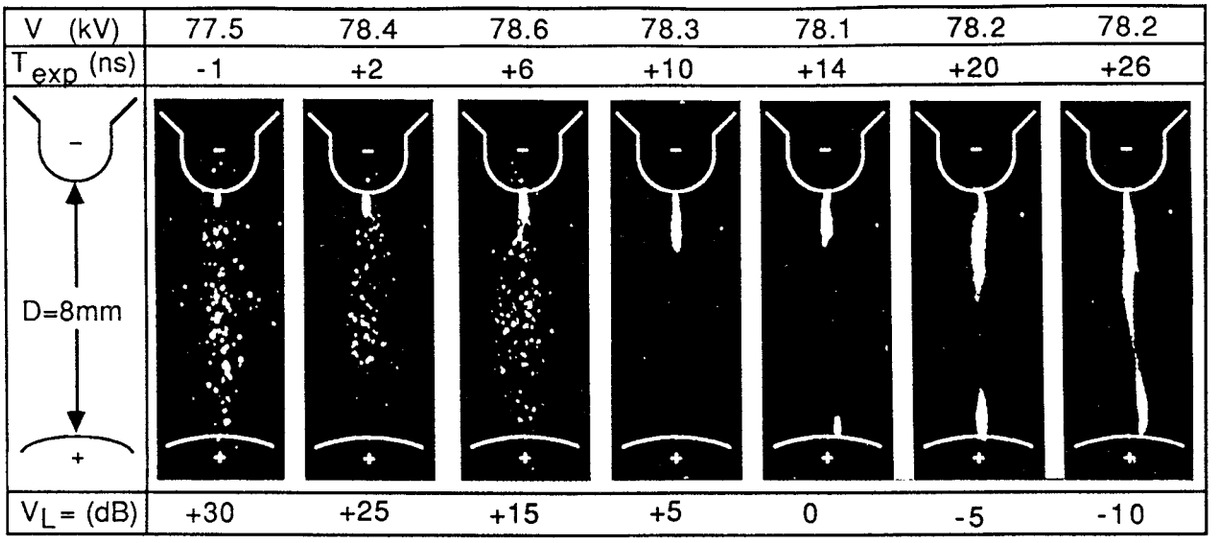

Figure 38. Optical analysis of the breakdown development in SF_6 for rectangular impulse voltage; negative polarity; UV ionization; $p = 1$ bar; $d = 8$ mm; relative overvoltage $(V - V_B)/V_B = 55\%$; $\eta = 0.62$.

Effective Electrons for Avalanche Formation. From Eq. (170) an estimate of the number of free electrons per unit time and per unit volume can be made. But in electronegative gases not all of them are really effective because very low electron multiplication is obtained for fields on the order of the limiting field $E \approx E_0$ and $\alpha/\eta \approx 1$ but with $\alpha > \eta$.

If the first ionization and attachment processes are analyzed in such cases, it is evident that statistically a single electron is not sufficient for avalanche development. During the first collision, which causes attachment or ionization, attachment or ionization occur with nearly equal probability. Therefore after this first collision this electron is attached with 50% probability and is no longer available for avalanche formation. The probability for ionization and the formation of two electrons is also 50%. For those that can also collide with molecules, the relevant probability for attachment is also 50%. The probability for the attachment of both electrons is 25%. After the second series of collisions the probability for attachment is 62.5% for each electron.

As a mean value, 1.6 primary electrons are required if avalanche growth is to be maintained after the second series of collisions. For higher fields and larger values of α/η fewer primary electrons are required. According to a statistical analysis (49) only a fraction $g(E)$

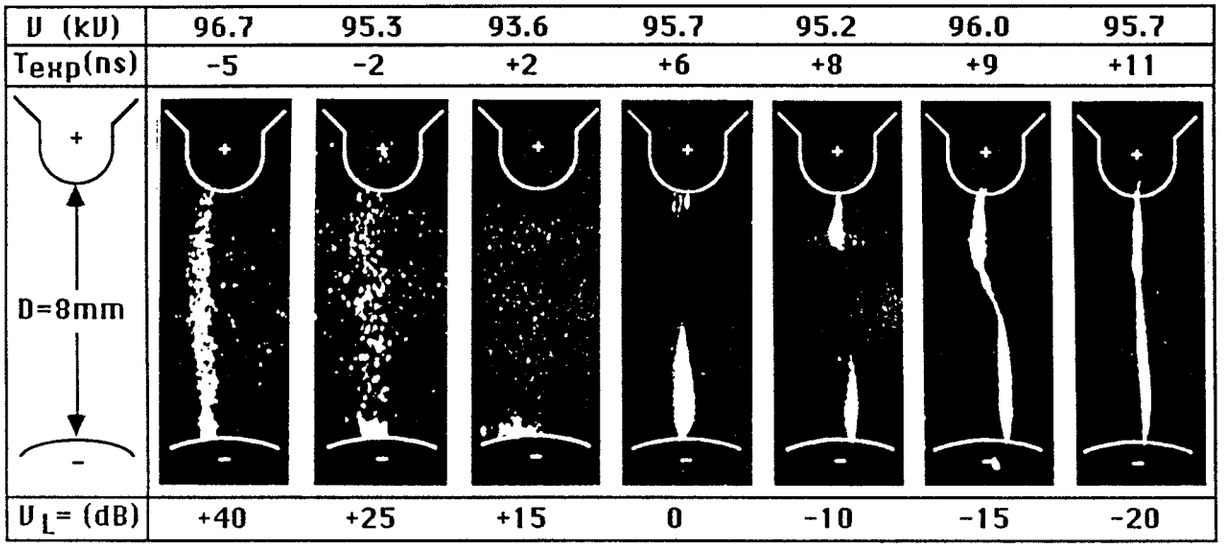

Figure 39. Optical analysis of the breakdown development in SF_6 for rectangular impulse voltage; positive polarity; UV ionization; $p = 1$ bar; $d = 8$ mm; relative overvoltage $(V - V_B)/V_B = 75\%$; $\eta = 0.62$.

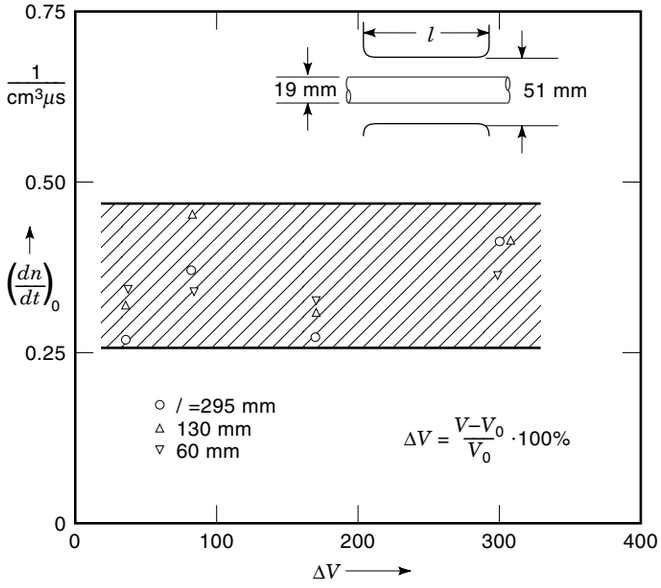

Figure 40. Effective generation rate of primary electrons $(dn/dt)_0$ for coaxial cyclindrical electrodes with different lengths depending on the applied impulse voltage V (1.2 /50 μs) related to V_0 (48).

$$\begin{aligned} g(E) &= 1 - \eta/\alpha \quad \text{for} \quad \alpha \geq \eta \\ g(E) &= 0 \qquad\quad \text{for} \quad \alpha < \eta \end{aligned} \tag{171}$$

of the primary electrons are effective for avalanche growth.

The weight function $g(E)$ depends on the reduced field E/p, as shown in Fig. 41 for SF_6 (1). Because the development of an avalanche of critical size is not possible for $\alpha < \eta$, the weight function $g(E) = 0$ in this condition. Based on that criterion, a so-called effective number of primary electrons $N(t)$ can be calculated, which are located in those parts of the discharge volume where the condition $g(E) > 0$ is fulfilled.

For this calculation the discharge volume is subdivided by equipotential lines in volume elements with equal mean field. For each volume element dV the mean number of effective

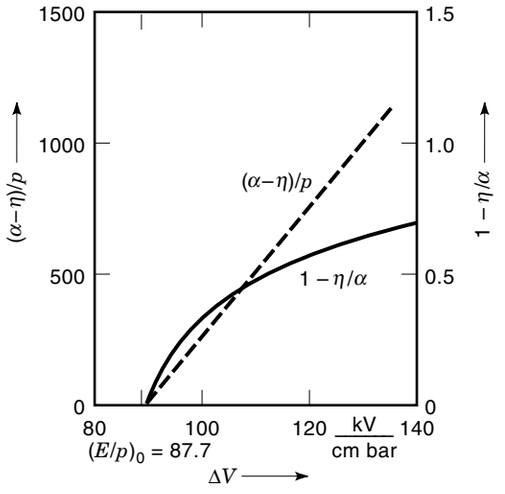

Figure 41. Weight function $g(E) = 1 - \eta/\alpha$ and reduced effective ionization coefficient $(\alpha - \eta)/p$ for SF_6 (1).

electrons $N(t)$ can be calculated (50)

$$\frac{dN(t)}{dt} = \left[\frac{dn}{dt}\right]_0 g(E)\, dV \tag{172}$$

$$N(t) = \left(\frac{dn}{dt}\right)_0 \int_{t_0}^{t} \int_V g(E)\, dV\, dt \tag{173}$$

where the gap volume is V and the time t_0 when the maximum field in the gap exceeds the limiting field E_0 at voltage V_0. With the weighted volume V_g

$$V_g = \int_V g(E)\, dV \tag{174}$$

the mean number of effective electrons is given by

$$N(t) = \left(\frac{dn}{dt}\right)_0 \int_{t_0}^{t} V_g\, dt \tag{175}$$

Equation (175), called the volume–time law (51,52), gives the mean number of electrons effective for avalanche growth. Even for a specific electrode arrangement, the weighted volume V_g and the mean number of effective electrons depend on the voltage and also on the time, if the voltage is not constant. For $t \leq t_0$ we obtain:

$$V_g(v) = 0 \quad \text{for} \quad V \leq V_0 \quad \text{and} \quad t \leq t_0 \tag{176}$$

$$N(t) = 0 \quad \text{for} \quad V \leq V_0 \quad \text{and} \quad t \leq t_0 \tag{177}$$

For $t > t_0$ the mean number of effective electrons $N(t)$ increases. According to Eq. (175), the probability $dP_e(t)$ for the availability of an effective primary electron in the time interval dt is given by

$$dP_e(t) = \left(\frac{dn}{dt}\right)_0 V_g(t)\, dt \tag{178}$$

Breakdown can be initiated only in this time interval, if it did not already occur. If the probability for a breakdown in the time interval between 0 and t is $P(t)$, then the probability that no breakdown will occur in this time interval is $1 - P(t)$. In the time interval between t and $t + dt$, therefore, the probability for a breakdown will be:

$$dP(t) = [1 - P(t)] \left(\frac{dn}{dt}\right)_0 V_g(t)\, dt \tag{179}$$

The solution of this differential equation is (53):

$$P(t) = 1 - \exp\left[-\left(\frac{dn}{dt}\right)_0 \int_{t_0}^{t} V_g(t)\, dt\right] \tag{180}$$

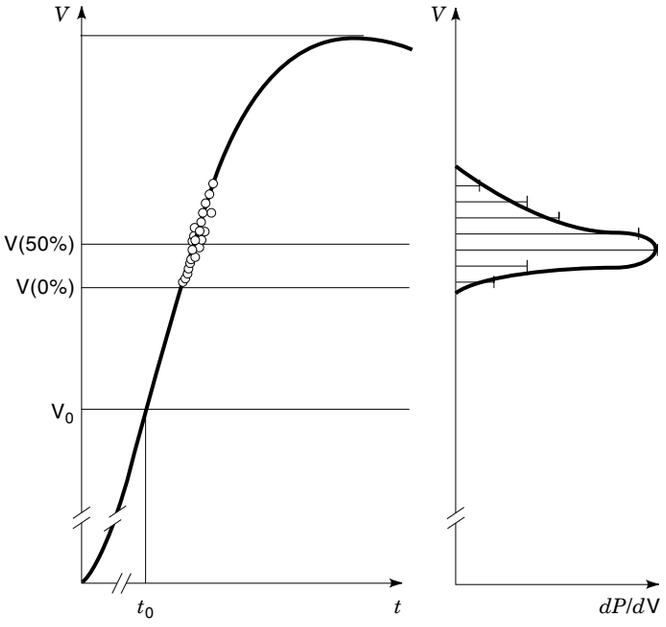

Figure 42. Impulse voltage, distribution of the occurrence of breakdown, and density of the breakdown probability (solid lines are calculated; points and bars are measured values) for breakdown in SF_6 (51).

From Fig. 42 it can be seen that by this method of calculation the probability for breakdown can be analyzed rather precisely. On the left side of the diagram, within the course of the impulse voltage, the value of the impulse resistance voltage $V_{0\%}$ and the measured values of the breakdown voltages have been marked. The density of the calculated and measured values of the breakdown probability are shown on the right side.

Formative Time Lag

The time for avalanche multiplication together with the time for streamer propagation is the formative time lag t_F.

After the availability of effective electrons, the time for avalanche multiplication to the critical size N_{cr} is rather short. Mainly depending on the gas pressure and the overvoltage, time intervals between 10 ns and 100 ns are typical. Longer time intervals occur if successive electron avalanches develop in cases of very low overvoltage.

The time for streamer propagation is also strongly influenced by parameters like gas pressure, gap width, and field distribution. As shown in Fig. 14 this time can be extremely short and is less than 10 ns in small gaps and for high gas pressure.

The variety of possible situations is nearly unlimited given the influence of the overvoltage. To give some idea of practical situations, an example is given in Fig. 43 for the formative time lags of rather small gaps in N_2 (54). For a nearly homogeneous field distribution, the data indicate formative time lags in the order of 100 ns for overvoltages of a few percent. For nonhomogeneous gaps, the situation is more complicated because higher overvoltages are required to obtain these rather low formative time lags. In SF_6, these characteristics differ significantly (54).

For larger gaps and approximately homogeneous field distribtion many successive streamers, as described in Streamer Discharge, develop. It is not practical to perform calculations for this development. Good results, however, have been ob-

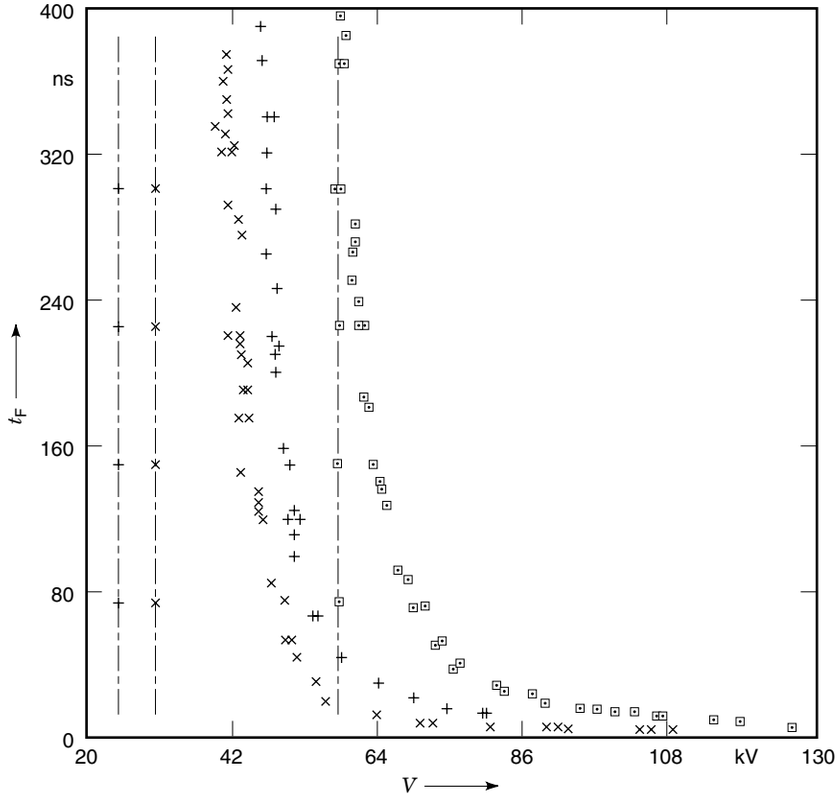

Figure 43. Formative time lags in N_2; $p = 1$ bar; $d = 20$ mm; □ − $\eta = 0.76$; × − $\eta = 0.24$; + − $\eta \approx 0.04$; the dotted lines are the dc breakdown voltage; the symbols are the measured formative time lags (54).

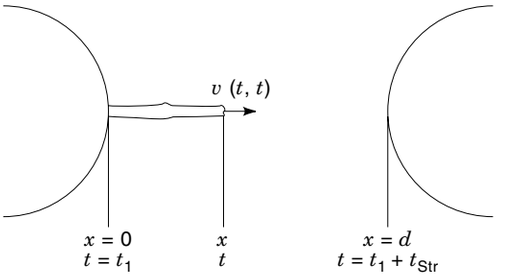

Figure 44. Model of streamer propagation (55).

tained by using an empirical equation, the voltage-time-area criterion (55).

This criterion is developed from a simple physical model. It is assumed that the progression of the streamer channel occurs with a velocity $v(x, t)$, which varies with the location and the time (Fig. 44). At the location x and the time t the propagation is given by

$$dx = v_x(x, t)\,dt \tag{181}$$

For fields smaller than $E_1(x)$, based on the applied voltage V_1, no streamer propagation occurs.

$$v_x(x, t) = 0 \quad \text{for} \quad E(x, t) \le E_1(x) \quad \text{and} \quad V(t) \le V_1 \tag{182}$$

For $V(t) > V_1$ the threshold field $E_1(x)$ is exceeded and streamer progression occurs with a velocity, which is assumed to be proportional to the difference between the actual field and the threshold field:

$$v_x(x, t) = K[E(x, t) - E_1(x)] \quad \text{for} \quad E(x, t) > E_1(x) \tag{183}$$

The influence of space charges is neglected. Therefore the field $E(x, t)$ can be calculated on the basis of the value of the voltage $V(t)$ at the time t and a function $g(x)$, which depends on the electrode geometry:

$$E(x, t) = V(t)g(x) \tag{184}$$

Accordingly the threshold field $E_1(x)$ is calculated from the voltage V_1:

$$E_1(x) = V_1 g(x) \tag{185}$$

The velocity of the streamer progression is obtained from Eqs. (183)–(185)

$$v_x(x, t) = K g(x)[V(t) - V_1] \tag{186}$$

From Eq. 181 the result is

$$\int_0^d \frac{1}{K}\frac{dx}{g(x)} = \int_{t_1}^{t_1+t_{\mathrm{Str}}} [V(t) - V_1]\,dt \tag{187}$$

The left side of Eq. (187) depends only on the electrode geometry. The right side is given by the voltage amplitude and shape related to the threshold voltage. The lower integration limit t_1 corresponds to the start of the streamer progression. At the upper limit $t_1 + t_{\mathrm{Str}}$ the streamer has reached the opposite electrode. Because the left side of Eq. (187) is constant for a specific electrode geometry, the voltage–time–area criterion is given by

$$\int_{t_1}^{t_1+t_{\mathrm{Str}}} [V(t) - V_1]\,dt = A \tag{188}$$

The voltage–time area A depends on the electrode geometry and increases with the gap width d. Therefore it is appropriate to use the reduced voltage–time area A/d, which can be considered constant, if classification of the geometry of the gap is performed before according to Table 10 (56).

For small gap widths and approximately homogeneous field distribution, the reduced voltage–time area is also defined as A/V_1 (57,58).

If the threshold voltage V_1 and A are known for a certain gap, the impulse resistance voltage for any applied voltage shape can be determined by using the voltage–time–area criterion, as long as the total time lag is determined mainly by the streamer formation. Therefore the threshold voltage is identical to the breakdown voltage for long-term voltage stress. As an approximation, the voltage–time–area criterion can also be used in the case of leader discharge.

Spark Formation Time

After the formative time lag has passed, an additional phase with the duration t_{B} is needed to complete the breakdown by forming a highly conductive spark channel, which is followed by voltage collapse. This spark formation time t_{B} can be described by several spark laws.

The following calculation is based on Toepler's spark law (59,60) which is supported by a simple physical model (61). The spark law of Rompe and Weizel (62) has similar characteristics but does not provide any advantage nor higher precision. The spark law of Braginskij (63) is better suited to describe the rapid expansion of the spark channel after the completion of the voltage collapse, but this feature is not important within high voltage engineering. A recent comparison has again shown the superiority of Toepler's spark law (64).

The following model provides some explanation for the background of Toepler's spark law (61). It is assumed that a weakly conducting channel is formed after propagation of the streamer between the electrodes. As the gas temperature is still rather low within this channel, thermoionization (see Thermoionization) is neglected. The conductivity of this channel is increased by collision ionization. Due to the low mobility of the ions the current is caused only by the movement of electrons. The current density S is obtained from

$$S = e n_{\mathrm{e}} b_{\mathrm{e}} E \tag{189}$$

Table 10. Reduced Voltage–Time Area A/d for Different Gap Geometries in Air[a]

Electrode Arrangement	A/d, kV · μs/m
Positive point–plane electrodes	650
Negative point–plane electrodes	400
Positive point–point electrodes	620
Negative point–point electrodes	590

[a] Ref. 56.

where the electron densities n_e, the electron mobility b_e and the axial field E in the spark channel. According to the effective ionization coefficient $\alpha-\eta$, the following increase of electron density dn_e is obtained by collision ionization:

$$dn_e = (\alpha - \eta) n_e \, dx \tag{190}$$

during the movement on the path dx:

$$dx = b_e E \, dt \tag{191}$$

The temporal increase of electron density is obtained from Eqs. (190) and (191):

$$\frac{dn_e}{dt} = \frac{dn_e}{dx}\frac{dx}{dt} = (\alpha - \eta) n_e b_e E \tag{192}$$

Combined with Eq. (189), the electron density at time t after the start of the formation of the spark channel is obtained from Eq. (192)

$$n_e(t) = \frac{\alpha - \eta}{e} \int_0^t S \, dt \tag{193}$$

The time-dependent specific resistance $\rho = E/S$ of the spark channel is calculated from Eq. (189) and (193):

$$\rho(t) = \frac{1}{(\alpha - \eta) b_e \int_0^t S \, dt} \tag{194}$$

If a homogeneous current density is assumed within the spark channel of area A_F, which is assumed to be approximately constant, the time-dependent resistance of the spark channel with length d is given by

$$R_F(t) = \rho(t)\frac{d}{A_F} = \frac{d}{(\alpha - \eta) b_e \int_0^t i \, dt} \tag{195}$$

Because the effective ionization coefficient $(\alpha - \eta)$ increases with the field E (Figs. 10 and 11) and the electron mobility b_e decreases with E [Eq. (46) and Fig. 6], the product of both is regarded as constant:

$$(\alpha - \eta) b_e = \frac{1}{k_T} = \text{const} \tag{196}$$

Thereby Toepler's spark law is obtained:

$$R_F(t) = \frac{k_T d}{\int_0^t i \, dt} \tag{197}$$

Experimental data for the spark constant k_T, which is slightly dependent on the breakdown field E_B, are shown in Fig. 45 (65,66). An overview is given in Table 11 (65–67).

To provide some data for the practical application of Toepler's spark law, it is assumed that a coaxial line with characteristic impedance Z_L has been charged to the breakdown voltage V_B of the spark gap with the gap width d and is discharged across the spark channel with spark resistance R_F. Based on the equivalent circuit in Fig. 46 and by neglecting the spark inductance L_F and the electrode capacitance

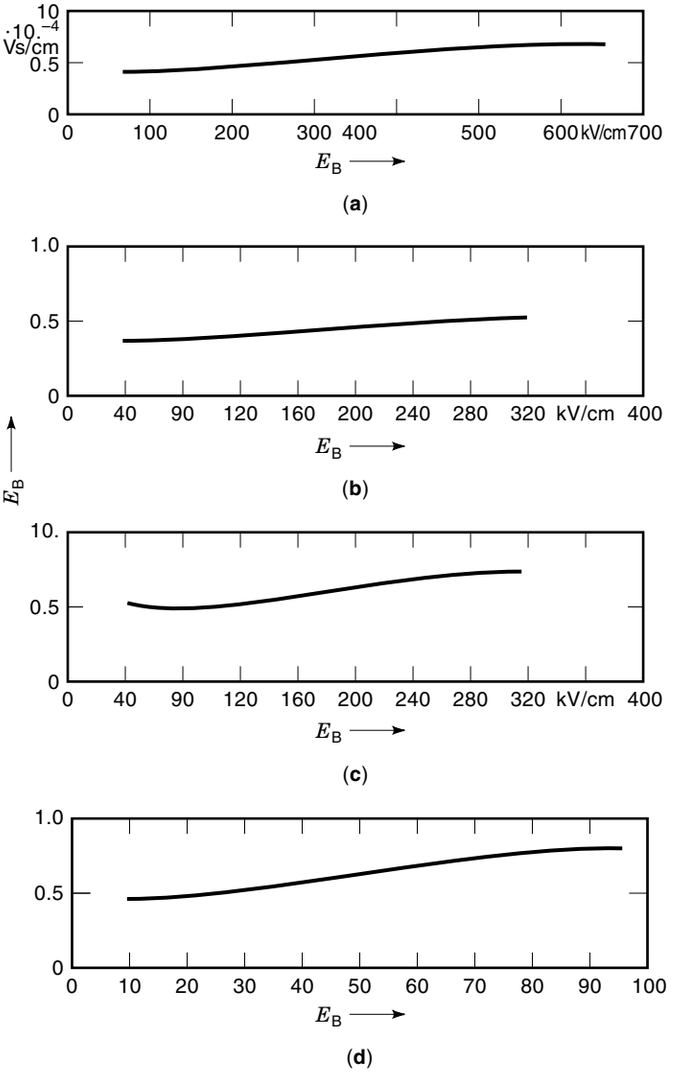

Figure 45. Experimental data for k_T in (a) SF_6, (b) N_2, (c) CO_2, and (d) Ar; gap widths 0.5 to 6 mm; gas pressure 1 to 8 bar (65,66).

C_p, the discharge current is given by

$$i(t) = \frac{V_B}{R_F(t) + Z_L} \tag{198}$$

The discharge current is referred to its peak value:

$$y = \frac{i}{I_{max}} \qquad I_{max} = \frac{V_B}{Z_L} \tag{199}$$

Table 11. Spark Constant k_T for Different Gases[a]

Gas	k_T, Vs/cm
Air	$(0.45–0.65)\cdot 10^{-4}$
SF_6	$(0.4–0.65)\cdot 10^{-4}$
N_2	$(0.4–0.55)\cdot 10^{-4}$
Co_2	$(0.5–0.7)\cdot 10^{-4}$
Argon	$(0.9–1.6)\cdot 10^{-4}$

[a] Refs. 65–67.

$$i(t) = \frac{V_B}{R_F(t) + Z_L}$$

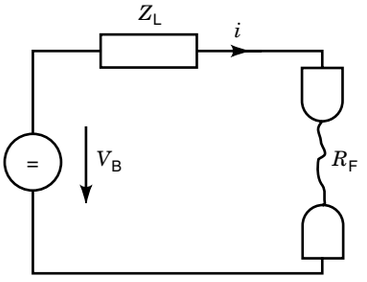

Figure 46. Equivalent circuit for the discharge of a coaxial line across the spark resistance.

Combined with Eq. (197) for the spark resistance, this results in

$$\frac{k_T d}{\int i\,dt} = \frac{V_B}{i} - Z_L = Z_L\left(\frac{I_{max}}{i} - 1\right) = Z_L\frac{1-y}{y} \tag{200}$$

$$\int y\,dt = \frac{k_T}{E_B}\frac{y}{(1-y)} \tag{201}$$

The solution is obtained by differentiation, separation of the variables, and partial fraction development (61):

$$dt = \frac{k_T}{E_B}\frac{dy}{y(1-y)^2} = \frac{k_T}{E_B}\left[\frac{1}{y} + \frac{1}{1-y} + \frac{1}{(1-y)^2}\right]dy \tag{202}$$

This results in an implicit solution for the referred discharge current:

$$t = \frac{k_T}{E_B}\left(\ln\frac{y}{1-y} + \frac{1}{1-y} + C\right) \tag{203}$$

The physical meaning of the integration constant C is the fact that any spark law can describe only the high-current phase of the discharge development, so that a minimum initial current has to be defined. For practical reasons this initial current is chosen as 0.01 I_{max}, which results in $y = 0.01$. The rise time of the discharge current is obtained from

$$T_A = 13.3\frac{k_T}{E_B} \tag{204}$$

Because the circuit in Fig. 46 is purely resistive, this time is identical to the time for the voltage breakdown across the gap, which is the spark formation time t_B.

Because the spark formation time depends only on the breakdown field E_B, it is much smaller in SF_6 than in air at the same pressure. For very high fields and small spark formation times, it is necessary to take the leakage reactance into account.

Compared to the other contributions to the time lag until breakdown, the spark formation time usually is the smallest part. During many evaluations, it is even not taken into account, because the beginning of the voltage collapse is already chosen for the definition of the breakdown.

Voltage–Time Characteristics

It is assumed that the test specimen is stressed with impulse voltage of equal shape and varying amplitude. The amplitude of the impulse voltage is plotted versus the time to breakdown. Thereby the voltage–time characteristics for this specific impulse shape are obtained. An example of such characteristics is shown in Fig. 47 (68).

Because the time lag to breakdown has a statistical spread, a band of voltage-time characteristics is obtained. The lower limit of this band is given by the 0% breakdown voltage ($V_{0\%}$) and the upper limit by the 100% breakdown voltage ($V_{100\%}$).

For dimensioning, the lower limit of the voltage–time characteristics has to be taken into account. These values are determined by the formative time lag (and the spark formation time). Very short formative time lags are obtained for approximately homogeneous field distribution and in gases with a steep increase in the effective ionization coefficient. Therefore the voltage-time characteristics of SF_6-insulated apparatus usually are much more uniform than those of air insulation.

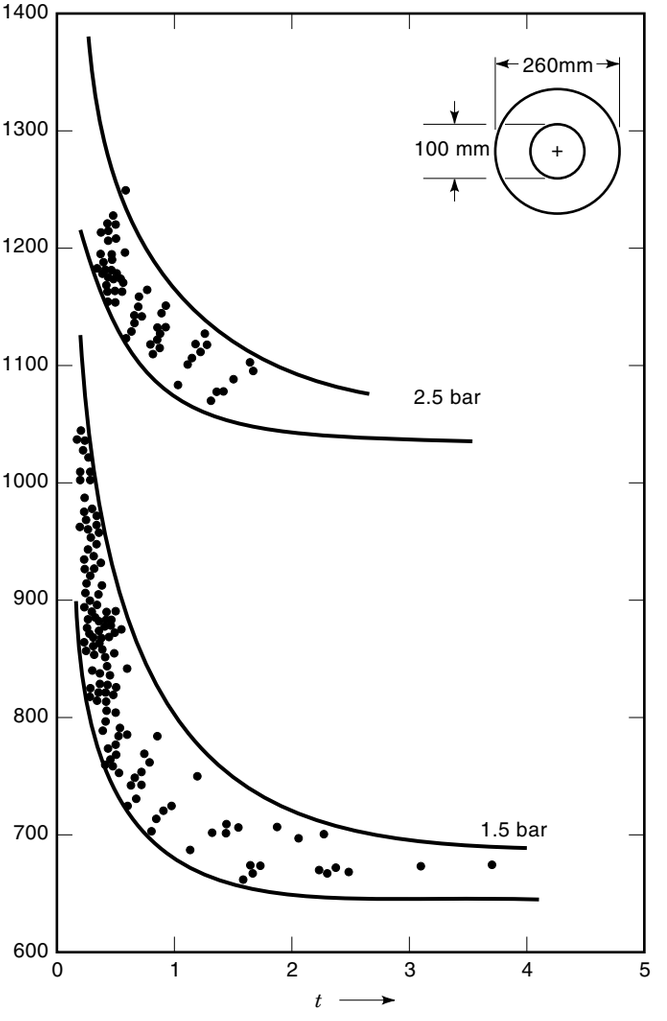

Figure 47. Calculated (solid lines) and measured (dots) voltage-time characteristics in SF_6 for impulse voltage (1.2/50 μs) (68).

FLASHOVER AT INSULATOR SURFACES

Two different arrangements are shown in Fig. 48 where breakdown development occurs along the surface of an insulator.

In the arrangement shown in Fig. 48(a), creeping discharges occur, which develop perpendicular to the field lines. Because regular discharges, which would develop along the field lines, are impeded by the high resistance of the solid insulating material.

In the arrangement shown in Fig. 48(b), the macrofield is not influenced by the insulator. However because of roughness of the insulator surface and tiny gaps at the electrodes (triple-junction), the microfield is likely to be enhanced. Especially at high gas pressure and in SF_6 (because of the high local electron multiplication), some reduction of the breakdown voltage compared with that of the gas gap has to be taken into account. Additional problems occur because of contamination of the insulator surface by humidity and other pollution. This aspect, however, is not dealt with in this article.

Creeping Discharges

With the arrangement shown in Fig. 48(a), creeping discharges can develop along the insulator surface. These creeping discharges are conducted by the contour of the insulator. A strongly nonhomogeneous field distribution is obtained especially for larger dimensions of the insulator surface. This results in a breakdown mechanism similar to the leader mechanism which usually occurs only in very long gaps of some meters (see Leader Discharge).

The reason for this phenomenon, which occurs at much smaller distances of some centimeters, is the high capacity of the plane electrode and the resulting displacement current across the insulator. Therefore the frequency of the voltage and the permittivity of the insulator are important influencing factors. It is obvious that such a discharge does not occur during pure dc voltage stress.

Because high displacement currents are generally obtained for high-frequency voltages (see High-Frequency Breakdown), it must be expected that for rather short gaps, leader-like discharges also occur.

To develop creeping discharge, the capacitance between a surface element and the plane electrode is decisive (1). Therefore the capacitance ΔC_0 per unit area is defined. For an insulator thickness d, capacitance is given by

$$\Delta C_0 = \epsilon_0 \epsilon_r \frac{1}{d} \tag{205}$$

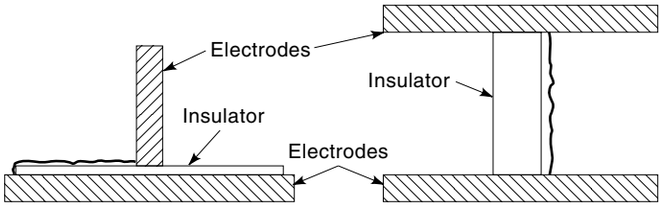

Figure 48. Breakdown at the insulator surface. *Left:* electrical field perpendicular to the insulator surface; *right:* electrical field parallel to the insulator surface.

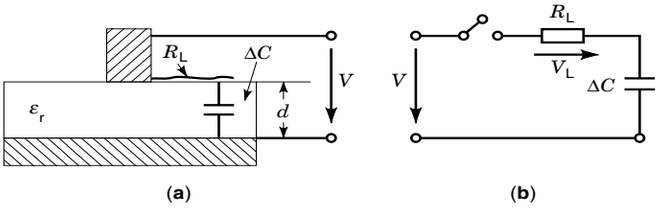

Figure 49. (a) Creepage arrangement; (b) with equivalent circuit (1).

Figure 49 shows the creepage arrangement and its equivalent circuit. The displacement current is supplied across the leader-like discharge channel with resistance R_L. The area with the streamer-like discharges and the total involved capacitance ΔC

$$\Delta C = k \Delta C_0 \tag{206}$$

is charged and discharged by this current. A rapid charge of ΔC is obtained only if the resistance R_L is low, so that a small time constant τ

$$\tau = R_L \Delta C \tag{207}$$

is obtained. Therefore the resistance R_L is the key factor for discharge development. The value of R_L depends on the degree of ionization, that is, the heating, of the leader-like channel. For heating, the energy dissipation in R_L is relevant. This energy W_L can be approximated from Fig. 49 if the supply voltage V is assumed as a rectangular pulse:

$$W_L = \frac{1}{2} \Delta C V_L^2 \tag{208}$$

where V_L is the voltage across the leader-like discharge. If W_L reaches energy W_{Th}, which is required for thermoionization (see Thermoionization), the leader inception voltage V_{Li} is reached:

$$W_{Th} = \frac{1}{2} \Delta C V_{Li}^2 \tag{209}$$

The leader inception voltage is obtained from Eqs. (205), (206), and (209):

$$V_{Li} = \sqrt{\frac{2W_{Th}}{k \Delta C_0}} = \sqrt{\frac{2W_{Th}}{k \epsilon_0 \epsilon_r} d} \tag{210}$$

For ac voltage an empirical formula, similar to the results of the model presented, is used to determine V_{Li}:

$$V_{Li} = 75\,\text{kV} \left(\frac{1}{\epsilon_r} \frac{d}{\text{cm}} \right)^{0.44} \tag{211}$$

Such creeping discharges may not occur in service nor during test. According to Eqs. (210) and (211), a sufficient thickness of insulating material and a low permittivity are required to obtain a high value of V_{Li}.

Surface Flashover

The following considerations are focused on discharges described in Fig. 48(b). The possible interactions between the

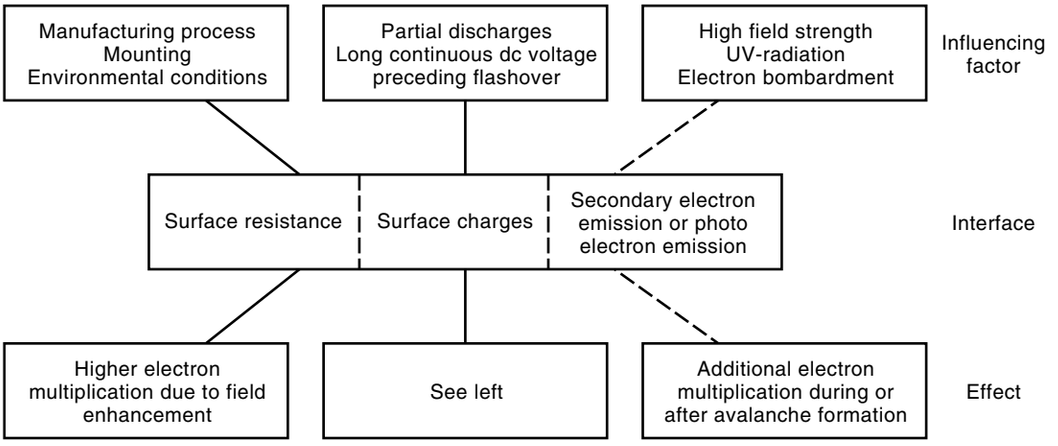

Figure 50. Possible interfacial effects between gaseous and solid dielectrics (44).

insulator surface and the gas discharge are summarized in Fig. 50 (44). For that purpose, an insulator model has been developed, which provides well defined experimental conditions (45). This model is shown in Fig. 51 in both the head-on (a) and the side view (b). Because of electrode geometry and the coaxial outer conductor, an approximately homogeneous field is obtained, and the highest field is at the ungrounded electrode.

Using this model ensures that the macrofield in the gap is not influenced by the insulator surface. The insulator surface is located in the area with the highest macrofield, where the discharge development is likely to occur. In this way any possible interaction between the insulator surface and the discharge development can take place. If these conditions are not met as a result of moving the insulator surface slightly outside this area, the influence of the insulator on the breakdown development is greatly reduced (69).

To focus on the interaction between insulator surface and gas discharge, any additional effects like contamination of the surface should be excluded by careful cleaning. Triple-junction phenomena at the electrode surface should be excluded by metallic coating the relevant insulator surface. The result of such investigations (46) is shown.

Comparing the breakdown voltages of N successive flashover events in the gas gap shows that in SF_6 some scatter always occurs, whereas in N_2 even at 5 bar the values are much more reproducible. Insulating only with N_2 at 2 bar, the scatter of the breakdown voltages is small. At 5 bar, reduced breakdown voltages already occur with significant scatter (Fig. 52) (46). This is still more pronounced in SF_6, especially for the higher gas pressure of 2.4 bar (Fig. 53) (46). In this case, the mean value of the breakdown voltage is also significantly lower than in the gas gap. As the macrofield in N_2 at 5 bar is comparable with that in SF_6, it can be concluded from the breakdown voltage measurements that the amount of interaction between gas discharge and insulator surface depends strongly on the field or the gas pressure, respectively.

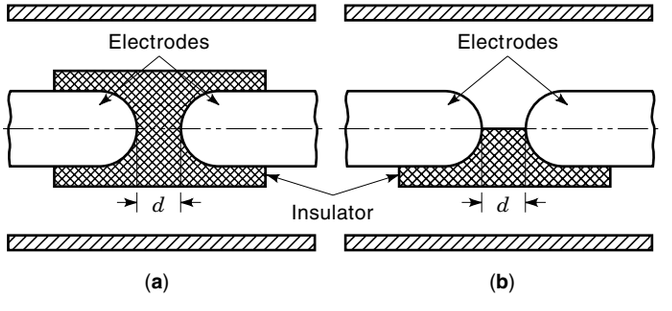

Figure 51. Insulator model for surface flashover experiments (45); (a) head-on view; (b) side view.

Discharge development can be evaluated by high speed framing of the prebreakdown phenomena with 1 ns exposure time. To obtain more information about the interaction between gas discharge and insulator surface, it is essential to achieve a three-dimensional view. For this purpose nearly simultaneously photographs of the side view and the head-on view were taken (46). This feature is of special interest if a high spatial scatter of the prebreakdown phenomena occurs, which is typical for compressed SF_6.

In N_2 at 2 bar the discharge development is influenced in the streamer phase only by the insulator. After discharge inception in the gas volume, the streamer approaches the insulator surface and its temporal progression is enhanced (Fig. 54). Therefore the breakdown voltage is nearly the same as in the gas gap.

For higher gas pressure of 5 bar, discharge inception in N_2 also occurs in the gas volume. In that case a rather high breakdown voltage is obtained. If the discharge inception occurs close to the insulator surface, a lower breakdown voltage occurs. Obviously, because of the short avalanche length at high gas pressure, local field disturbances at the insulator surface become more effective.

In SF_6 at 2 bar the influence of the insulator on discharge development is already much greater. Therefore discharge inception always occurs close to the insulator surface. This may occur near both electrodes or even in the middle of the gap (Fig. 55) (46). In such cases several luminous centers develop, which remain separated for some nanoseconds. Based on the very short avalanche length in SF_6, it has to be supposed that these are independently developing discharges. As soon as they grow together, a continuous prebreakdown channel is formed. In such cases generally the breakdown voltage is reduced significantly.

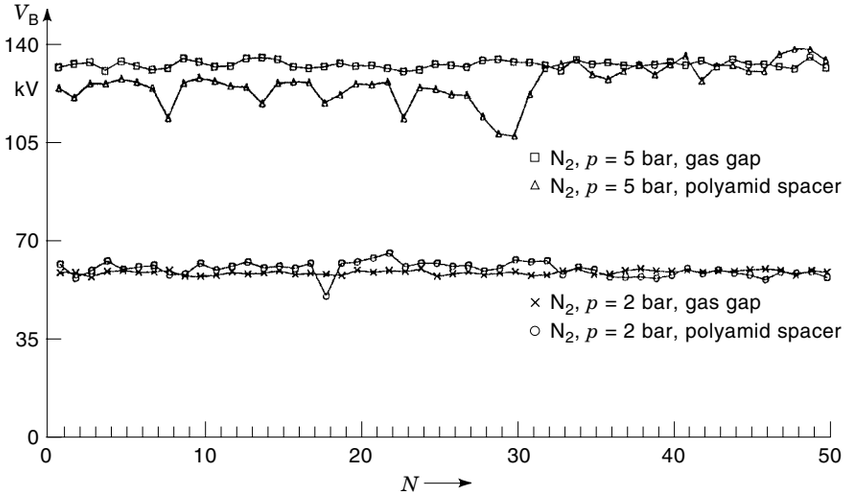

Figure 52. Breakdown voltage of the insulator model compared with the gas gap; N_2, d = 10 mm (46).

Discharge inception is greatly influenced, especially in SF_6, by the microfield at the insulator surface. Therefore the distribution of the macrofield (see Surface Effects) and, for instance, the polarity are of minor importance. This could be confirmed during measurements with negative polarity (of the ungrounded electrode) where discharge inception may also occur in the middle of the gap.

In N_2 at high pressure and in SF_6 in general discharge inception is already influenced by the insulator. The reason must be the greatly decreased avalanche length, which allows effective multiplication in the local enhanced microfield at the insulator. In N_2, this effect is limited to the anode region. In SF_6 it may occur even in the middle of the gap. In such cases, multiple avalanching takes place, and the breakdown voltage is reduced significantly.

HIGH-FREQUENCY BREAKDOWN

For ac voltage stress, it is generally assumed that the rate of variation of the amplitude of the sinusoidal voltage can be neglected during the breakdown time interval, which is required for discharge development. For power distribution frequencies and for gap widths of up to approximately 1 m, this is usually ensured by the rather fast discharge development caused by the high mobility of the electrons. If space-charge-induced phenomena are neglected, this results in identical ac (peak) and dc breakdown voltages. However, for voltage frequency significantly higher than 50/60 Hz it is no longer justified to assume that a constant voltage stress with the ac peak voltage is provided during the entire phase of discharge development. This results in an influence on the ac breakdown voltage (70).

Because of the low mobility ions, it can occur in high-frequency voltage stress that not all of the ions generated during electron multiplication are removed before the voltage polarity reverses. This results in an increasing number of ions within the gap and in an additional field distortion caused by space charges. Because of this field distortion the breakdown voltage is decreased. At very high frequency voltage the mobility of electrons also has to be taken into account. Thereby avalanche growth is impeded, because the voltage can already decrease before the critical number of electrons is obtained. This results in an increase of the breakdown voltage.

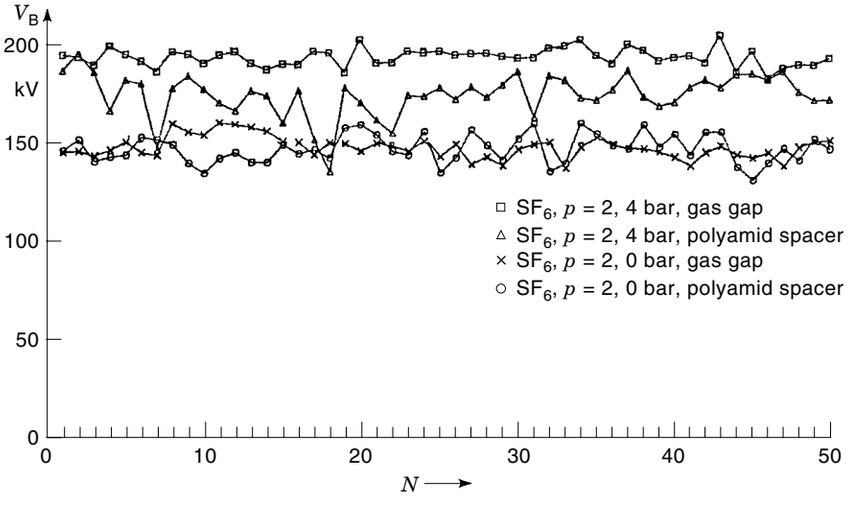

Figure 53. Breakdown voltage of the insulator model compared with the gas gap; SF_6, d = 10 mm (46).

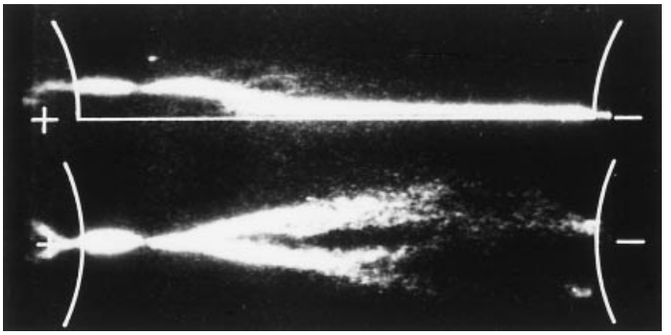

Figure 54. Discharge inception in N_2, d = 10 mm, p = 2 bar, V_B = 57.1 kV; upper: side view, lower: head-on view; −11/1000 means: T_{exp} = −11 ns is the moment of exposure (zero is the beginning of the voltage collapse): G_L = 1000 is the relative luminous gain of the image recording system (46).

For nonhomogeneous gaps, high-frequency voltage stress causes high displacement currents which induce leader development. This happens for rather low gap widths and results in an unexpected reduction of the breakdown voltage. Usually the voltage range where such phenomena occur is not obtained with steady-state sinusoidal voltages. However, this phenomenon also occurs with damped oscillating switching surges, which reach both high amplitude and frequency (71).

High-Frequency Breakdown in Approximately Homogeneous Gaps

For power distribution frequency, the rate of variation of the voltage of a sine wave near its peak value is very small. For instance, at a frequency of 50 Hz the voltage is equal to or higher than 99% of the peak value during a time interval of nearly 1 ms. In comparison, times which are required for discharge development (see Breakdown Characteristics) are so long that no influence of the variation of the voltage amplitude on discharge development is expected. Therefore for power distribution frequency, if space-charge phenomena are excluded (see Breakdown in Nonhomogeneous Fields), the ac breakdown voltages are essentially the same as the dc breakdown voltages.

For significantly increased frequency, the amplitude of the voltage already decreases or even the polarity reverses before discharge development is finalized. Therefore both the limited mobility of the ions and the electrons are responsible. Because of the much lower mobility of ions, the influence already occurs at rather low voltage frequency, whereas the mobility of electrons must be taken into account at much higher frequencies.

Ions generated during any prebreakdown phenomenon have to be removed from the gap. At high voltage frequency this may not be possible before polarity reversal occurs, resulting in a space charge-induced field distortion. Thereby the breakdown voltage is reduced, as described in detail later.

At very high voltage frequency the velocity of electrons [Eq. (50)] also has to be taken into account for such considerations. Thereby the avalanche growth is impeded, which re-

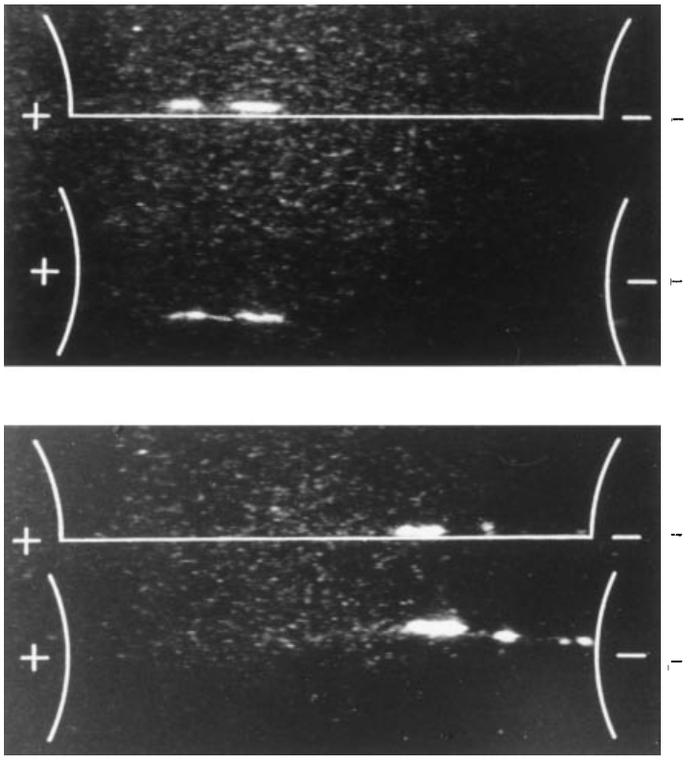

Figure 55. Discharge inception in SF_6; d = 10 mm; p = 2.4 bar; V_B: 153.7 kV (upper), 185 kV (lower) (46).

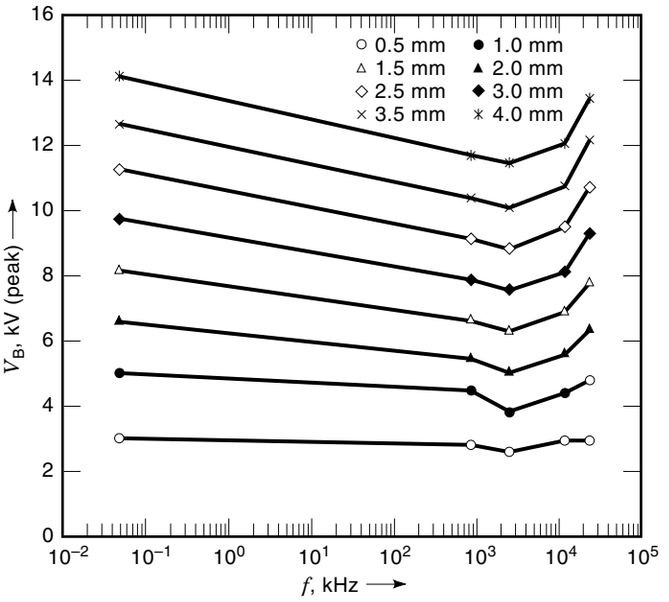

Figure 56. Breakdown at high-frequency voltage; air, approximately homogeneous field (73).

sults in an increase of the breakdown voltage, also described later. This phenomenon becomes effective at frequencies on the order of some 10 MHz, which usually only occur in RF transmitters (72).

Therefore the resistance of gaps with approximately homogeneous field distribution has a typical frequency dependency with a distinct minimum, as shown in Fig. 56 (73). Only for very small gaps of less than 1 mm essentially no frequency dependency of the breakdown voltage is observed because discharge development is very fast and practically no ions remain within such small gaps.

At power distribution frequencies, the ions generated during electron multiplication processes at the peak value of the applied sinusoidal voltage are completely removed from the gap in the time interval with decreasing field before the voltage polarity reverses. This can be shown by a simple consideration, where only the positive ions are regarded. In the case of electronegative gases, because of the effect of negative ions and the possible neutralization of space charges, this effect is smaller (70).

It is assumed that positive ions have been generated at the peak value of the applied voltage and that the majority of the ions are near the anode. During the following quarter period of the sinusoidal voltage, the positive ions move back to the cathode and are collected if no polarity reversal of the applied voltage occurs before all of them arrive at the cathode. According to Eq. (31), the ions move the following distance s_1 during that time:

$$s_1 = \int_0^{t/4} v(t)\,dt = \int_0^{t/4} bE(t)\,dt \tag{212}$$

Because the applied external field decreases from its initial peak value E_0, the result is given by

$$s_1 = \int_0^{t/4} bE_0 \cos(\omega t)\,dt \frac{bE_0}{\omega} |\sin(\omega t)|_0^{t/4} = \frac{bE_0}{2\pi f} \tag{213}$$

According to Eq. (50), an initial velocity $v_0 = bE_0$ of approximately 0.6 mm/μs can be assumed for ions in air at a pressure of 1 bar. At a voltage frequency of 50 Hz, this would result in a distance $s_1 = 1.91$ m, which would be relevant only for very large gap widths d.

However, by increasing the frequency, the ions move only a correspondingly smaller distance until the polarity of the voltage is reversed. This is shown in Fig. 57. After being generated at the voltage peak, the ions move toward the cathode [Fig. 57(a)]. At the moment polarity reverses [Fig. 57(b)] a significant part of the positive ions have not reached the cathode. After the polarity reversal the remaining ions are moving in the opposite direction toward the new cathode [Fig. 57(c)]. However, during that time interval not all positive ions reach the cathode. Therefore a positive space charge remains within the gap.

During the negative part of the sinusoidal voltage the positive ions move by the following distance s_2:

$$s_2 = \int_{t/4}^{3t/4} bE_0 \cos(\omega t)\,dt = \frac{bE_0}{\omega} |\sin(\omega t)|_{t/4}^{3t/4} = -\frac{bE_0}{\pi f} \tag{214}$$

In case condition $|s_2| \le d$ cannot be fulfilled, positive ions remain within the gap and a reduction of the breakdown voltage has to be expected. From this condition a critical frequency f_{crit} based on Eq. (214) can be defined:

$$f_{crit} = \frac{bE_0}{\pi d} \tag{215}$$

In air at 1 bar this results in

$$f_{crit} \approx \frac{200}{d/\text{mm}}\,\text{kHz} \tag{216}$$

Beginning with f_{crit}, some reduction of the breakdown voltage occurs, as already shown in Fig. 56. The dependency of the critical frequency on the gap width can be seen more clearly from Fig. 58 (74).

For much higher voltage frequency, the mobility of the electrons also has to be taken into account to evaluate the influence of the frequency on breakdown development. According to Eq. (50) at the peak value of the voltage an initial velocity $v_0 = bE_0$ of approximately 150 mm/μs can be assumed for electrons in air at a pressure of 1 bar. If the resulting transit time of electrons becomes significant compared with the period of the high-frequency voltage, an increase of the voltage amplitude is required to reduce the transit time. Additionally the ionization coefficient is reduced with the decrease of the amplitude of the high-frequency voltage from its peak value. For both reasons the amplitude of the voltage has to be increased with higher frequencies to create an electron avalanche of critical size within the available time period.

Therefore the insulating characteristics of rather small gaps with homogeneous and approximately homogeneous field distribution with respect to the voltage frequency is summarized by the following statements (70):

- At frequency f_{crit} a reduction of the breakdown voltage begins. This reduction can be up to 20%.
- At MHz frequencies, the breakdown voltage has its minimum. By further increasing the frequency, there is a re-

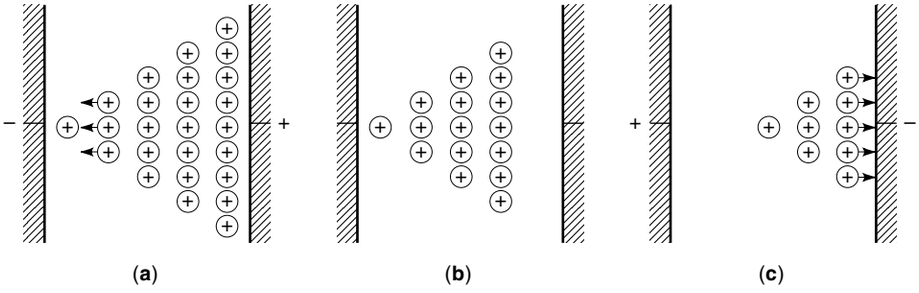

Figure 57. Formation of a positive space charge at high-frequency voltage; (a) ion density after the positive peak; (b) ion density at the polarity reversal; (c) ion density before the beginning of the next sine wave.

covery of dielectric strength which will exceed the breakdown strength at power frequency voltage.

High-Frequency Breakdown in Nonhomogeneous Gaps

The influence of frequency on the breakdown voltages is much more significant for nonhomogeneous gaps (75). This can be seen in Fig. 59 for rather large gap widths. The critical frequency still coincides reasonably with the approximation given before. However the amount of the reduction of the breakdown voltages is already about 50% for rather small gaps. The results are also strongly influenced by the electrode configuration. The lowest values were obtained for an ungrounded point electrode.

It has to be assumed that these phenomena are comparable to those observed in very long air gaps for rather slow switching surge phenomena (see Leader Discharge). The reason for this phenomenon, which already occurs at much lower distances of some centimeters, is the high displacement current in the leader-like discharges in spite of their short range. Therefore similar current densities are obtained, which would occur for leaders more than 1 m long in air.

Usually such strongly divergent fields and high amplitudes of the steady-state voltage are rare. However a similar situation may be obtained in the case of damped oscillating voltages of high frequency.

High-Frequency Breakdown for Switching Surges

The development of leader discharges at high frequency voltages also occurs with damped oscillating switching surges (very fast transient voltages; VFT-voltages), which reach high amplitude and high frequency (71). This aspect is of increasing interest (76–78), because such phenomena occur in encapsulated compressed gas insulated substations and apparatus and frequencies up to some 10 MHz are generated.

Some recent work is considered here (79,80), which was performed for a damped sinusoidal voltage stress in the frequency range of 3 to 12 MHz superimposed on a voltage step (dotted lines in Figs. 60 and 61). The ratio of the first peak of the damped VFT to the amplitude of the voltage step is in the range of 1.8 to 2.0, depending on the frequency of the VFT. To compare the characteristics of attaching and nonattaching gases, both pure SF_6 and N_2 and different mixtures of both have been investigated.

The electrodes with a Rogowski profile provide a nearly homogeneous basic field. This is distorted by a steel needle with a tip radius of 50 μm and 3 mm or 10 mm long, which

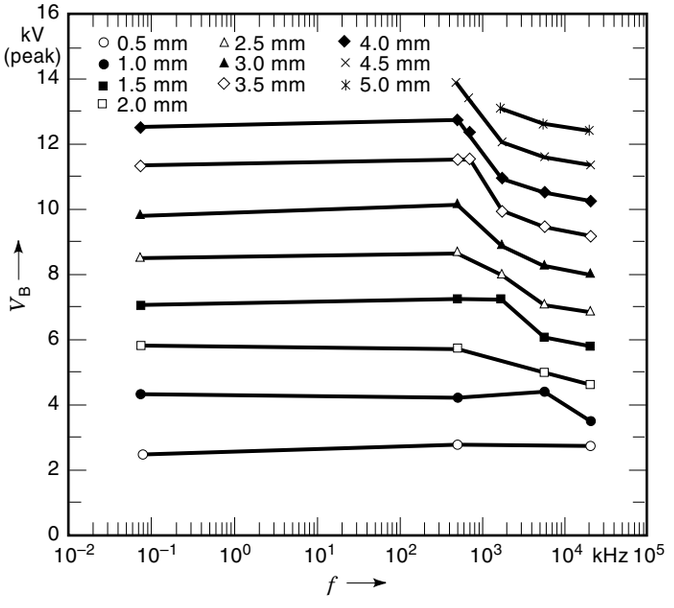

Figure 58. Breakdown at high-frequency voltage; air, approximately homogeneous field (74).

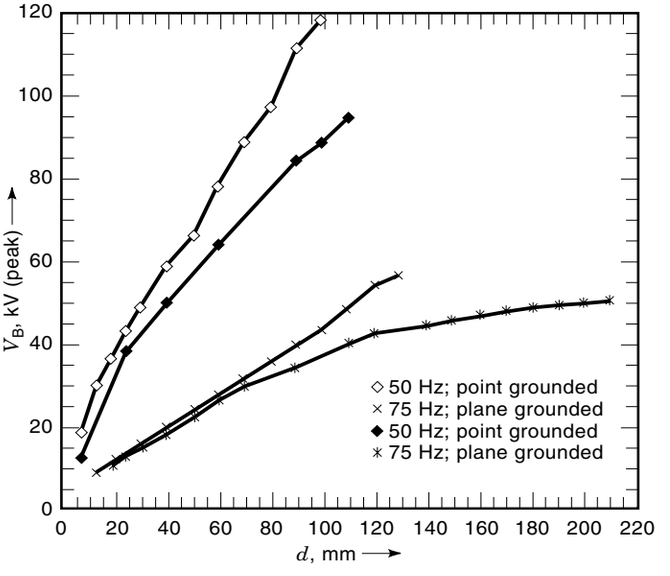

Figure 59. Breakdown at high-frequency voltage; air, nonhomogeneous field (point–plane electrodes) (75).

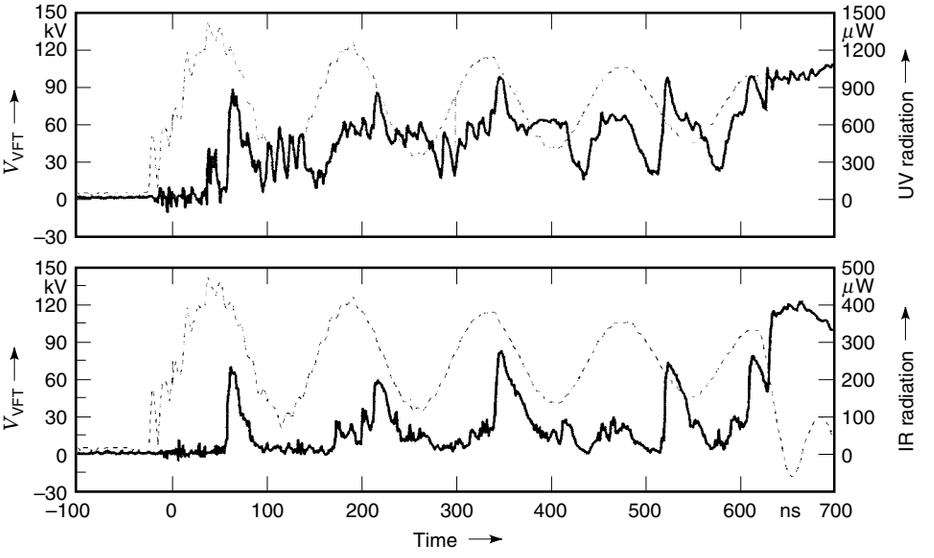

Figure 60. UV and IR radiation intensity for VFT-voltage stress of positive polarity with a frequency of 6 MHz; --- VFT-voltage; —— photomultiplier signals; d = 25 mm; η = 0.025; p = 1.5 bar (79).

is mounted in the center of the high-voltage electrode. The degree of homogeneity $\eta = E_{min}/E_{max}$ is 0.04 or 0.025 depending on the needle length.

In Fig. 62 the breakdown voltages of the nonhomogeneous SF_6 gaps with two different degrees of homogeneity of η = 0.04 and 0.025 stressed by VFT-voltage of variable frequency are shown (79). It can be seen that the VFT-voltage with a frequency of 3 MHz provides the smallest dielectric strength. However, the highest dielectric strength is not obtained for the highest frequency. For all pressures a frequency of 6 MHz leads to the highest dielectric strength.

In Fig. 62 some areas occur of decreasing dielectric strength for increasing gas pressure. These areas move toward smaller gas pressure with increasing frequency. This effect is caused by corona stabilization (81). The characteristics of corona-stabilized breakdown can be split into three regions separated by the pressure values p_1 and p_c. Up to the pressure p_1 the breakdown strength rises linearly with gas pressure and is much higher than the corona onset voltage because of corona stabilization. Between p_1 and p_c the breakdown voltage reaches a local maximum. After some decrease the breakdown voltage coincides with the corona inception voltage at the critical pressure p_c. For gas pressure higher than p_c, no difference is found between the corona inception and the breakdown voltage.

As indicated by the symbols in Fig. 62, the critical pressure decreases with increasing frequency and with decreasing degree of homogeneity. The breakdown strength rises slowly but linearly with the gas pressure for $p > 4$ bar, that is, in the region where the breakdown voltage coincides with the corona inception voltage.

In addition to electrical measurements, optical diagnostics of the prebreakdown phenomena were done. To record the prebreakdown phenomena, a solar-blind photomultiplier with high UV sensitivity (UV-PM) and an infrared sensitive photomultiplier (IR-PM) were used. The UV-PM is used to detect

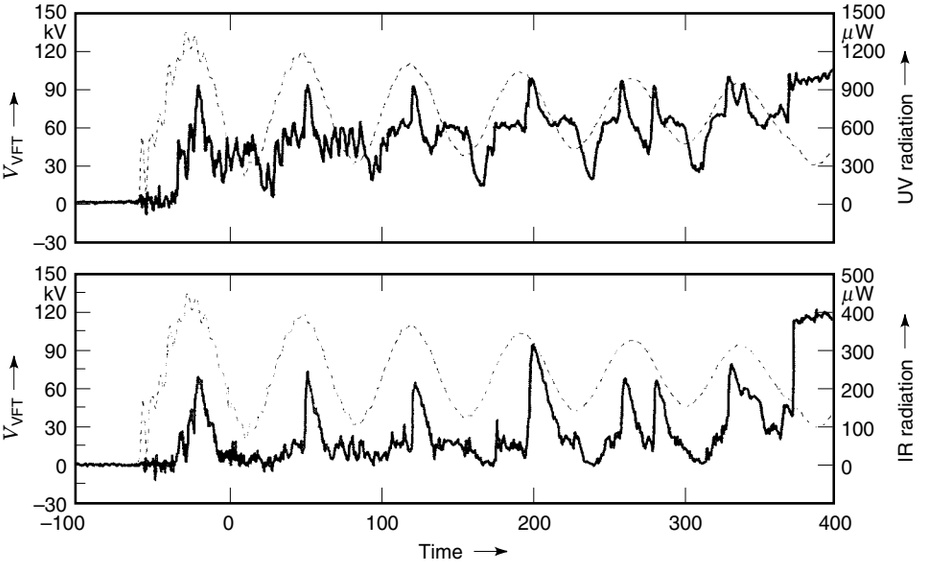

Figure 61. UV and IR radiation intensity for VFT-voltage stress of positive polarity with a frequency of 6 MHz; --- VFT-voltage; —— photomultiplier signals; d = 25 mm; η = 0.025; p = 2 bar (8,10).

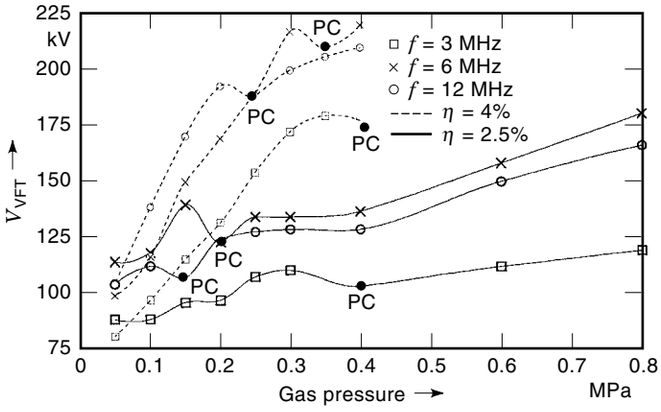

Figure 62. Breakdown voltage V_{VFT} of SF_6 for VFT-voltage stress of positive polarity for different gas pressures (0.1 MPa = 1 bar), frequencies, and degrees of homogeneity; d = 25 mm (79).

the line spectrum of the SF_6 molecule at a wavelength of 182.3 nm, which has to be expected during streamer inception. Using an interference filter with a center wavelength of 694 nm, the IR-PM is suited for detecting the line spectrum of atomic fluorine caused by the dissociation of SF_6 molecules during the leader phase. By evaluating such data it has to be kept in mind that a leader step and a streamer corona nearly coincide.

The recorded photomultiplier signals show that the discharge mechanism is changing at the critical pressure. For the 6 MHz VFT a precursor mechanism occurred for the pressure below the critical pressure of 2 bar. Figure 60 shows the signals of the photomultipliers for a 6 MHz VFT-voltage at a pressure of 1.5 bar (79). The precursor radiation, that is, the first peak in the UV signal, starts 20 ns before the first leader step is initiated. This matches well with the equations for the delay between precursor and leader inception (82). Breakdown occurs immediately after the fifth leader step.

At the critical pressure a mixture of stem mechanism and high-frequency mechanism was observed, as displayed in Fig. 61 (79). Ionization, that is, streamer corona and the development of leader segments occur shortly after the first four peaks of the test voltage. It is remarkable that the first leader segment occurs immediately after the start of UV radiation, that is, only a few nanoseconds after the first ionization. This behavior is characteristic of the stem mechanism (76). After the fourth peak, streamer corona and leader step occur at both slopes of the VFT-voltage. For one period of the VFT-voltage, UV and IR radiation are modulated with twice the frequency of the VFT-voltage. This behavior is typical for the high-frequency mechanism (76). A stem mechanism was observed for all frequencies of the voltage above the critical pressure.

The breakdown characteristics of nonhomogeneous gaps filled with SF_6 and stressed by very fast transient voltages is based on corona stabilization and characterized by the following regions:

- The region of linear increase of the dielectric strength with a streamer-based discharge ($p < p_1$).
- The transition region where a local maximum of dielectric strength is found and where, depending on the frequency streamer to leader transition based on the precursor, high-frequency or stem mechanism is found ($p_1 < p < p_c$).
- The region where the breakdown strength coincides with the corona inception voltage that has a streamer leader transition according to the stem mechanism ($p > p_c$).

Under real conditions in GIS, the resulting waveforms caused by switching operations are more complex and contain at least two main frequency components superimposed on a step voltage in the following frequency ranges (83,84):

- Fast transient components (FT) with frequencies between 0.1 and 5 MHz.
- Very fast transient components (VFT) with main frequencies below 30 MHz, on which low-amplitude signals at very high frequencies of up to 100 MHz are superimposed.

Voltage shapes with these different frequencies have to be considered especially when testing gas-insulated disconnectors (85). As an example, Fig. 63 shows four types of composite voltage stress in GIS with a subsequent voltage collapse caused by a needle-shaped protrusion. The outcoupling of the internal traveling surges leads to high damping. The main high-frequency components depend on the GIS configuration and the section lengths. For a single bus 11.5 m long, there is a main oscillation with 13 MHz, as shown in Fig. 63(d). The presence of external lumped-circuit components, for example, capacitive voltage transformers or coupling capacitors, causes a FT oscillation of about 1 MHz in Fig. 63(a), (b), and 3 MHz in Fig. 63(c). These external components are also responsible for different damping of the FT components in Figs. 63(a), (b), and (c).

The VFT stress has been systematically related to the lightning impulse (LI) resistance, which is generally the basis for GIS design. For sound insulating systems the VFT stress is covered by its resistance to standard LI (1.2/50 μs) (84). Special attention has to be paid when defects are present and in designing the disconnector itself. The mechanism of disconnector-triggered breakdown is well known, and the risk is covered by standardized tests (85). The nonhomogeneous fields caused by defects in the insulation system give considerably lower breakdown values. A minimum for LI has an initiation time of approximately 5 μs. Of special interest is the breakdown voltage of VFT compared to LI.

The influence of the applied voltage shape can be demonstrated by comparing the measured voltage–time (V–t) curves. The breakdown was investigated at a needle–plane gap, with the needle at positive potential at the end of the bus duct (86). As an example Figs. 64 and 65 show the measurements for a needle with a length l = 15 mm, a tip radius of 0.25 mm, a gap width d = 85 mm, and a gas pressure of p = 3 bar. The V–t curve under LI stress is taken as reference level for the severity of VFT and composite voltage stress.

The VFT component accelerates discharge development. Thus a VFT shape with small damping [Fig. 63(d)] gives the lowest breakdown levels. In the case of higher damping, as in practice, the values converge to the minimum breakdown levels for LI stresses. For composite voltage stresses, the relationship between the FT and VFT components determines the

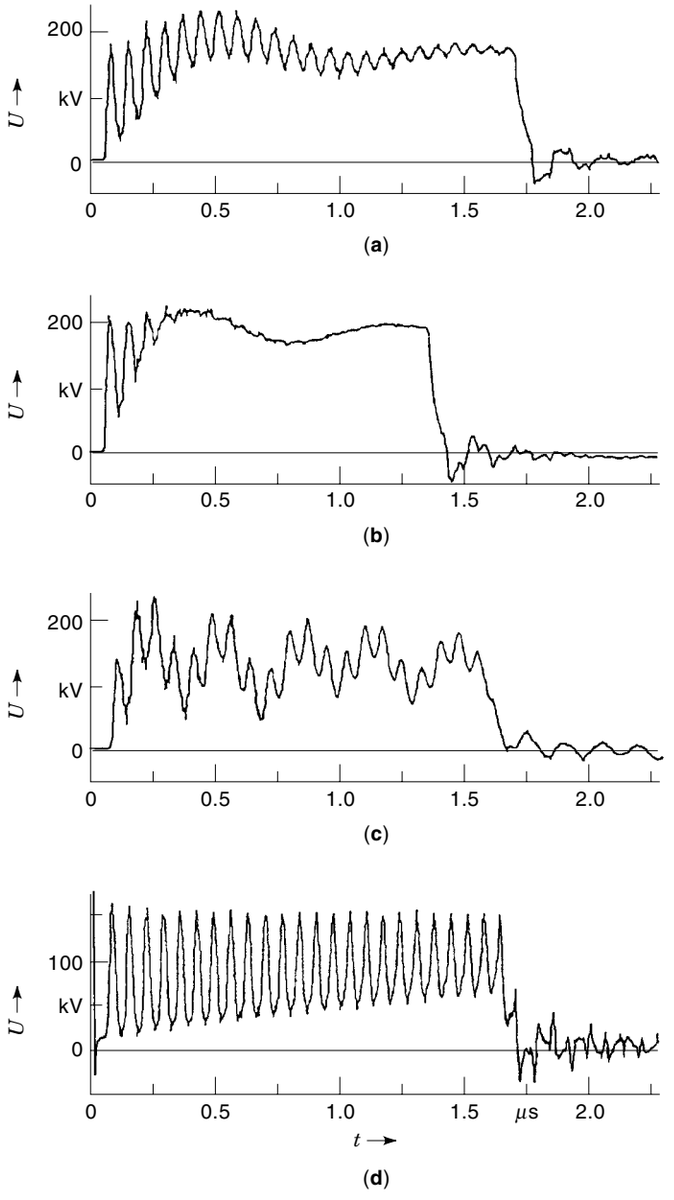

Figure 63. Composite voltage stress in GIS with different FT and VFT components (85).

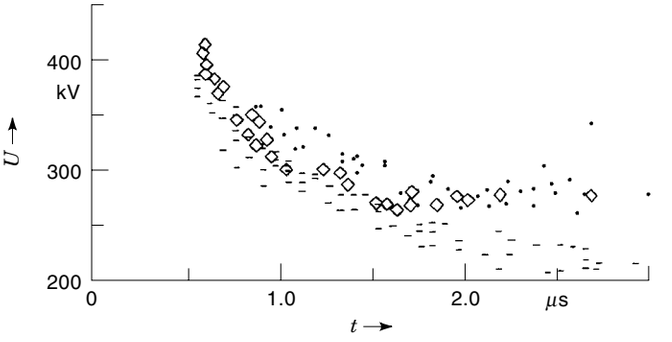

Figure 64. *V–t* curves for transient voltage stress; p = 3 bar, I = 15 mm; ◇—LI stress; ●—composite voltage stress according to Fig. 63(c) and ––VFT stress according to Fig. 63(d) (86).

resulting insulation resistance level (87). Because of the dominant FT oscillation, the voltage shape according to Figs. 63(a), (b), and (c) gives similar values compared with LI stresses. However, transients with a small FT oscillation [Figs. 63(a), (b)] are more critical than LI stresses.

In the case of LI, the streamer–leader transition and breakdown can be described by the precursor mechanism (82), whereas for a VFTO with a high-oscillation frequency and small damping the high-frequency mechanism (76) has to be considered. The corresponding simulation models permit computing the discharge development with satisfactory precision, but only for one type of transient in each case.

A similar tool is necessary to estimate the breakdown levels under composite voltage stress. Based on the physical background of both mechanisms, a new universal theory for the streamer-leader transition has been developed, the so-called energy mechanism (87). The corresponding simulation model allows calculating the leader propagation in SF_6 without corona stabilization for all kinds of steep-transient voltage stresses, such as, for example, LI, VFT, and composite voltage. The main steps of the calculation are described in the following.

Discharge development starts with the formation of a streamer after the reduced limiting field $(E/p)_0$ = 87.7 kV/(mm bar) is exceeded. Considering the different field distribution inside and outside the streamer, its time-varying diameter $D_S(t)$ [Fig. 66(a)] can be computed for each time step. Subsequently the capacitance $C(t)$ of this streamer region to the ground plane has to be determined by precise field calculation. The transient voltage $u^*(t) = u(t) - u_S(t)$ and the capacitance $C(t)$ cause the displacement current $i(t)$:

$$i(t) = C(t)\frac{du^*(t)}{dt} + u^*(t)\frac{dC(t)}{dt} \tag{217}$$

The essential physical effects in the streamer can be simulated simply by the network according to Fig. 66(b). Because of the capacitance $C_S(t)$ of the streamer itself, only the part $i_R(t)$ of the displacement current $i(t)$ causes the thermal losses which result in thermal ionization. Considering this network, the ionization current $i_R(t)$ can be calculated by numerically

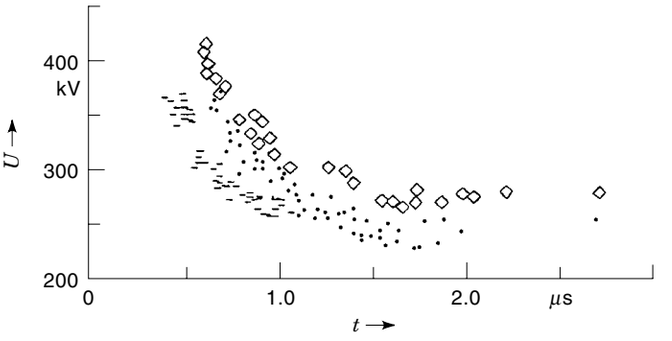

Figure 65. *V–t* curves for transient voltage stress; p = 3 bar, I = 15 mm; ◇—LI stress; ●—composite voltage stress according to Fig. 63(a) and ––according to Fig. 63(b) (86).

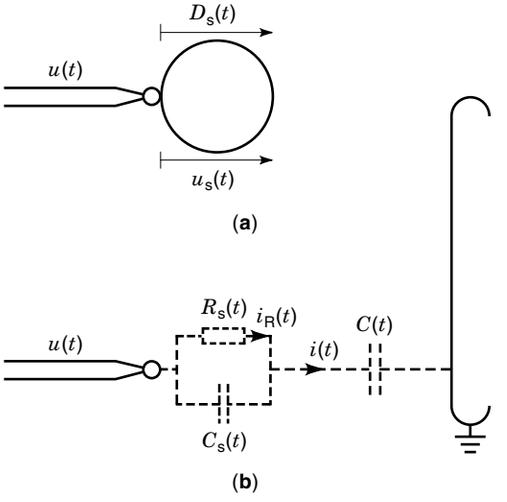

Figure 66. Model of the energy mechanism. (a) Simulation model; (b) equivalent circuit.

solving the following differential equation:

$$i_R(t) + \epsilon_0 \rho \frac{d}{dt}(i_R(t)) = i(t) \tag{218}$$

where ϵ_0 is the permittivity of the free space and ρ the specific resistance of the streamer channel (87). The ionization current $i_R(t)$ and the voltage drop $u_S(t)$ along the streamer length provide a significant energy input into the streamer region:

$$W(t) = \int P(t)\,dt = \int u_S(t) i_R(t)\,dt \tag{219}$$

with $P(t) > 0$ (87). If the enthalpy rise Δh exceeds 6 to 10 $\times$ 10^6 J/kg, the gas is sufficiently dissociated and ionized for leader formation. Consequently the former streamer region is bridged by a leader channel of high conductivity. A new streamer is initiated at the tip of the leader, and the next leader steps can be calculated in the same way as before.

This method of calculation requires the applied LI, VFT, or composite voltage shape, the gas pressure, and the electrode geometry as input data for the field calculation. The results coincide very well with the corresponding measured infrared signals and streak records (87). Leader steps occur only near the maximum of the FT voltage shape, coincident with the positive slopes of the VFT component.

The accuracy of the simulation model was tested by comparing measured and calculated voltage–time curves for different transients, various protrusions, and gas pressures up to 7 bar. The varying field conditions are well represented by the calculations. As an example, Fig. 67 shows the calculated breakdown voltages under LI and VFT stress according to Fig. 63(d) for $p = 5$ bar and $l = 4$ mm (87). There is good agreement between the measured and calculated values. During disconnector operations in real GIS, the composite voltage stress according to Fig. 63(c) has to be considered. Figure 64 shows that in this case the breakdown values for LI and the composite VFT are almost the same.

The following work has been performed for SF_6/N_2 gas mixtures (80) under experimental conditions similar to those described in the initial part of this chapter. As shown in Fig. 68,

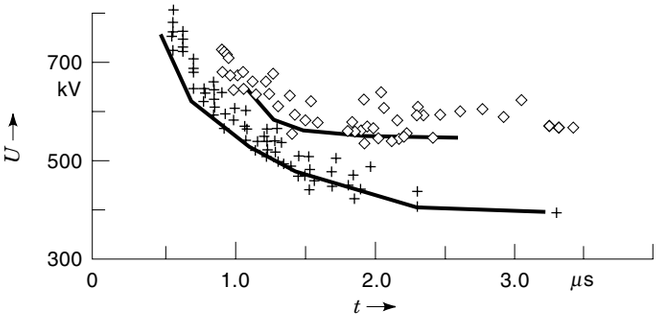

Figure 67. V–t curves for LI and VFT stress; $p = 5$ bar, $I = 4$ mm; ◇—Li, +—VFT according to Fig. 63(d); ––calculated curves (87).

an admixture of only 10% SF_6 to N_2 increases the resistance to approximately 70% of that of pure SF_6. With an admixture of 25% SF_6 to N_2, the resistance can be increased to approximately 85% of that of pure SF_6. However there are also some deviations from this characteristic observed and local minima and maxima of the breakdown voltages occur.

In general the increase of breakdown voltages by corona stabilization (corona peak) increases with the addition of N_2 to SF_6. However at the same time, the corona inception voltages decreased with reduced SF_6 content. It is assumed that the interaction between opposing phenomena cause the local minima and maxima of the breakdown voltage.

As shown in Figs. 68 and 69 the frequency of the VFT-voltage does not strongly influence the resistance of pure N_2. The resistance of pure N_2 for positive polarity is only 66% of that for negative polarity. This behavior agrees with the general breakdown characteristics of nonhomogeneous gaps (see Space-Charge Formation).

For the high-frequency breakdown mechanism it is assumed that for the negative polarity of the VFT-voltage the head of a negative streamer corona, which contains electrons of high mobility, will expand by diffusion much more than a positive streamer head. This results in a smaller concentration of space charges and in a smaller enhancement of the electrical field, which results in a higher dielectric strength.

By an admixture of 10% SF_6 to N_2, some influence on the frequency of the VFT-voltage occurs for negative polarity of

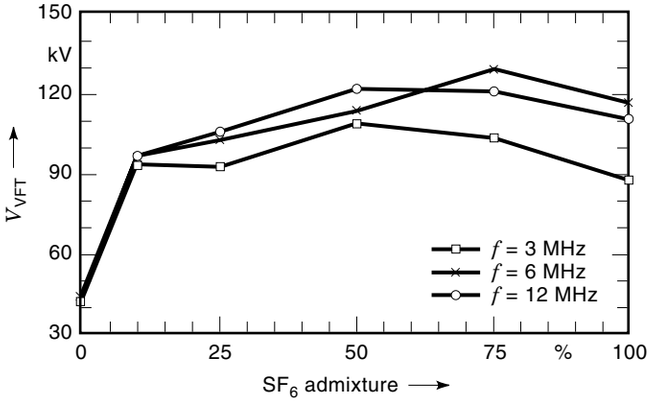

Figure 68. Breakdown voltage V_{VFT} of SF_6/N_2 gas mixtures for VFT-voltage stress of positive polarity and different frequencies of the VFT-voltage; $d = 25$ mm; $\eta = 0.025$; $p = 1$ bar (80).

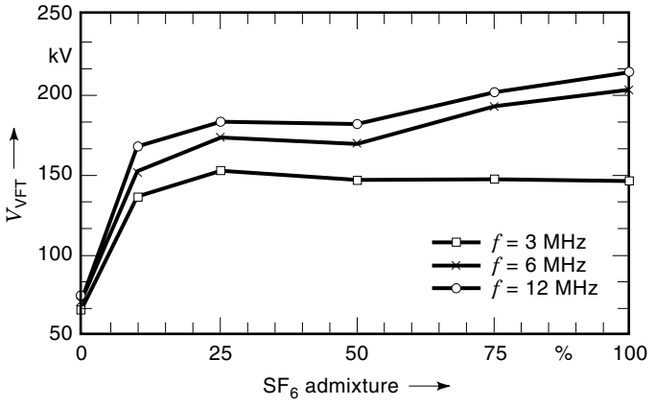

Figure 69. Breakdown voltage V_{VFT} of SF_6/N_2 gas mixtures for VFT-voltage stress of negative polarity and different frequencies of the VFT-voltage; $d = 25$ mm; $\eta = 0.025$; $p = 1$ bar (80).

the VFT-voltage. By increasing the SF_6 content to 25% for the positive polarity of the VFT-voltage a significant influence of the frequency of the VFT-voltage is also observed. In general the lowest frequency of 3 MHz provides the lowest breakdown voltages.

A very important observation is that for positive polarity of the VFT-voltage, pure SF_6 never provides the maximum resistance, but mixtures containing between 50% and 75% SF_6 have the best performance. This behavior is different for negative polarity of the VFT-voltage, but because the resistance generally is significantly higher for that case, it is not decisive for dimensioning.

BIBLIOGRAPHY

1. M. Beyer et al., *Hochspannungstechnik—Theoretische und praktische Grundlagen,* Berlin: Springer, 1986.
2. P. Schulz, *Elektronische Vorgänge in Gasen und Festkörpern,* Karlsruhe: Braun, 1968.
3. A. M. Howatson, *An Introduction to Gas Discharges,* Oxford: Pergamon, 1965.
4. L. I. Sirotinski, *Hochspannungstechnik,* Berlin: Verlag Technik, 1955, vol. 1, part 1.
5. W. Rieder, *Plasma und Lichtbogen,* Braunschweig: Vieweg 1967.
6. Les Renardières Group, Research on long air gap discharges at Les Renardières, *Electra,* No. 23, p. 53, 1972.
7. W. Mosch and W. Hauschild, *Hochspannungsisolierungen mit Schwefelhexafluorid,* Heidelberg: Hüthig, 1979.
8. A. von Engel, *Ionized Gases,* Oxford: Oxford University Press, 1965.
9. L. G. Christophorou et al., *Oak Ridge Natl. Lab. [Rep.] ORNL-TM (U.S.),* **ORNL-TM-6902**: July, 1979; **ORNL-TM-7123**: January, 1980.
10. J. M. Meek and J. D. Craggs, *Electrical Breakdown of Gases,* Chichester: Wiley, 1978.
11. W. O. Schumann, *Elektrische Durchbruchfeldstärke von Gasen,* Berlin: Springer, 1923.
12. H. Raether, *Electron Avalanches and Breakdown in Gases,* London: Butterworth, 1964.
13. B. Lieberoth-Leden, *Über ein Kurzzeitkamerasystem für den Subnanosekundenbereich mit einem getasteten Mikrokanalplatten-Bildverstärker und dessen Anwendung zur Aufzeichnung der Vorentladungsentwicklung in komprimierten Isoliergasen,* Dissertation, Technische Hochschule, Darmstadt, 1987.
14. W. Pfeiffer and B. Lieberoth-Leden, Predischarge development in N_2 and SF_6 at high gas pressure, *IEEE Trans. Electr. Insul.,* **24**: 285, 1989.
15. I. Sander, *Örtlich und zeitlich aufgelöste Spektroskopie an Vorentladungskanälen in Stickstoff,* Dissertation, Universität Hamburg, 1975.
16. T. H. Teich and I. Sangi, Discharge parameters for some electronegative gases and emission of radiation from electron avalanches, *Int. Symp. Hochspannungstech.,* München, 1972, p. 391.
17. T. H. Teich and D. W. Branston, Light emission from electron avalanches in electronegative gases and nitrogen, *2nd Int. Conf. Gas Discharges,* London, 1972, p. 335.
18. M. Giesselmann, W. Pfeiffer, and J. Wolf, Voltage-time characteristics in SF_6 and SF_6-N_2 mixtures, *IEEE Int. Symp. Electr. Insul.,* Washington, DC, 1986, p. 155.
19. W. Legler, Anregung von UV-Strahlung in Stickstoff und Wasserstoff durch einen Elektronenschwarm, *Z. Phys.,* **182**: 169, 1962.
20. K. H. Wagner, Die Entwicklung der Elektronenlawine in den Plasmakanal, untersucht mit Bildverstärker und Wischverschluss, *Z. Phys.,* **189**: 465–505, 1966.
21. A. Pedersen, Criteria for spark breakdown in sulfur hexafluoride. *IEEE Trans. Power Appar. Syst.,* **PAS-89**: 2043, 1970.
22. J. S. Townsend, *Electricity in Gases,* Oxford: Oxford Univ. Press, 1915.
23. T. Aschwanden, Discharge parameter in binary SF_6 mixtures, *IEE Conf. Gas Discharges, IEE Conf. Publ.,* **189**: 1980, 24–27.
24. T. W. Dakin et al., Breakdown of gases in uniform fields. Paschen curves for nitrogen, air and sulfur hexafluoride, *Electra,* no. 32, 61, 1974.
25. A. Wieland, *Durchschlagverhalten von SF_6 und SF_6-Gas-Gemischen bis zu hohen Gasdrücken,* Dissertation, Technische Hochschule, Darmstadt, 1978.
26. B. Hartlieb, *Das Durchschlagverhalten von hochspannungstechnisch wichtigen SF_6-Gas-Gemischen,* Dissertation, Technische Hochschule, Berlin, 1977.
27. T. Aschwanden, *Die Ermittlung physikalischer Entladungsparameter in Isoliergasen und Isoliergasgemischen mit einer verbesserten Swarm-Methode,* Dissertation, ETH, Zürich, 1985.
28. A. Pedersen, The effect of surface roughness on breakdown in SF_6, *IEEE Trans. Power Appar. Syst.,* **PAS-94**: 1749, 1975.
29. C. M. Cooke, Ionisation, electrode surfaces and discharges in SF_6 at extra high voltages, *IEEE Trans. Power Appar. Syst.,* **PAS-94**: 1518, 1975.
30. W. Zaengl and R. Baumgartner, Zur Ursache der Abweichungen vom Paschen-Gesetz in SF_6, *ETZ, Elektrotech. Z., Ausg. A,* **96**: 510, 1975.
31. J. Donon and G. Voisin, Factors influencing the ageing of insulating structures in SF_6, *CIGRE-Rep.,* 15.04, 1980.
32. A. Schwab and R. Zentner, Der Übergang von der impulsförmigen in die impulslose Koronaentladung, *ETZ, Elektrotech. Z., Ausg. A,* **89**: 402, 1968.
33. W. Büsch, *Die Schaltspannungsfestigkeit der Luft im UHV-Bereich bei positiver Polarität und der Einfluß der Luftfeuchtigkeit,* Dissertation, ETH, Zürich, 1982.
34. C. T. Phelps and R. F. Griffiths, Dependence of positive corona streamer propagation on air pressure and water vapour content, *J. Appl. Phys.,* **47**: 2929, 1976.
35. L. Thione, The dielectric strength of large air insulation, in *Surges in High-voltage Networks,* New York: Plenum, 1980, pp. 165–205.
36. R. T. Waters et al., The structure of the impulse corona in a rod-plane gap II. The negative corona: Propagation and streamer-

anode interaction, *Proc. R. Soc. London, Ser. A,* **367**: 321–342, 1979.

37. Les Renardières Group, Research on long air gap discharges at Les Renardières, *Electra,* no. 23, 53, 1972.
38. Les Renardières Group, Research on long air gap discharges at Les Renardières—1973 results, *Electra,* no. 35, 49, 1974.
39. Les Renardières Group, Positive discharges in long air gaps at Les Renardières—1975 results and conclusions, *Electra,* no. 53, 31, 1977.
40. Les Renardières Group, Negative discharges in long air gaps at Les Renardières—1978 results, *Electra,* no. 74, 30, 1981.
41. A. Boillot et al., L'amorcage dans l'air aux grandes distances, *Rev. Gén. Electr.,* **53**: 763, 1974.
42. G. Gallet and G. Leroy, Expression for switching impulse strength suggesting a highest permissible voltage for ac systems, *IEEE Conf. Pap. C,* **73-408-2**: 1973.
43. A. Pigini et al., Switching impulse strength of very large air gaps, *Int. Symp. High Voltage Eng.,* rep. 52-15, Milan, 1979.
44. W. Pfeiffer, Breakdown mechanism and time development of discharges in compressed insulating gases. *Nucl. Instrum. Methods Phys. Res.,* **220**: 63, 1984.
45. P. Völker, *Untersuchungen zur Entwicklung des elektrischen Durchschlags in Gasen und an festen Isolierstoffoberflächen,* Dissertation, Technische Hochschule, Darmstadt, 1981.
46. M. Giesselmann, *Kurzzeitoptische Untersuchungen der Entladungsentwicklung in N_2 und SF_6 an Modellanordnungen bei Gleich- und Impulsspannung,* Dissertation, Technische Hochschule, Darmstadt, 1986.
47. D. Hansen, H. Jungblut, and W. F. Schmidt, Electron detachment from negative ions in sulfur hexafluoride, *J. Appl. Phys. D,* **16**: 1623, 1983.
48. G. Dreger, *Die statistische Streuzeit und die Anfangselektronenrate bei Stoßspannungsbeanspruchung von Schwefelhexafluorid,* Dissertation, Technische Hochschule, TH Darmstadt, 1980.
49. W. Legler, Die Statistik der Elektronenlawinen in elektronegativen Gasen, bei hohen Feldstärken und bei großer Gasverstärkung, *Z. Naturforsch.,* **16A**: 253, 1961.
50. W. Boeck, Die statistische Streuzeit bei Stoßspannungsbeanspruchung von SF_6-isolierten Gasstrecken, *Int. Symp. High Voltage Eng.,* Zürich, 1975, p. 332.
51. W. Boeck, Volumen-Zeit-Gesetz beim Stoßspannungsdurchschlag von SF_6. *ETZ, Elektrotech. Z, Ausg. A,* **96**: 300, 1975.
52. W. Boeck, SF_6-insulation breakdown behaviour under impulse stress, in *Surges in High-voltage Networks,* New York: Plenum, 1980, p. 207.
53. J. Heinhold and K. W. Gaede, *Ingenieur-Statistik.* München: Oldenbourg, 1979.
54. J. Wolf, *Untersuchung der Entwicklung des elektrischen Durchschlages in SF_6 und SF_6-N_2-Gasgemischen für inhomogene Feldverteilung bei Impulsspannung,* Dissertation, Technische Hochschule, Darmstadt, 1988.
55. D. Kind, *Die Aufbaufläche bei Stoßspannungsbeanspruchung von technischen Elektrodenanordnungen in Luft,* Dissertation, Technische Hochschule, München, 1957.
56. L. Thione, The dielectric strength of large air insulation, in *Surges in High-voltage Networks,* New York: Plenum, 1980, pp. 165–205.
57. W. Knorr, *Die Zündung schwach inhomogener Elektrodenanordnungen in SF_6,* Dissertation RWTH, Aachen, 1979.
58. W. Knorr, K. Möller, and Diederich, Voltage-time characteristics of slightly nonuniform arrangements in SF_6 using linearly rising and oscillating lightning impulse voltages, *CIGRE-Rep.,* 15-05, 1980.
59. M. Toepler, Zur Kenntnis der Gesetze der Gleitfunkenbildung, *Ann. Phys. (Leipzig)* [4], **21**: 193, 1906.
60. M. Toepler, Stoßspannung, Überschlag und Durchschlag bei Isolatoren. *ETZ, Elektrotech. Z.,* **45**: 1045, 1924.
61. W. Pfeiffer, *Untersuchung des Verlaufs von Funkenentladungen in verschiedenen Gasen bei Überdruck,* Dissertation Technische Hochschule, Darmstadt, 1970.
62. W. Weizel and R. Rompe, Theorie des elektrischen Funken. *Ann. Phys. (Leipzig)* [6], **1**: 285, 1947.
63. S. I. Braginskij, Zur Theorie der Entwicklung des Funkenkanals, *J. ETF,* **34**: 1548, 1958.
64. M. Junker, *Ein Hybridmodell zur Beschreibung der gesamten Entladungsentwicklung in Funkenstrecken,* Dissertation, Technische Hochschule, Darmstadt, 1995.
65. W. Pfeiffer, Der Spannungszusammenbruch an Funkenstrecken in komprimierten Gasen, *Z. Angew. Phys.,* **32**: 265, 1971.
66. W. Pfeiffer, Gesetzmässigkeiten beim Durchschlag von Funkenstrecken in komprimiertem Schwefelhexafluorid, *ETZ, Elektrotech. Z., Ausg. A,* **95**: 405, 1974.
67. K. Möller, Ein Beitrag zur experimentellen Überprüfung der Funkengesetze von Toepler, Rompe-Weizel und Braginskii, *ETZ, Elektrotech. Z., Ausg. A,* **92**: 37, 1971.
68. W. Taschner, Dependency of *v-t-* curves on the front steepness of testing voltage in SF_6, measuring method and definitions, *IEE 6th Gas Discharge Conf.,* Edinburgh, 1980, p. 172.
69. W. Pfeiffer, Gas breakdown in case of steep fronted pulses and insulator interfaces, *IEEE Trans. Electr. Insul.,* **17**: 505, 1982.
70. B. Gänger, *Der elektrische Durchschlag von Gasen,* Berlin: Springer, 1953.
71. W. Boeck et al., Insulating behaviour of SF_6 with and without solid insulation in case of fast transients, *CIGRE-Rep.,* 15-07, 1986.
72. L. Rohde and G. Wedemeyer, Verluste und Durchschlag bei Hochspannung hoher Frequenz, *ETZ, Elektrotech. Z.,* **61**: 1161, 1940.
73. F. Müller, Der elektrische Durchschlag von Luft bei sehr hohen Frequenzen, *Arch. Elektrotech.,* **28**: 341, 1934.
74. H. Lassen, Frequenzabhängigkeit der Funkenspannung in Luft, *Arch. Elektrotech.,* **25**: 322, 1931.
75. J. Kampschulte, Luftdurchschlag und Überschlag mit Wechselspannung von 50 . . . 100000 Hz., *Arch. Elektrotech.,* **24**: 525, 1930.
76. H. Hiesinger, Leader breakdown for inhomogeneous fields in case of VFT conditions, *7th Int. Symp. High Voltage Eng.,* Dresden, Paper 32.05, 1991.
77. P. Zipfl, *Untersuchungen des Isolationsverhaltens von SF_6 und SF_6-N_2-Gemischen bei Beanspruchung durch hochfrequent oszillierende Stoßspannungen unter Verwendung eines weiterentwickelten Kurzzeitkamerasystems,* Dissertation, Technische Hochschule, Darmstadt, 1992.
78. V. Zimmer, *Isolationseigenschaften von SF_6 und SF_6-N_2-Gemischen sowie von Stützisolatoren bei Beanspruchung mit hochfrequent oszillierender Stoßspannung,* Dissertation, Technische Hochschule, Darmstadt, 1994.
79. W. Pfeiffer, D. Schoen, and C. Zender, Corona stabilisation and prebreakdown development in SF_6 for inhomogeneous fields stressed with very fast transient voltages, *10th Int. Symp. High Voltage Eng.,* paper 3468, Montreal, 1997.
80. W. Pfeiffer, D. Schoen, and C. Zender, Dielectric strength of SF_6/N_2 mixtures for nonuniform field distribution and very fast transient voltage stress. XII, *Int. Conf. Gas Discharges The Appl.,* Greifswald, 1997.

81. O. Farish et al., Corona controlled breakdown in SF_6 and SF_6 mixtures. Invited review, *16th Int. Conf. Phenom. Ioniz. Gases,* Düsseldorf, 1983.
82. L. Niemeyer, Leader breakdown in compressed SF_6: Recent concepts and understanding, *Gaseous Dielectr., 6th,* Knoxville, TN, 1990, p. 49.
83. CIGRE WG 15.03, GIS insulation properties in case of VFT and DC stress, *CIGRE Rep.* 15-201, Paris, 1996.
84. CIGRE WG 33/13-09, Very fast transient phenomena associated with gas insulated substations, *CIGRE Rep.* 33-13, Paris, 1988.
85. W. Boeck and K. Fröhlich, GIS disconnector testing, *7th Int. Symp. High Voltage Eng.,* Dresden, 1991, paper 31.01.
86. D. Buchner, Breakdown behaviour of SF_6 insulation under composite VFT voltage stress, *10th Int. Conf. Gas Discharges The Appl.,* Swansea, 1992, p. 422.
87. D. Buchner, Breakdown of SF_6 insulation in case of inhomogeneous fields under different transient voltage stress, *9th Int. Symp. High Voltage Eng.,* no. 2268, Graz, 1995.

W. BOECK
Technical University of Munich
W. PFEIFFER
Darmstadt University of Technology